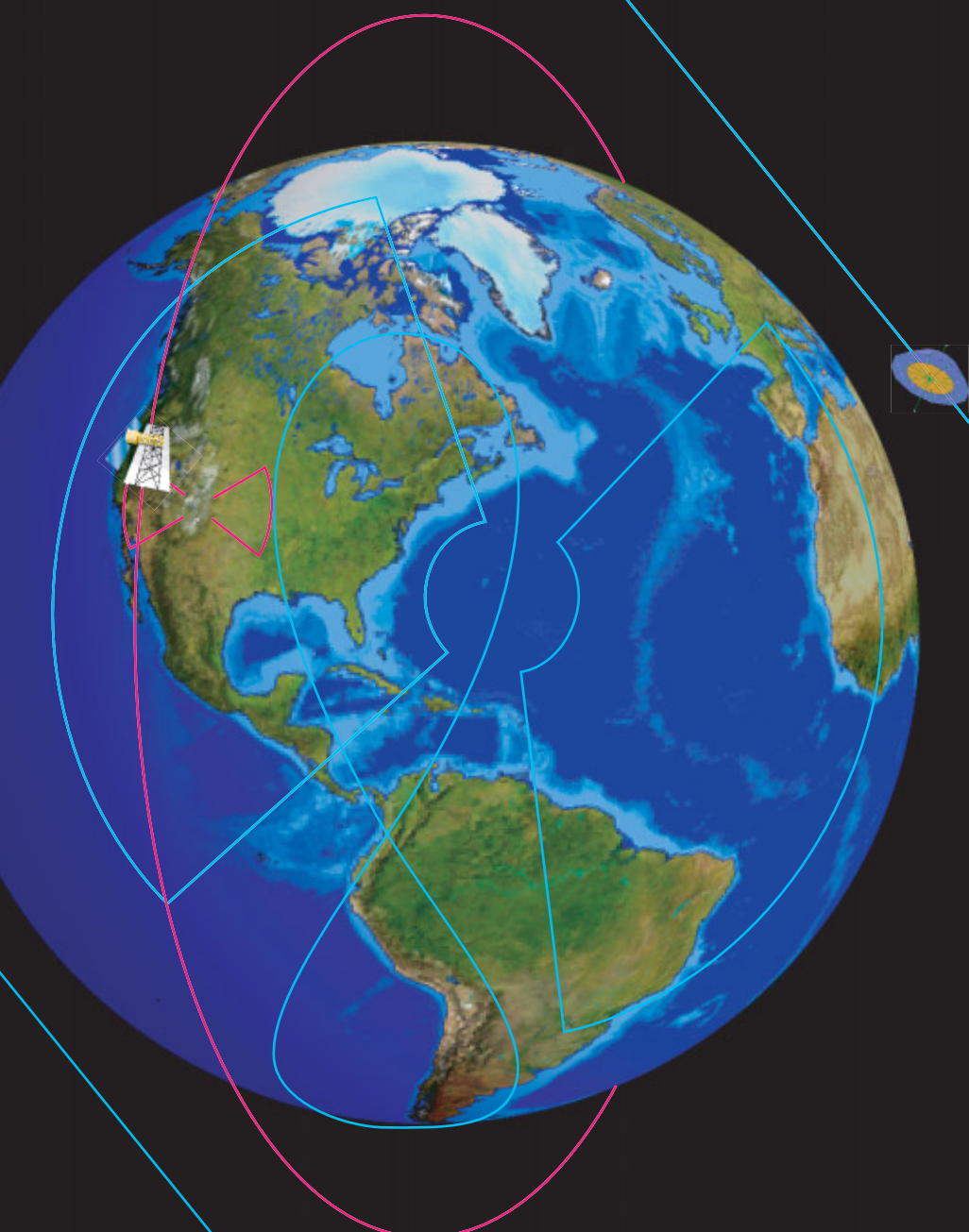


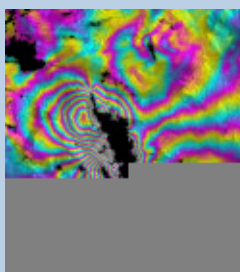
GESS

GLOBAL EARTHQUAKE SATELLITE SYSTEM



A 20-YEAR
PLAN TO
ENABLE
EARTHQUAKE
PREDICTION

MARCH 2003



CONTENTS

Executive Summary	2
CHAPTER ONE Earthquake Hazard Assessment in the Future	4
CHAPTER TWO Scientific Motivation	14
CHAPTER THREE Enhanced Low-Earth Orbit	28
CHAPTER FOUR Geosynchronous Architecture	50
CHAPTER FIVE Optimizing the Measurement	66
CHAPTER FIVE Technology Studies	76
The 20-Year Plan	95
Appendix	98

Executive Summary

THE ELEGANCE OF THE THEORY OF plate tectonics, and the predictability of plate motions, led to an optimistic view during the 1970s that individual earthquakes could be predicted. Decades later, the realization that the dynamics of the solid Earth are complex, nonlinear, and self-organizing has somewhat dampened the early optimism for predicting earthquakes, but has also stimulated a vigorous effort to model and understand their complexity. Today, the importance of a predictive capability can hardly be overstated, as populations in seismically active areas continue to grow, and potential economic losses widen. What will it take to predict earthquakes?

The advent of space geodesy — the science of measuring deformation of the solid Earth — has enabled major advances in understanding the deforming crust. Global Positioning System (GPS) geodesy, and recently the European Remote Sensing (ERS) synthetic aperture radar (SAR) satellites, have given us a glimpse of the revolution in understanding that will come with systematic, highly accurate observations of surface deformation. The near-term prospect of predicting a certain magnitude earthquake on a specific fault, occurring on a particular day or week, is expected to remain out of reach. However, dynamic hazard assessments of individual fault systems at time scales of months appear to be feasible if frequent, high-precision deformation measurements are available.

The NASA Solid Earth Science Working Group (SESWG) produced a report, "Living on a Restless Earth," that offers as its first priority the need for a highly capable system for measuring global surface deformation for understanding earthquakes, as well as myriad other geophysical phenomena. This study translates that recommendation into a detailed implementation plan, focused specifically on improving understanding of earthquakes. To initiate our study of a Global Earthquake Satellite System (GESS) that could provide the data needed to enable prediction, we gathered from the scientific community measurement requirements to address outstanding problems. These requirements were combined with the needs of the disaster response community, and drove the definition of a plan for an end-to-end program that would enable earthquake forecasting.

Although there are diverse geophysical phenomena — electromagnetic and thermal emissions in particular — that appear to bear some relationship to the earthquake cycle, only surface deformation and seismicity can be directly related to it. We focused the observational scenario on obtaining synoptic measurements of surface deformation at appropriate accuracies and temporal scales to reveal the behavior of the crust as it accumulates strain between earthquakes and relieves it through coseismic ruptures, aseismic slip, and other transient

deformation. The optimal system for measuring characteristic surface deformation is an L-band interferometric SAR (InSAR) because the wavelength favors long-term correlation, the measurement capability is all-weather, and the technique allows for automated, wide-area mapping. Our mission and technology studies have, therefore, focused on InSAR missions, and specifically, constellations in different orbit configurations. The required number of satellites decreases with altitude, so a constellation of several satellites in geosynchronous orbit (GEO) performs as well as many more satellites in low-Earth orbit (LEO).

We develop detailed mission architectures for an enhanced LEO constellation, as well as a GEO constellation. To advance towards a reliable predictive capability requires that deformation must be resolved at an absolute accuracy of approximately 1 mm/yr over the course of a decade.

The future modeling environment will maximize the impact of InSAR data by folding current observations into system models. The observational data, including InSAR, GPS, seismicity, and strainmeters, will be assimilated into computational models, which will evolve as they are constrained and verified by the data. The physical processes associated with solid-Earth deformation interact over many spatial and temporal scales. Recent work suggests strong correlations in both space and time, resulting in observable space-time patterns. Data mining will be needed for analyzing the terabytes per day of streaming data in order to search for anomalies and recognize the emerging behavior of interacting fault systems. Near-line and online archives, and rapid access, are critical to enable continuous examination of system behavior, and to provide appropriate and timely data and information to the United States Geological Survey, Federal Emergency

Management Agency, the California Office of Emergency Services, and others.

The disaster management community generally needs information as soon as possible. Their needs drive the data latency requirement, as well as the spatial resolution. Decorrelation is a strong indication of collapsed structures, and the ability to map damaged neighborhoods, for example, within hours of an earthquake would be a great benefit. Data are needed within 24 hours and preferably within two hours for maximum effectiveness.

The challenging observational program described in the report naturally results in a list of investments needed to accelerate development of technology components. At the top of this list are large (30 m diameter), lightweight, low-cost, active, electronically steerable antennas; lightweight, low-power radar electronics; and development of new processing systems for high-vantage-point observations. Models must be developed to estimate the tropospheric water vapor along the radar line-of-sight. And in order to maximize societal benefits, we must invest in creating the ability to merge data sets, rapidly analyze them, and inform interested parties of an impending earthquake.

The measurement requirements generated by the scientific community and the technology roadmaps for different architectures lay the groundwork for building a truly comprehensive global earthquake satellite system. The first step is to focus on surface deformation measurements through progressively advanced L-band InSAR systems and aggressive modeling. These studies, presented here, constitute important steps towards understanding earthquake physics well enough to forecast earthquakes and save lives and assets.

Earthquake Hazard Assessment in the Future

CHAPTER ONE



Understanding the earthquake cycle and assessing earthquake hazards is a topic of both increasing potential for scientific advancement and societal urgency. A large portion of the world's population inhabits seismically active regions, including the megacities of Los Angeles, Tokyo, and Mexico City, and heavily populated regions in Asia. Furthermore, the recent devastating Gujarat earthquake in India and the New Madrid series of earthquakes in the U.S. underscore the vulnerability of areas not thought to be tectonically active. Population growth will exacerbate the potential for huge earthquake-related casualties, and economic losses of tens of billions of dollars will likely occur as a result of future large events. Since earthquake losses, human and material, are primarily the result of structural failures, enforcing appropriate building codes and retrofitting structures can reduce the overall hazard.

Knowledge of the overall earthquake hazard, and more specific regional and local earthquake risk (at the scale of fault systems) is needed to effectively mitigate these earthquake hazards. A global earthquake observing system will monitor the behavior of interacting fault systems, identify unknown (subsurface) faults, guide new models of the deforming crust, and verify those dynamic models. This knowledge will translate into tangible societal benefits by providing the basis for more effective hazard assessments and mitigation efforts.

During the last decades, powerful new tools to observe tectonic deformation have been developed and deployed with encouraging results for improving knowledge of fault system behavior and earthquake hazards. In the future, the coupling of complex numerical models and orders of magnitude increase in observing power promises to lead to accurate, targeted, short-term earthquake forecasting. Dynamic earthquake hazard assessments resolved for a range of spatial scales (large and small fault systems) and time scales (months to decades) will allow a more systematic approach to prioritizing the retrofitting of vulnerable structures, relocating populations at risk, protecting lifelines, preparing for disasters, and educating the public.

The suite of spaceborne observations needed to achieve this vision has been studied, and the derived requirements have defined a set of mission architectures and enabling technologies that will accelerate progress in achieving the goal of improved earthquake hazard assessments.

Three decades ago, earthquake prediction was thought to be an achievable goal. Such optimism has all but vanished in the face of current understanding of the complexity of the physics of earthquake fault systems. The advent of dense geodetic networks in seismically active regions (e.g., SCIGN, the Southern California Integrated Global Positioning System Network), and satellite interferometric synthetic aperture radar (InSAR) from the European Remote Sensing (ERS) satellites, have resulted in great progress in understanding fault ruptures, transient stress fields, and the collective behavior of fault systems, including transfer of stresses to neighboring faults following earthquakes (Freed and Lin, 2001; Pollitz and Sacks, 2002). These improved observations of surface deformation, coupled with advances in compu-

tational models and resources, have stimulated numerical simulations of fault systems that attempt to reveal system behavior. As InSAR and Global Positioning System (GPS) data become more spatially and temporally continuous in the future, the modeling environment will rapidly evolve to achieve revolutionary advances in understanding the emergent behavior of fault systems. This in turn will enable finer temporal resolution (dynamic) earthquake hazard assessments on the scale of individual faults and fault systems. Dynamic earthquake hazard assessment, coupled with rapid postearthquake damage assessments will enable more effective management of seismic disasters.

The Global Earthquake Satellite System (GESS) study began with the requirements generated for the LightSAR mission, as well as those generated in an EarthScope workshop focused on InSAR (J. B. Minster, personal communication, 2001). EarthScope is a National Science Foundation (NSF) initiative, carried out in partnership with the United States Geological Survey (USGS) and NASA, to study crustal deformation in North America. NASA's proposed contribution to the initiative is an InSAR satellite. Under EarthScope, NSF will field an array of approximately 1000 GPS monitoring sites across western North America, one or more strainmeters, and several deep drill holes near the San Andreas fault. The USGS will upgrade and expand its digital seismic network as its contribution. The synergistic combination of these measurements and InSAR-observed surface deformation is expected to yield major advances in understanding of the crustal structure and rheology of the continent.

Whereas the requirements for a near-term InSAR satellite are well understood, the future needs, which are not well defined, are the driver for our study. Therefore, we have exam-

ined the outstanding questions concerning the physics and forecasting of earthquakes, and used these as the basis of a Request for Proposals, issued by JPL, to fund studies that defined measurement requirements for an observing system that could answer them. These questions are:

1. How does the crust deform during the interseismic period between earthquakes and what are its temporal characteristics (if any) before major earthquakes?
2. How do earthquake ruptures evolve both kinematically and dynamically and what controls the earthquake size?
3. What controls the space–time characteristics of complex earthquakes and triggered earthquakes and aftershocks?
4. What are the sources and temporal characteristics of postseismic processes and how does this process relate to triggered seismicity?
5. How can we identify and map earthquake effects postseismically or identify regions with a high susceptibility to amplified ground shaking or liquefaction/ground failure?
6. Are there precursory phenomena (potential field, electromagnetic effects, or thermal field changes) preceding earthquakes that could be resolved from space?

Incorporating this community input, we have formulated a more stringent set of requirements for measurement of surface deformation that will answer questions 1–4, and we consider approaches to addressing questions 5 and 6. The drivers for these requirements are discussed below and in Chapter 2.

Elements of a Global Earthquake Satellite Observing System

Efforts to advance understanding of earthquake physics require detailed observations of

all phases of the earthquake cycle (pre-, co-, and postseismic), across multiple fault systems and tectonic environments, with global distribution. Satellites offer the best way to achieve global coverage and consistent observations of the land surface. While ground seismometer and GPS networks are and will remain critical, the synoptic view of the deforming crust that is possible using satellite data drives the need for a global earthquake satellite observing system. In addition, knowledge of the character of the shallow subsurface is critical to assessing expected ground accelerations.

Surface Deformation Measurements

Measurement of surface change (displacement) constitutes a powerful tool for resolving the deformation fields resulting from tectonic strain (Figure 1.1). Surface deformation includes other components besides tectonic strain, such as surface motion due to ground-water storage and retrieval (Bawden et al., 2001). The InSAR technique relies on correlated image-pairs to derive displacements to the resolution of a fraction of the radar wavelength. If topography is known, two images can be used to derive a map of the displacement in the range direction. Additional image pairs obtained from different look directions (i.e., ascending versus descending) improve the resolution of vertical and horizontal displacements. If topography is not known, three images can be differenced to derive the topography and its change. The accuracy of the measurement depends on several factors, including the radar signal-to-noise ratio (SNR), orbit determination precision, and removal of signal path delays caused by the variations in spurious ionospheric electron density and tropospheric water vapor. All of these errors must be minimized to achieve long-term absolute accuracy of interseismic strain accumulation.



Figure 1.1
Earthquakes can cause significant surface deformation, such as this meter offset from an earthquake in the California desert.
(Robert Eplett,
CA OES)

Subsurface Characteristics

The type of material in the shallow subsurface, and its saturation, affect the ground acceleration experienced as a result of a particular earthquake. Directivity of seismic energy during fault rupture can result in quite different patterns of deformation. Liquefaction, the sudden release of water from saturated, permeable layers, is of particular concern in coastal landfill areas, and on steep slopes. Mapping the degree of saturation in the shallow subsurface will help determine landslide hazards, and may allow the liquefaction hazard to be folded into the overall dynamic earthquake hazard assessment. Radar sounders, along with InSAR displacements, can provide data to augment surface measurements that seek to characterize the subsurface.

Electromagnetic and Thermal Anomaly Precursors

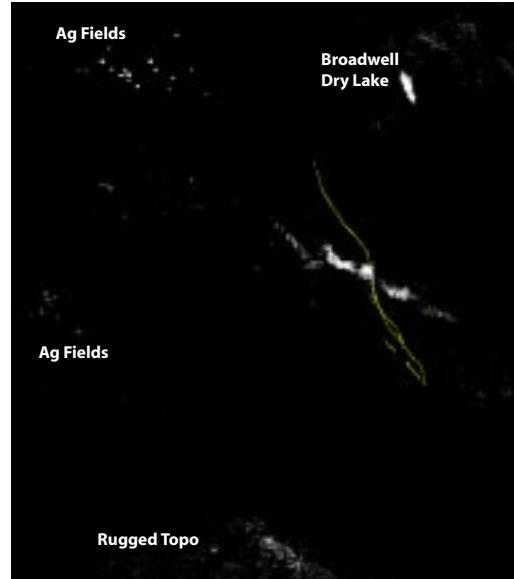
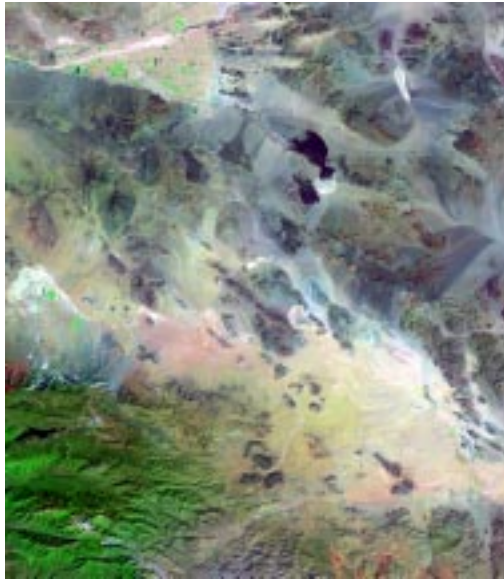
Many claims have been made concerning the correlation of magnetic fields, electric fields, and seismicity, including precursory electromagnetic signals. Mechanisms to produce such correlative variations include move-

ment of fluids in fault zones as a result of stress changes preceding ruptures, and piezomagnetic effects of stress field changes. Improvements in data quality and quantity over the past 40 years have led to a substantial decrease in the correlated signals (Johnston, 1997). Magnetic anomalies associated with main shocks are well documented and can be accounted for by piezomagnetic effects. The subject of precursory electromagnetic signals, and a satisfactory mechanism to explain them, requires more laboratory and field research, as well as high-quality continuous ground and satellite magnetic field data series with proper reference control. Recognizing subtle signals generated at the surface against the background of the highly dynamic external magnetic field at satellite altitudes is challenging. These correlations are likely best tested using carefully configured ground networks in seismogenic zones.

A weak infrared (IR) thermal anomaly was observed near the epicenter of the October 1999 Hector Mine, California, earthquake (Figure 1.2). This and other suggested correlations between thermal IR anomalies and

Figure 1.2

Landsat data for Mojave Desert, California, on October 15, 1999, hours before the Hector Mine earthquake. The visible scene is on the left, and the thermal difference between October 15 and an image from September 29, 1999 is shown at right. A weak thermal anomaly intersects the fault segment that broke in the Hector Mine earthquake (yellow line). (R. Crippen, JPL)



earthquakes have been studied with inconclusive results. As with electromagnetic anomalies, more robust correlations and plausible mechanisms are needed to assess this potential stress indicator. The current Advanced Spaceborne Thermal Emission Radiometer (ASTER) and Landsat ETM+ instruments have good spatial resolution, and may provide data to test existing hypotheses, but coverage is sparse.

Spatial and Temporal Measurement Requirements

The primary focus of the GESS study was the measurement of surface deformation, as this has emerged as the top priority for space-based observation of the earthquake cycle. Light detection and ranging (LIDAR) systems can provide precise measurements of vertical surface change through clear air and even beneath vegetation canopies. Wide-swath LIDAR is thus a promising technique for complementing InSAR (Hofton and Blair, 2002; Chao et al., 2002), especially in vegetated areas.

Detailed requirements for InSAR data gathering have been collected to support three main objectives: long-term measurement of interseismic strain accumulation (to <1 mm/yr resolution), detailed maps of coseismic deformation to define the fault rupture, and measurement of transient deformation such as postseismic relaxation and stress transfer following earthquakes, aseismic creep, and slow earthquakes. To maximize correlation between scenes, especially at interannual time scales, an L-band system is preferred. The mid-term and far-term requirements are summarized in Table 1.1.

Observing interseismic strain accumulation drives the need for very precise long-term accuracy. To distinguish between hazards from blind thrust and shallow faults requires deformation rates to be resolved at the 1 mm/yr level over 10 years. Achieving this accuracy requires mitigating the tropospheric and ionospheric noise in the images, as well as reducing orbit errors. Fortunately, the strain accumulation process is steady, so stacking and filtering techniques can be used to remove

these sources of noise. Short repeat periods enable frequent data acquisitions to support these needs. A promising approach to mitigate the tropospheric water vapor delay is to combine the radar observations with other atmospheric data to derive the water vapor content along the radar line-of-sight. For interseismic strain measurements, the length of the data series may be more important than the revisit frequency and the requirement is on the order of 10 years for an L-band system.

Observation of coseismic deformation drives the need for precise instantaneous accuracy and short revisit times. Exponentially decaying postseismic processes will obscure the coseismic signals with time following the event. Also, good spatial resolution is needed to precisely map the decorrelation and displacement close to the rupture. Transient postseismic strain, as well as aseismic creep and slow earthquakes, drive the need for frequent revisit times to capture these events. Chapter 2 discusses the measurement needs in greater detail.

Concept Mission Architectures

The scientific requirements for studying earthquakes drive two main components of a proposed Global Earthquake Satellite System: accurate, high-resolution surface deformation measurements; and timely, global coverage.

Interferometric synthetic aperture radar techniques provide spatially continuous observations of surface movements in the form of high-resolution displacement maps. InSAR produces unique, spatially continuous, distributed observations. The line-of-sight components of surface displacements can be determined to fractional-wavelength accuracies over hundreds of kilometers at high resolutions (tens of meters). Three-dimensional

vector displacement information can be derived by combining ascending, descending, right-looking, and left-looking data.

A key performance parameter for a disaster and hazard monitoring system is the timely access to and coverage of the target area. InSAR deformation maps can only be generated when the SAR sensor passes overhead and a prior reference data set exists; therefore, the instantaneous field of view (accessible area), and the likelihood that any given target will be covered within a given time are crucial design parameters.

As such, two point designs were selected early in the study to provide innovative radar mission architectures that add perspective to the traditional and tested low-Earth orbit (LEO) missions flown at altitudes from 560–870 km.

Most LEO SAR designs to date, including those of the widely used ERS 1 and 2 satellites, have involved swath widths of around 100 km, and therefore have required orbit repeat periods of around 30–40 days in order to provide global coverage. With the use of ScanSAR techniques (Tomiyasu, 1981), as on RADARSAT and the Shuttle Radar Topography Mission (SRTM), the SAR swath can be extended significantly at the expense of image resolution. This can be a worthy trade, as characterizing coseismic fault rupture requires rapid accessibility — the ability to map a specified target area at a critical time — but only moderate resolution. However, to implement repeat-pass interferometry with a ScanSAR system, the along-track ScanSAR bursts would have to be precisely aligned between orbits. This has not been done before. Increasing the satellite elevation can also enhance the accessibility of a SAR sensor, as doing so generally increases the area the satellite can view at any given time. Generally,

Table 1.1
Requirements for surface deformation measurements.

	MINIMUM	GOAL
Displacement Accuracy	25 mm instantaneous	5 mm instantaneous
3-D Displacement Accuracy	50 mm (1 week)	10 mm (1 day)
Displacement Rate	2 mm/yr (over 10 yr)	<1 mm/yr (over 10 yr)
Temporal Accessibility (Science)	8 days	1 day or less
Temporal Accessibility (Disaster)	1 day	2 hrs
Daily Coverage	$6 \times 10^6 \text{ km}^2$	Global (land)
Map Region	$\pm 60^\circ$ latitude	Global
Spatial Resolution	50–100 m	3–30 m
Geolocation Accuracy	25 m	3 m
Swath	100 km	500 km
Data Latency in Case of Event	1 day	Minutes to hours

it is found that a SAR will only operate satisfactorily if it has a certain minimum antenna area. That area, A , is

$$A \geq k \frac{4v \lambda R}{c \tan \theta}$$

where v is the velocity of the satellite relative to the Earth, λ is the wavelength, R is the range to the target, c is the speed of light, θ is the incidence angle, and k is a weighting factor that depends on the specific sidelobe requirements and is generally on the order of 1.4–2.0. As the range R increases with platform altitude more quickly than the velocity v decreases, the antenna size must increase with orbit elevation. However, the accessible area increases as well. Thus, to the extent that the mission cost is not 100% dominated by the radar aperture size, one will achieve greater efficiency in terms of accessible area per dollar by raising the elevation of the satellite. As past SAR system studies have focused on elevations in the range 560–820 km, and the performance of such systems is fairly well

understood, we have studied the placement of a SAR satellite in a higher, “enhanced LEO” configuration (LEO+) at an altitude of 1325 km.

This design is largely evolutionary relative to present and past LEO SAR systems. The orbit is a proven TOPEX-class orbit, and the radar hardware could be built from existing technology. However, the higher altitude affords a much larger accessible area than traditional LEO systems.

By increasing the satellite elevation even higher for the purpose of improving its accessibility, one can imagine operating a SAR in a geosynchronous orbit (Figure 1.3). Such a system provides an enormous instantaneous field of view, and is also able to provide data at very high resolution, in contrast to optical sensors at those altitudes. However, the technological challenges are significant not only because of the very large active antenna aperture required, but also due to issues relating to processing the extremely long apertures, in particular in

higher resolution modes (2–10 m horizontal). As a SAR uses the relative motion between itself and the target to achieve high resolution, synthetic aperture formation will be impossible from a geostationary geometry, where the radar location is fixed in Earth body fixed coordinates (EBFC). However, when the inclination of the orbit is not zero, the satellite will be moving in EBFC. We have primarily studied circular orbits with inclinations between 50° and 65°. In these cases, the ground track will resemble that shown in Figure 1.3 (a figure eight). In terms of the Earth surface area that is in view from a single satellite at a given time, a geosynchronous satellite will outperform a LEO-type satellite by two orders of magnitude, thus requiring far fewer satellites to cover the globe entirely at all times. The trade-study comparing LEO-type systems to geosynchronous SAR systems is, however, complicated for several reasons. A geosynchronous SAR would require an extremely large antenna aperture, which would involve the use of technologies that are not yet mature. A geosynchronous SAR would also differ from a LEO SAR in its coverage characteristics. Contrary to LEO satellites, a geosynchronous satellite can be placed to provide focused regional coverage for a limited set of Earth longitudes. A minimum of three geosynchronous satellites will be required for global coverage.

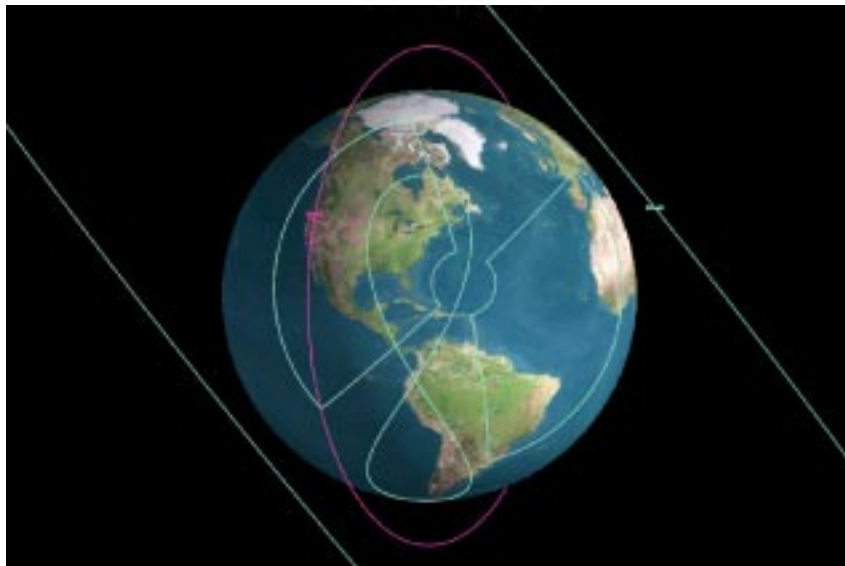
The radar processing required for a geosynchronous SAR would also differ quite dramatically from that of a LEO system because of the peculiar characteristics of geosynchronous orbits, as well as atmospheric changes over the long integration times that arise from the long apertures and low relative velocities. It will also be necessary to address dynamic atmospheric (**troposphere** and ionosphere)

correction, which is presently not well understood and not tested at all.

In addition, we study constellations based on those two point designs. The constellations provide insight as to what future systems could provide in terms of an operational mapping capability. Constellations of satellites capable of providing observations on a very frequent basis (many observations each day) were studied for the LEO+, MEO (medium Earth orbit), and geosynchronous cases. In these evaluations, the relevant performance measure was the likelihood that a given position on the ground would be mapped within a given time. The constellations were also assessed for accuracy in providing 3-D displacement measurements.

A key concern in repeat-pass interferometry is so-called temporal decorrelation. While InSAR measurements reflect the collective displacement of all scatterers within a given image resolution cell — typically tens of meters wide to fractional-wavelength accuracy — the technique breaks down when the scattering centers within the resolution cell experience different displacements, or when the dominant scatterers change from one observation to the next. For example, the vegetation in the resolution cell might induce temporal decorrelation. At longer wavelengths, the radar returns would come mainly from plant branches and trunks, so the signal might decorrelate over periods of weeks to months. At short wavelengths, the radar echoes might come primarily from the leaves, which can decorrelate in seconds as the leaves move with the wind. Precipitation and the freezing or thawing of the ground will also introduce significant temporal decorrelation. Longer wavelengths tend to exhibit better correlation properties over extended time periods. In rela-

Figure 1.3
Orbit and ground trace of a geosynchronous satellite at a 50° orbit inclination (figure eight). Instantaneous field of view for a 5000-km SAR swath is shown (blue). Orbital path and instantaneous field of view for a LEO+ SAR is also shown (pink).



tion to vegetation, longer wavelengths tend to look through the lighter components, such as leaves, to primarily “see” the more stable elements such as branches, trunks, and the ground. The frequency trade-off is counterbalanced by issues such as the ionosphere, and the antenna size. These factors suggest that L-band (approximately 24 cm wavelength) is a good compromise for the frequency selection. The designs presented are based on a single polarization design, to keep cost at a minimum. It is conceivable that a polarimetric capability would allow forming interferograms from polarimetric combinations that would reduce the decorrelation from vegetation.

Also, to bridge the two extreme design points of LEO+ and geosynchronous, we performed a parametric analysis indicating key performance parameters at altitudes in between. Interestingly, the analysis hints that for future around-the-clock monitoring, medium Earth orbit (MEO) configuration, with somewhat smaller antennas and reduced costs relative to geosynchronous, might offer a very capable and effective trade-off.

The scientific requirements outlined in Table 1.1 can be met by various SAR architectures. The report details those architectures in the following chapters. The most promising concepts are a constellation of six to twenty-four SAR satellites in LEO or LEO+ (1325 km) orbits, or three to six geosynchronous SARs. A few LEO+ satellites can optimize most of the requirements, but very short revisit times require larger constellations.

Expected Benefits

Improved Earthquake Hazard Assessments

Current seismic hazard assessments rely on historical earthquake catalogs to predict the statistical probability of future earthquakes. However, there is a spectrum of crustal deformation driven by plate motions that is transient and/or aseismic. Our incomplete knowledge of the deformation budget is a major obstacle to improving predictive capabilities. It is difficult to verify predictive models against infrequent and sparse seismic and geodetic data. There is a debate as to whether the crust is in a constant state of self-orga-

nized criticality in seismic zones, or whether the crust approaches and retreats from that state in a cyclic pattern; the answer has profound implications for the predictability of earthquakes. One promising model posits that normalized surface shear strain across faults, obtainable from dense InSAR data, appears to be a proxy for the unobservable stress-strain dynamics that govern fault rupture (Rundle et al., 2002). The ability to resolve surface deformation to the centimeter level over the entire globe will result in hundreds of earthquakes each year that can be analyzed to test and improve predictive models (Melbourne et al., 2002). Community models will produce dynamic earthquake hazard assessments by using observations in real time, mining the data, and adjusting the earthquake hazard assessments based on the emerging model system behavior. This will allow more effective use of portable ground networks or arrays of instruments (laser strainmeters, seismometers, magnetometers) to capture information on transient fault behavior leading up to an event. While predicting the time, location, and size of a particular earthquake will remain elusive, much higher fidelity earthquake forecasts appear within reach.

The total seismic risk includes the likelihood of a particular seismic event, and the response of any particular site to the seismic waves generated. The worst damage occurs in regions of directed seismic energy, and liquefaction (the sudden liquification of permeable sedimentary layers) often amplifies the damage. Very precise surface deformation measurements will help to identify aquifer discharge and recharge, and can provide information on the saturation of vulnerable subsurface sedimentary layers (Tobita et al., 2002). This knowledge can be folded into the

earthquake hazard assessments to produce a localized, dynamic measure of seismic risk.

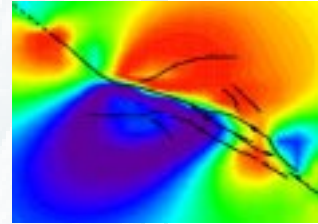
Disaster Management

The dynamic earthquake hazard assessments described will provide the disaster management community with information to focus mitigation efforts. Such efforts include prioritizing retrofitting projects to protect lifelines and infrastructure, educating the public, staging emergency supplies, and establishing mobile communication networks. Earthquake hazard assessment models should be interfaced with decision support systems to guide mitigation efforts.

Temporal revisit times on the order of hours following an event are required to effectively support disaster response efforts. Mapping zones of decorrelation will be most useful to the emergency workers on the ground. Areas that decorrelate between interferograms obtained prior to a seismic event and those that span the event indicate changes in the built environment, and zones of intense shaking that can focus response efforts. InSAR has the advantage of being an all-weather capability for either day or night, an important consideration for obtaining time-critical measurements. Radar-equipped uninhabited aerial vehicles may play an important role in disaster response efforts.

A SAR constellation would allow a staring capability that would reveal the details of transient postseismic behavior and could be particularly useful in the hours and days following a great earthquake to assess the stress transfer and loading of neighboring fault systems, potentially predicting large damaging aftershocks and triggered earthquakes.

Scientific Motivation



C H A P T E R T W O

The requirements for a global earthquake observational system are derived from current scientific understanding of earthquake physics, crustal rheology, and fault interactions, the societal benefits of defining and mitigating seismic hazard, and aiding in disaster response following large earthquakes. In simple terms, earthquakes are generally viewed as being one component of a longer cycle in which a given section of a fault accumulates stress due to plate tectonic driving forces, releases that stress during an earthquake, and then begins the cycle anew. Since these time scales are on the order of seconds for the coseismic portion and centuries for the interseismic phase, we rarely observe a complete cycle. When multiple events do repeat on a given fault segment, significant variation in time scale and earthquake size is the rule. Further complicating our understanding of earthquakes is that they do not occur in isolation. Earthquakes located nearby in space and time induce additional forces into a given fault system, either through the static stress changes induced coseismically, or through temporally evolving postseismic stress changes. Since seismology is essentially confined to the coseismic realm, geodesy is the principal means of measuring the response of the fault and lithosphere during the inter- and postseismic part of the earthquake process. GPS networks have already had a tremendous impact on understanding the earthquake cycle. A space-based system for monitoring crustal deformation is the logical next step to achieve revolutionary advances in earthquake science needed to develop a better predictive capability.

GESS Science Investigations and Requirements

The GESS science requirements derive directly from the GESS investigations that addressed the current and future state of our understanding of earthquake physics, and the measurements necessary (and practical) to advance our understanding (see page 98). Some of the investigations present theoretical or scenario-based models that predict specific space–time behavior of seismicity and patterns of crustal deformation. These studies placed requirements on resolving different classes of lithospheric models and time scales of pre- and postseismic deformation. Other studies presented examples from the current principal satellite SAR system, the European Space Agency's (ESA) ERS satellites, which have formed the basis for much of our current understanding of SAR interferometry, both in terms of performance and in terms of the types of information and applications that are possible. These examples impact both the single image and interferogram data requirements, and also illustrate methods for overcoming some of the error sources through data stacking, time series inversion, or atmospheric modeling. Finally, applications goals such as earthquake disaster response also impact the system requirements.

Before examining the main scientific questions regarding earthquakes, it is worth summarizing how these pieces fit together and their historical context. Our current understanding and the direction we see as necessary to understanding the earthquake process are directly linked to the recent past. Much of our understanding of earthquakes comes from seismology, both in terms of their space–time magnitude, and from understanding the characteristics of the earthquake rupture kinemat-

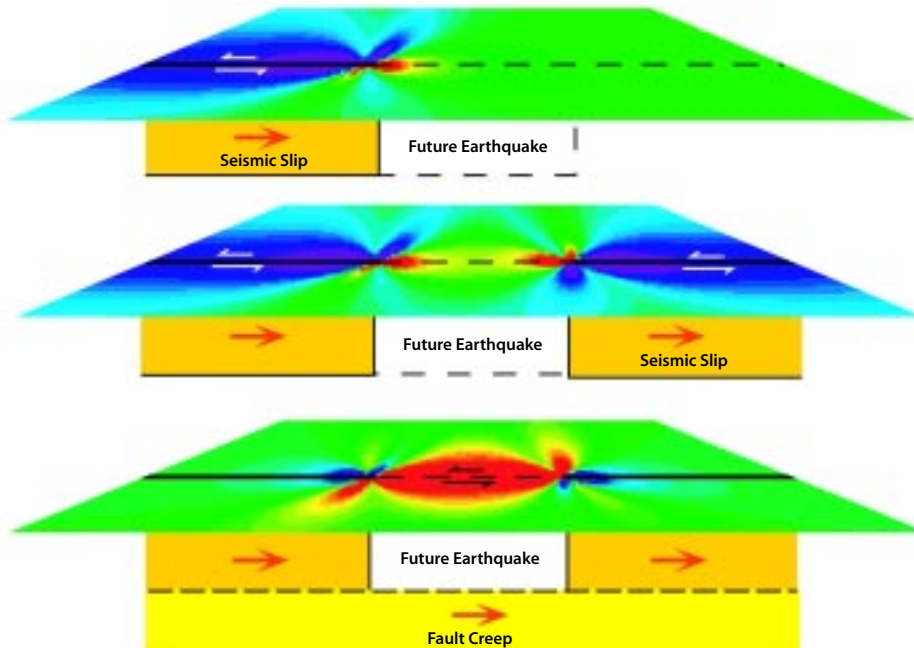
ics and dynamics. Understanding coseismic rupture kinematics has benefited from the use of high-quality geodetic data, in particular the applications of InSAR.

Advances in GPS and InSAR data in conjunction with several significant earthquake sequences (Landers–Hector Mine, California; Izmit–Duzce, Turkey) in the 1990s provided important insight into their coseismic ruptures, and also provided important new observations and model constraints on complex ruptures, triggered earthquake sequences, and aftershocks. The Landers earthquake was the first application of InSAR to crustal deformation. Examination of the complex rupture and aftershocks of the Landers event stimulated development of models based on stress shadowing and stress migration in the crust and upper mantle to explain the space–time occurrence of these triggered events. The case was similar for the Izmit–Duzce and Manyi–Kokoxili, Tibet, earthquake sequences. High-quality space geodetic data (particularly from InSAR) allowed observation of spatial and temporal behavior of the crust following large earthquakes that forced re-examination of the crustal response and the forces governing earthquakes.

The insights gained from these event data sets have in turn boosted a debate regarding the time-varying state of stress in the crust, and have fueled fresh examination of the physics of the earthquake cycle on fault systems. Theoretical models that examine earthquake clustering and stress evolution predict spatial and temporal deformation signals that could be measurable with future satellite systems. This could lead to significant advances in our ability to constrain the locations of future earthquakes.

Figure 2.1

Evolution of Coulomb stresses prior to an earthquake. Each figure shows the progression of the surface Coulomb stress due to earthquakes and deep fault creep on a fault segment that will experience a future earthquake. Warm colors indicate that the change in stress favors a future earthquake. Thus, in addition to the steady-state tectonic loading of the future earthquake segment, the positive Coulomb stress caused by the surrounding fault segments increases the likelihood of an event on the future earthquake segment. (Sammis and Ivins, 2002)



Significant improvement in observation of earthquake crustal deformation provided by GPS and InSAR during the past decade placed critical constraints on some existing models and forced significant revision of others. Perhaps the most significant inference we can draw from these advances is that the feedback loop between data and models is critical, and that future advances will require better data, particularly InSAR data.

As stated in Chapter 1, we solicited studies to define requirements for an observational system that could address specific outstanding questions in earthquake science. The results of the studies are discussed here. In the following section, we have renumbered the original six study questions slightly, combining questions 3 and 4 to emphasize the relationship between complex and triggered earthquakes, and postseismic processes.

- How does the crust deform during the interseismic period between earthquakes and what are its temporal characteristics (if any) before major earthquakes?*

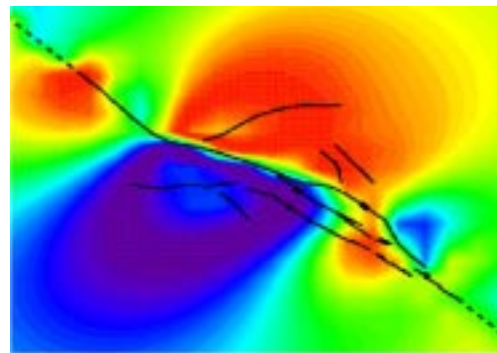
Detecting signals precursory to large earthquakes has been one of the most sought after and debated aspects of earthquake physics. Observations of precursory signals have been sporadic and often without a clear link to the subsequent earthquake. In the cases where the connection is clear, the measurements have generally been point location measurements, sometimes requiring measurement sensitivities that are not possible with satellite systems.

At the core of this debate is whether or not earthquakes are fundamentally predictable. Some have argued that the crust is continuously in a state of self-organized criticality (SOC) with the probability of earthquake size and location remaining steady. Sammis and

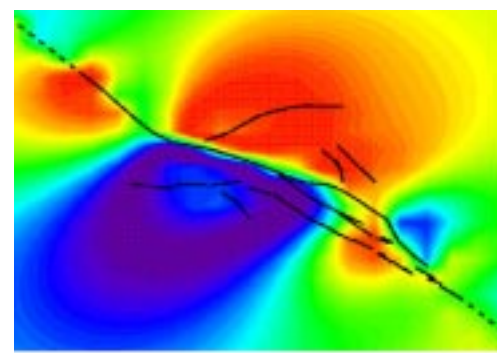
Ivins (2002) and Rundle and Kellogg (2002) argue, instead, that earthquake systems have “memory,” with large earthquakes moving the crust away from SOC through “stress shadowing” (Figure 2.1). This provides testable observations of seismicity and late seismic cycle deformation that could be measured both seismically and with radar interferometry (Figure 2.2). The stress shadow models for the earthquake cycle (Figure 2.1) predict that when the surrounding crust is moved away from SOC less background seismicity is expected, but as a future earthquake approaches an increase in surrounding activity should occur.

The basis for this model is the seismicity and stress shadow models derived for the large earthquake sequences of the 1990s described previously. The exciting aspect of these recent seismic cycle models is that they predict temporally and spatially varying deformation patterns in the termination regions of locked fault segments. These models can constrain earthquake fault system behavior, and should be of a magnitude measurable with radar satellite systems.

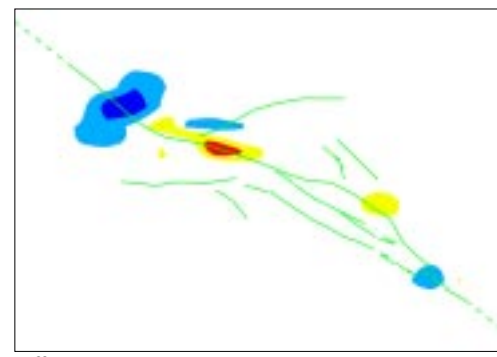
Part of the model for individual faults and fault systems consists of sections that experience either continuous or transient creep. Creep, or aseismic slip, describes slip on fault surfaces that does not produce seismic waves, or discernible shaking. While some creeping fault segments are recognized, and several such segments are monitored locally in well-instrumented regions such as California, many creeping faults are still unknown. InSAR is a valuable measurement technique for detecting and measuring the spatial and temporal characteristics of creeping faults (Figures 2.3 and 2.4), including strike-slip faults (Sandwell and



Five years pre-earthquake.



Five years postearthquake.



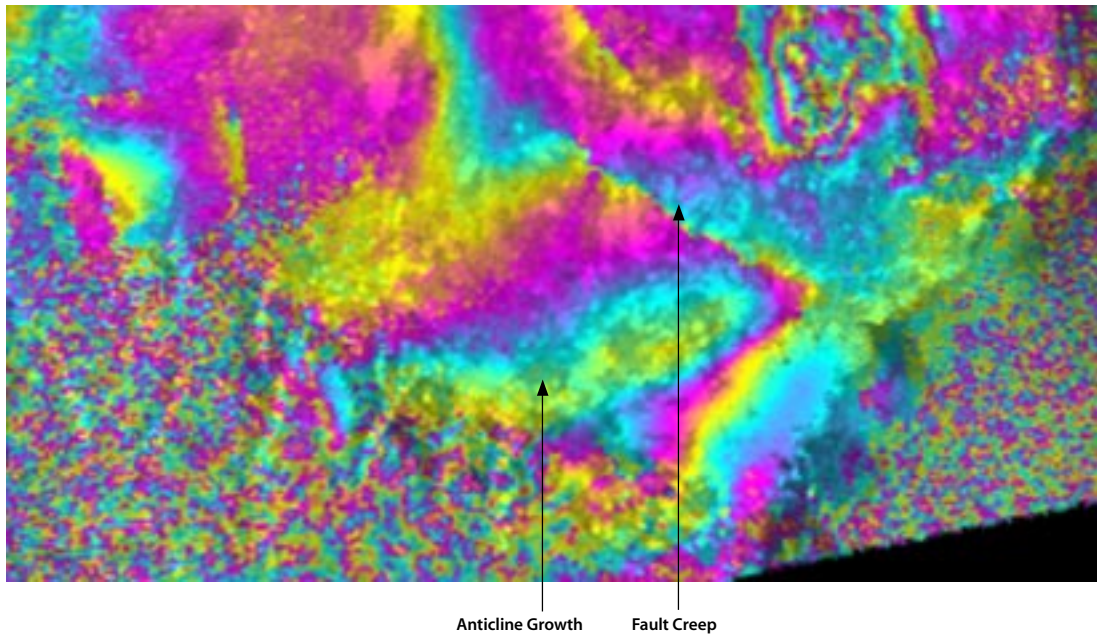
Difference.

Contour Interval = Radar Wavelength

Figure 2.2
Comparison of the predicted deformation due to stress buildup and release for a large simulated San Andreas earthquake, as observed by C-band InSAR. The bottom panel differences the pre- and postseismic signals to show the level of precursory deformation expected, defining the segment of the fault that will rupture. (Rundle and Kellogg, 2002)

Figure 2.3

A portion of an interferogram at Mt. Etna, Italy, showing anticline growth and fault creep (data from 1993–1996, from ERS-1 and ERS-2, courtesy ESA). One color cycle represents 2.8 cm of surface displacement in the radar line-of-sight (LOS). Incidence angle for this image is approximately 23° from vertical toward the west-southwest. The anticline and fault both show approximately 3 cm of LOS displacement. (Lundgren, 2002)



Fialko, 2002; Burgmann et al., 2002; Lundgren, 2002) as well as blind thrusts (Lundgren, 2002). If the motion is steady, stacking (averaging) InSAR data can reduce many of the transient and systematic errors in a series of interferograms (Sandwell and Fialko, 2002). To detect variations in the rate of deformation, least-squares network inversions can be used to calculate an InSAR time series (Figure 2.4), with a relative deformation map at each InSAR data acquisition (Burgmann et al., 2002; Lundgren, 2002). To be able to detect any precursory deformation and to discriminate between even relatively simple models of locked versus creeping areas on faults requires a measurement accuracy of less than 1 mm per year (Zebker and Segall, 2002; Fielding and Wright, 2002).

Requirements

The requirements for detecting these signals requires both wide swath (on the order of 100 km), and detailed spatial sampling (10–100 m). Also required is long-term temporal continuity (over decades) but at fine enough temporal sampling (several days) that precursory phenomena can be separated from the coseismic, postseismic, and aftershock signals that accompany a large earthquake (i.e., Figure 2.2). Similarly, to monitor creep processes on faults, long time span interferograms (more than seven years) are most important for resolving rates at the 1 mm/yr level (Sandwell and Fialko, 2002). However, detecting transient deformation requires weekly or more frequent measurements to improve temporal resolution and reduce atmospheric noise.

2. How do earthquake ruptures evolve both kinematically and dynamically and what controls the earthquake size?

To start to address the question of when and where a future earthquake will occur, and how big it will be, requires an improved understanding of earthquake physics. This starts with more precise knowledge of the coseismic ruptures: how does the slip grow over the fault plane in both time and magnitude, and what controls these parameters? Questions encompassed by this include understanding how earthquakes nucleate and what causes them to stop.

Although answering this question has traditionally been the realm of continuum mechanics and seismology, surface deformation has increasingly played a part in improving kinematic and dynamic coseismic models. InSAR has provided detailed surface deformation maps that place tight constraints on the spatial distribution of slip on the fault plane, thus allowing seismic data to better

define the temporal evolution of the slip when joint seismic and geodetic inversions are calculated (Olsen and Peyrat, 2002; DeLouis et al., 2002).

The location and slip vectors of the coseismic slip for large earthquakes are important in constraining the temporal characteristics of the earthquake rupture, thus defining the driving force for subsequent postseismic crustal response, afterslip, and the locations and sizes of aftershocks. High-density surface displacements as revealed through InSAR have been used over the past decade to place powerful constraints on coseismic slip maps. When combined with other seismic data, the resulting inverse models can image the propagation of the rupture in space and time, and place important constraints on the fault dynamics. Repeat orbit interferometry alone cannot meet the temporal requirements for directly imaging the seismic wave propagation and rupture dynamics near the fault. How-

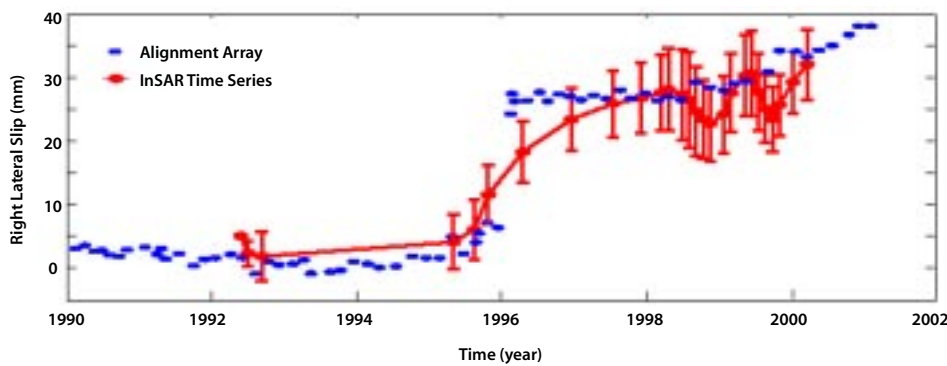


Figure 2.4
Observed surface creep across the southern Hayward fault in Fremont, California. Blue circles show alignment array data which captured a 2 cm creep event in February 1996. Red points display an InSAR time series where the change in range has been projected onto a fault parallel vector. The time series is the result of an inversion using 45 interferograms. Error bars represent the scatter in adjacent pixels. (Lienkaemper et al., 1997)



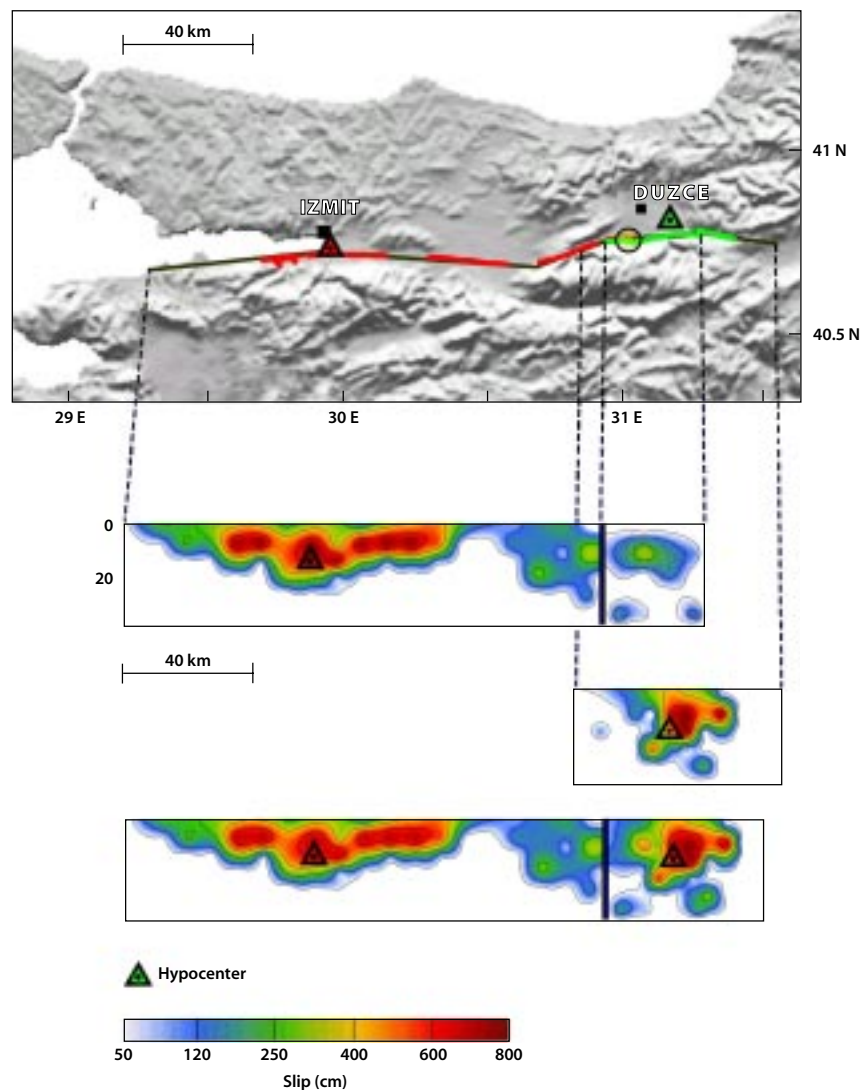
Izmit Earthquake



Duzce Earthquake

Figure 2.5

Complex slip and fault interaction for the 1999 Izmit–Duzce, Turkey, earthquakes (magnitude 7.5 and 7.3, respectively). The two photos are at the same location (indicated with a circle on the panel to the right). The photo on the left is the small fault offset at the eastern end of the Izmit rupture. The right photo shows the much larger normal fault motion that occurred during the Duzce earthquake (photos courtesy of the Seismological Society of America). Middle panel shows each earthquake's surface ruptures (red, Izmit; green, Duzce), hypocenters, and the traces of the modeled fault planes. The lower panels show the individual and combined slip on the fault planes. Notice how the Duzce slip area fills in the area immediately to the east of the Izmit rupture. The model was derived from the joint inversion of InSAR and seismic data. (Delouis et al., 2000)



ever, coseismic interferograms do provide unprecedented images of the surface deformation. This allows creation of detailed models of the slip heterogeneity that help identify rupture asperities, or barriers, and the physical controls on earthquake rupture growth and termination. Slip maps, such as those for the Izmit–Duzce sequence (Figure 2.5) are important input parameters for models of stress loading on nearby fault systems.

Requirements

Coseismic InSAR requires coherent SAR images taken as soon as possible before and after an earthquake in order to minimize the effects due to postseismic and possible precursory deformation transients. Due to the large signal, atmospheric noise is not as corrupting an error source for large earthquakes. For earthquakes such as Izmit, cultivated, vegetated areas were problematic for maintaining correlation between interferograms of C-band ERS data (Fielding and Wright, 2002). This problem would be mitigated by both more frequent repeat data, and with L-band radar (Price et al., 2002). A repeat time of one to three days would be optimal, with a repeat of one week offering significant improvements relative to current systems.

3. What controls the space–time characteristics of complex earthquakes, triggered earthquakes, and their aftershocks, and how are they related to postseismic processes?

Many large earthquakes cluster in space and time. Understanding the process that accounts for an initial earthquake triggering secondary events may reduce hazards, and lead to more accurate forecasts.

The physical parameters that control the spatial and temporal separation of events are poorly understood, such as the seven-year delay of the Landers–Hector Mine earthquakes over the tens of kilometers separating these events (Figure 2.6), or the three months that separated the Izmit–Duzce sequence, whose coseismic ruptures overlapped. In addition to static stress changes caused by a large earthquake, stress rates caused by creeping faults or volcanic processes can also affect seismicity (Toda et al., 2002). Triggered earthquakes pose a significant hazard and are potentially the best candidates to constrain in space and time, since the master event provides the largest change in stress to the local fault systems. At the present, understanding of these events is hampered by incomplete knowledge of the pre-existing physical properties of the neighboring fault systems, and of the evolution of the crustal stresses over time scales of minutes to years that separate coupled earthquakes. The initial conditions cannot be directly measured at present. InSAR could provide detailed measurements of the coseismic and postseismic deformation that would place better constraints on stress diffusion models, and refinements of fault interaction models, that could lead to better-constrained predictions of triggered earthquakes.

Recent observations, principally driven by GPS and InSAR, have revealed complex and relatively fast (days to years) near-field postseismic crustal deformations. These measurements have refined understanding of the different processes (afterslip, poroelastic, viscoelastic) that play a role in the diffusion of stress, both along the fault plane and within the surrounding crust and mantle (Figure 2.6). The detailed, spatially continuous surface deformation measurements

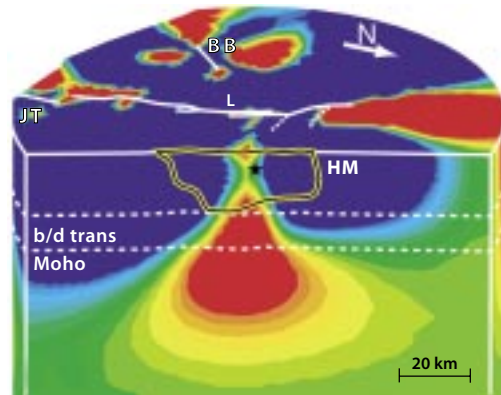
Figure 2.6

Calculated coseismic and postseismic changes in Coulomb stress associated with the 1992 Landers earthquake sequence.

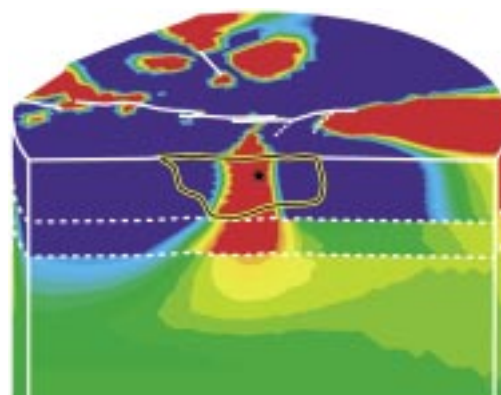
(a) Calculated coseismic Coulomb stress changes shown both for the top ground surface and for a cross-sectional view of the model along the Hector Mine (HM) rupture surface (surface encompassed by black within yellow line). The Hector Mine hypocenter is shown as a black star. The Joshua Tree (JT), Landers (L), and Big Bear (BB) rupture surfaces are shown as white lines on the top ground surface. The lower crust lies between the brittle/ductile transition (b/d trans) at 18 km depth and the Moho at 28 km depth.

(b) Calculated combined coseismic and seven years of postseismic Coulomb stress changes if viscous flow occurs predominantly in the upper mantle. (c) Calculated postseismic Coulomb stress changes due solely to viscous flow during the seven years following Landers (1992–1999).

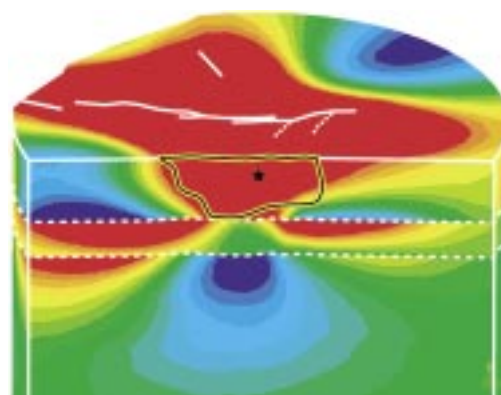
(Freed and Lin, 2001)



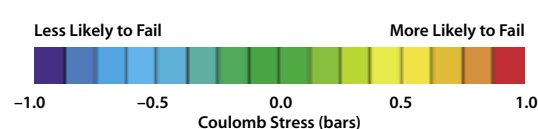
(a) Coseismic (1992)



(b) Coseismic and postseismic (1999)



(c) Postseismic only (1999–1992)



provided by InSAR are an important tool for recognizing these deformation patterns and interpreting the physical processes that cause them.

Requirements

To measure the rapid postseismic deformation and afterslip following a large earthquake (and between the triggered events) requires weekly revisit times. Because time scales of earthquake pairs can be from minutes to years, detecting changes in surface deformation requires similar time scales. Therefore, repeat measurements from one to three days would be better. The more frequent the measurements, the better we can understand earthquake and fault interactions more completely. In addition, frequent sampling allows for larger data sets. This improves signal resolution through stacking and time series computations that reduce the effects of atmospheric and other noise sources. Larger separations in time over greater spatial scales also dictate wide swath coverage over longer time periods, of order one decade. The subtle amplitudes seen for postseismic deformation associated with the Landers earthquake require resolution of deformation rates down to 1 mm/yr.

4. How can we identify and mitigate local seismic hazard (such as liquefaction)?

During an earthquake, the distribution of damage is not uniform and depends on the size and frequency of ground shaking, as well as other factors such as building construction. The reduction in loss of life and property, both during the earthquake and in the time following it, can be mitigated by understanding the areas that are most prone to severe damage,

and in identifying the degree of damage as quickly as possible afterwards.

One important contribution of GESS to earthquake hazard assessment lies in the application of space-based technologies to response efforts by local and federal agencies immediately following a large earthquake. Identifying liquefaction is by definition a post-event analysis. Shinozuka et al. (2002) compared attempts at identifying liquefaction and the ability to differentiate between liquefaction and the effects of ground shaking as the cause of building damage for the 2001 Gujarat, India, and Izmit earthquakes. They found that for the large rural areas of the Gujarat earthquake, the well-documented liquefaction observed in the field was detectable with panchromatic instruments in particular. In the case of the Izmit earthquake, comparison of before and after images for both panchromatic and ERS SAR data demonstrated accurate detection of heavily damaged structures, although the cause of damage, whether ground failure (liquefaction) or severe shaking, could not be differentiated.

Tobita et al. (2002) discussed the use of InSAR data, together with basin models, to estimate the liquefaction susceptibility of earthquake-prone local areas as a function of the saturation of the upper 20 m of the subsurface. Bawden et al. (2001) have shown the ability of geodetic data (InSAR and GPS) to detect surface deformation due to groundwater discharge and recharge in local basins in the Los Angeles region. Integration of tectonic and hydrologic modeling is needed and recommended to resolve tectonic deformation that is occurring against the noise background of hydrologic variations at similar scales and

amplitudes. Further, such an integrated model will contribute to identifying and scaling liquefaction hazards to determine the total seismic hazard. These studies will also provide useful information on the natural periods of soil sites for earthquake site response analysis.

Requirements

For detection of major liquefaction events, and major building damage during disaster response efforts, resolution of 10 m optical and 15 m SAR is acceptable. A smaller pixel size would enable a more complete assessment of ground failure and structural damage. For rapid earthquake response, revisit times of less than one day are best, both in terms of the response time and the quality of the damage maps. For liquefaction susceptibility and earthquake site response studies, subcentimeter resolution of surface change at spatial scales of tens of kilometers with revisit times on the order of a few days would be needed.

5. Are there non-seismic precursory phenomena that may enable and improve earthquake prediction?

There are numerous geophysical phenomena other than surface deformation that have been associated with seismic events. These include: very low-frequency (VLF), ultra low-frequency (ULF), and extremely low-frequency (ELF) magnetic fields observed on the ground and in space, high-frequency electric fields (including earthquake lights), and thermal anomalies observed with satellite sensors. There are individual events, such as the 1989 Loma Prieta earthquake ELF magnetic field, or the warming observed coincident with the Hector Mine earthquake, that appear significantly correlated with seismicity. But controversy remains regarding the statistical

significance of the relationship of these anomalous signals to seismic events, particularly as earthquake precursors. The very small number of occurrences of these phenomena that are properly referenced to background noise, and which have a clear spatial and temporal relation to specific earthquakes, confounds a systematic approach to investigating the possible sources.

An unusual and unique thermal warming was observed by Landsat just 18 hours prior to the Hector Mine earthquake of October 16, 1999 near the Hector Mine fault break (Crippen, 2002). Comparison of the October 15, 1999 scene to the September 29, 1999 preceding scene shows that greatest warming in a zone that intersects the Hector Mine fault break (Figure 1.2). Limited Landsat coverage of the same region does not reveal a similar pattern for the Landers earthquake (1992), but no scene was acquired within 14 days of the Landers quake, and the spatial and radiometric resolutions and repeat coverages were inferior in the earlier Landsat satellites. The Hector Mine warming has also been reported in GOES geosynchronous weather satellite data through a series of images taken every 30 minutes at 5-km resolution. They show an unusual (but subtle) heating trend a few hours before the earthquake.

Earthquake-associated thermal “anomalies” have previously been reported by others, but without the spatial or temporal clarity of “signal” possibly indicated by the Hector Mine observations. Thermal emissions associated with earthquakes have been attributed to changes in fluid flow near fault zones resulting from rupturing of flow barriers as the crust approaches its yield strength (e.g., Hamza, 2001). While pressure-driven fluid flow

within a shallow fault zone could generate a thermal anomaly of the scale and amplitude observed, a high permeability of the affected layers would be required for a precursory signal within one month of a main shock (E. Ivins, personal communication, 2003). This mechanism has been proposed as a means of generating both thermal and electromagnetic anomalies associated with the Loma Prieta earthquake (Fenoglio et al., 1995). To date, no clearly quantified relationship has emerged between thermal emission signals and earthquakes, either preseismically or coseismically. If thermal anomalies precede earthquakes by hours to days, satellite observations will require both high temporal (hourly) and high spatial (< 100 m) resolution to capture the signal.

Precursory quasicontinuous electric and magnetic fields associated with earthquakes, when they can be confidently observed, appear to arise from electrokinetic effects of fluid flow (Fenoglio et al., 1995; Park, 1996). Coseismic signals observed near the epicenter may reflect piezomagnetic effects (Johnston, 1997). Whereas a strong signal was observed by Magsat at 4 Hz for a M 7.2 earthquake in Tonga in 1980, a search for magnetic field signals of recent earthquakes using three currently orbiting high-precision magnetic field satellites did not identify any promising correlations (Taylor and Purucker, 2002). The mechanism proposed for Loma Prieta, invoking the motion of a conductive fluid resulting from rupture of impermeable layers, has also been proposed to explain transient thermal anomalies. Progress in understanding the relationship of electromagnetic and thermal emissions to the earthquake cycle requires

high-quality, frequently updated observations, and verifiable models that satisfy multiple observational constraints.

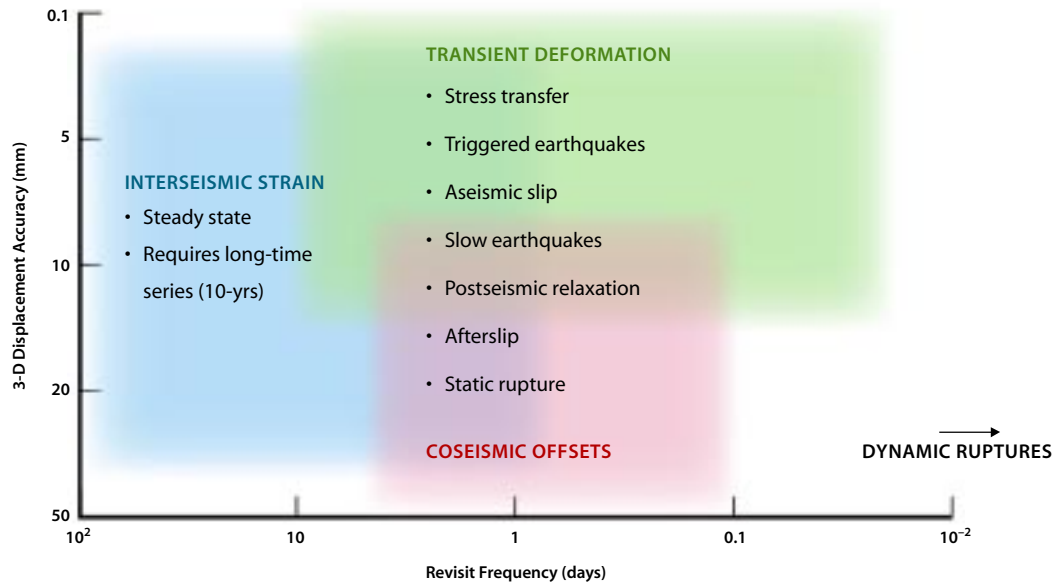
Requirements

High spatial (< 100 m) resolution thermal measurements between 3 and 15 microns, updated hourly to daily, are needed to capture putative ephemeral thermal anomalies associated with earthquakes. Continuous magnetic and electric field measurements at DC to 800 Hz frequency are needed to test whether variations are correlated with seismic activity. Most importantly, these signals must be systematically isolated from natural background noise in a consistent manner, and evaluated simultaneously with crustal stress inferred from surface deformation measurements and fluid motion in the crust inferred from time-varying gravity.

The detailed science requirements discussed above constitute a complete set of observations that contribute to understanding earthquake physics and the earthquake cycle. However, consistent with the recommendations of the SESWG report and the wider community, we have focused our mission architecture on observing surface deformation, as this is deemed the highest payoff measurement to study earthquake physics. We focus on InSAR rather than LIDAR for three reasons. InSAR is an all-weather capability that can efficiently map the globe using a wide swath. It also measures topographic change to fractional wavelength accuracy. Its major limitation is in dense vegetation, and loss of correlation due to major surface disruption or vegetation change unrelated to tectonics. LIDAR can provide very precise “bare-earth”

Figure 2.7

Science measurement requirements for surface displacement.



topography beneath vegetation. Its limitations are inoperability in cloudy air, a narrow footprint, and less-precise surface change detection. The InSAR technique has clear advantages for measuring long-term surface deformation globally. However, the LIDAR technique is likely to be important for local and regional-scale surveys of paleoseismic landforms, and for change detection beneath vegetation canopy.

The derived requirements for monitoring surface deformation are summarized on the science roadmap of Figure 2.7.

Disaster Management

A Global Earthquake Satellite System could contribute to managing earthquake disasters in two ways: by enabling higher spatial and temporal resolution hazard maps, and by

providing timely and valuable information following an earthquake. Hazard assessments are currently used proactively to guide both building codes and disaster preparedness. Spatio-temporal granularity of hazards assessments would allow prioritizing of retrofitting projects according to relative seismic risks. Similarly, emergent behavior of a fault system indicating increasing potential for fault rupture would allow preparations to focus on specific geographic areas and infrastructure assets. In a post-event scenario, GESS would provide maps showing major damage and mapping peak accelerations to accurately assess the magnitude of the damage and guide first-response teams. It would also provide data for real-time mapping of changes in stress on neighboring fault systems to assess potential triggered seismicity.

The needs of the disaster management community drive the latency requirements for downlinking data and producing data products. Data must reach the ground very quickly, and be processed into interferograms within hours of an event to maximize its effectiveness. Direct downlink to users and a distributed processing environment enable this scenario. Data and data products must be released immediately on the Web, and online catalogs of recent data acquisitions, interferograms, and deformation time series must be maintained to expedite processing. Near-line archives of a decimated complete data set are also required to facilitate new analyses. Maps would be produced showing areas where the radar returns have decorrelated to indicate changes in the built environment, as well as maps of peak accelerations showing locations of major damage.

A robust community modeling environment is necessary to support the disaster management community. The community model would provide a sanctioned way to identify emergent behavior of a fault system and adjust hazard maps. Processing of data would be expedited following anomaly detection (precursors), and ground networks deployed to further investigate and monitor fault behavior. Following an event, the model would produce an estimate of the new stress field.

The customers for this information are anticipated to be the USGS, the Federal Emergency Management Agency (FEMA), California Office of Emergency Services (CA OES), local governments, and schools. Enlightening the general public to the dynamic nature of crustal deformation and therefore the hazards they must live with should lead to greater overall preparedness and thus fewer losses.

Enhanced Low-Earth Orbit

CHAPTER THREE

The GESS enhanced low-Earth orbit concept, or LEO+, proposes the operation of one or more L-band SAR systems at an altitude of approximately 1325 km, significantly higher than those of most current SAR platforms. The higher platform altitude affords a wider visible area to the sensor: two 800-km swaths, each comprising seven subswaths, from 300 to 1100 km on either side of the satellite ground track. The large viewable area enables the system to access the entire Earth quickly, reducing the interferometric repeat period to six days and allowing for much finer InSAR temporal resolution than is available from other current or pending SAR missions. The higher altitude also offers better orbit stability, another important consideration for repeat-pass interferometry. A LEO+ mission could be flown using existing conventional technology, though the system would require a slightly larger antenna and greater power than LEO SAR systems.

The radar would be capable of generating high-resolution single-subswath images in a standard stripmap mode and provide lower-resolution, wider-swath images from multiple subswaths in interferometric ScanSAR mode. In stripmap mode, the five-look image resolution would be 30×30 m or better. The interferometric surface-displacement accuracy would depend mainly on the temporal correlation properties of the surface under observation, as well as on atmospheric effects, but with appropriate calibration and post-processing, nominal line-of-sight displacement accuracies better than 1 cm can be achieved. The instrument would acquire right-looking and left-looking data on ascending and descending passes, so it would be possible to synthesize 3-D maps of surface displacement from multiple interferograms with different viewing angles. Over targeted areas, a high-resolution 3-D displacement map comprising ten or more individual images could be generated in under 12 days, and global maps generated annually.

System Parameters

The radar would transmit 10 kW of peak power from a 3.5×13.5 m aperture L-band (24 cm wavelength) antenna that is mechanically steered to a fixed position looking either to the left or the right of the platform direction of motion. Each subswath on a given side would be illuminated through $\pm 10^\circ$ of electronic beam steering. Because the system performance would degrade somewhat with increasing slant range and incidence angle, the inner four subswaths (1–4) on each side are denoted “primary beams” while the outer three subswaths (5–7) are denoted “extended beams.” Across the entire swath, the ground incidence angle varies from 15° to 47° . Instrument parameters and performance measures for each subswath are summarized in Table 3.1.

A split-spectrum approach would be employed for ionospheric correction (see Payload Description for further detail) so that transmitted pulses occupy two distinct subbands of the 80 MHz L-band frequency allocation. The subband pulse bandwidth would be 20 MHz in subswaths 3–7, while the steep incidence angles in subswaths 1 and 2 would require a somewhat larger total bandwidth in order to maintain the required ground-range resolution. (Because the surface would also reflect more radar energy at steep incidence angles, SNR performance would not be sacrificed.) The pulse repetition frequency would be nominally around 1200 Hz.

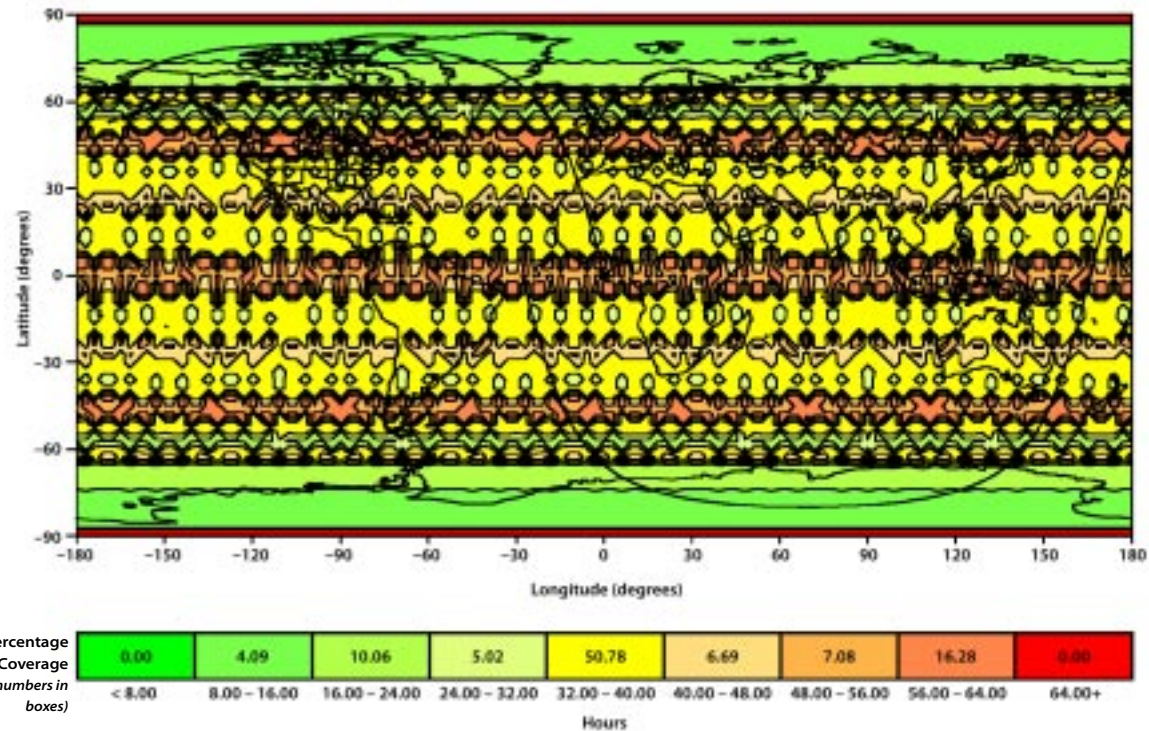


Figure 3.1
The maximum revisit time for any given spot for a single LEO+ SAR at approximately 1325 km altitude and 100° inclination, with a six-day repeating ground track. The percentage of the Earth’s surface that would be revisited within a given time frame is given in the legend below.

Table 3.1
LEO+ beam
summary.

	1	2	3	4	5	6	7
Ground Range from Nadir (km,near/far)	300/450	445/595	590/740	735/835	830/930	925/1025	1020/1090
Look Angle (deg, near/far)	12.7/18.5	18.4/23.7	23.5/28.4	28.2/31.1	31.0/33.6	33.5/36.0	35.8/37.4
Incidence Angle (deg, near/far)	15.4/22.6	22.3/29.1	28.8/35.0	34.8/38.6	38.4/42.0	41.8/45.2	45.0/47.2
Transmit Power (peak, kW)	10.0	10.0	10.0	10.0	10.0	10.0	10.0
Pulse Duration (μs)	50.0	50.0	50.0	50.0	50.0	50.0	50.0
Bandwidth (MHz)	17.0	12.0	10.0	10.0	10.0	10.0	10.0
Polarization	HH						
Pulse Repetition Frequency (Hz)	1240	1191	1233	1178	1224	1176	1220
Ground Range Resolution (m, near/far)	28.8/19.9	28.5/22.3	26.9/22.6	22.7/20.8	20.9/19.4	19.5/18.3	18.4/17.7
Single-Look Azimuth Resolution (m)	6.0	6.3	6.0	6.3	6.1	6.3	6.1
Minimum SNR Assuming Model Soil Surface (dB)	10.4	9.8	9.6	11.1	11.0	10.3	10.3
Maximum Range Ambiguity Level (dB)	-35.0	-36.0	-29.5	-32.8	-26.8	-23.7	-20.1
Maximum Azimuth Ambiguity Level (dB)	-22.1	-20.9	-21.8	-20.4	-21.7	-20.5	-21.5
Data Rate (Mb/s)	142.7	124.6	128.6	95.2	105.9	107.8	84.9

Orbit, Coverage, and Constellations

The satellite would be launched into a nearly circular, sun-synchronous terminator orbit at an altitude of 1325 km and an inclination of 101°; this orbit has a six-day repeating ground track (Figure 3.1). The satellite would be controlled under tight attitude and trajectory constraints in order to facilitate repeat-

pass interferometric processing. Given the satellite orbit and the capabilities of the radar instrument, 85% of the Earth's surface would be viewable by the satellite within 24 hours, and 100% of the surface would be viewable within 60 hours. This quick-response capability of the SAR could provide timely data in the crucial hours and days following an earthquake or other natural disaster.

A constellation of identical satellites in phased, node-spaced orbits could provide even shorter interferometric repeat times and event-response times (see Figure 3.2).

With a constellation of four satellites, the interferometric repeat period could be reduced to 36 hours, and an image of any point on the Earth could be formed by at least one satellite within about 12 hours of an event (or six hours for 85% accessibility). Multiple satellites could also be placed at different orbital inclinations in order to enhance the achievable 3-D surface displacement accuracy. That is, while near-polar orbits are required to provide Earth coverage at high latitudes, they do not offer much diversity in viewing angle at very low and very high latitudes. Hence, in equatorial regions of the Earth for example, the north-south component of surface displacement could not be very accurately determined. Therefore, in addition to the satellite(s) inclined 101°, one or more satellites could be placed in lower-inclination orbits in order to

increase the orthogonality of the directions from which different areas are mapped (Figure 3.3).

A more ambitious constellation of 36 satellites could reduce the interferometric repeat time to four hours and could allow most points on the Earth to be imaged within around two hours or less.

Instrument and Operational Modes

Each satellite could be operated in both high-resolution, single-subswath stripmap modes and wide-area, multiple-subswath interferometric ScanSAR modes (100-m resolution at eight looks). Note that in the interferometric ScanSAR modes, the instrument would need to be timed such that corresponding ScanSAR bursts are aligned between successive orbit passes. This mode of operation has not been demonstrated, but we expect that it is feasible.

If the instrument collects data for one-third of the time it is over land, its operational duty cycle would be approximately 10% on average,

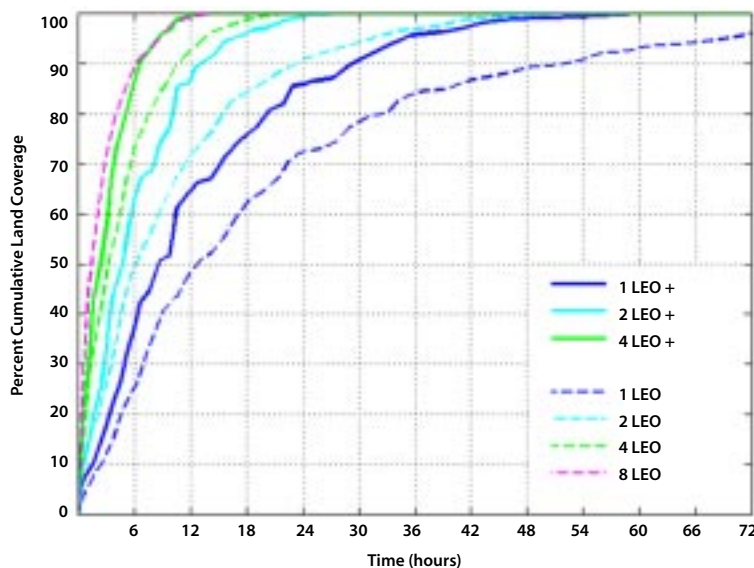
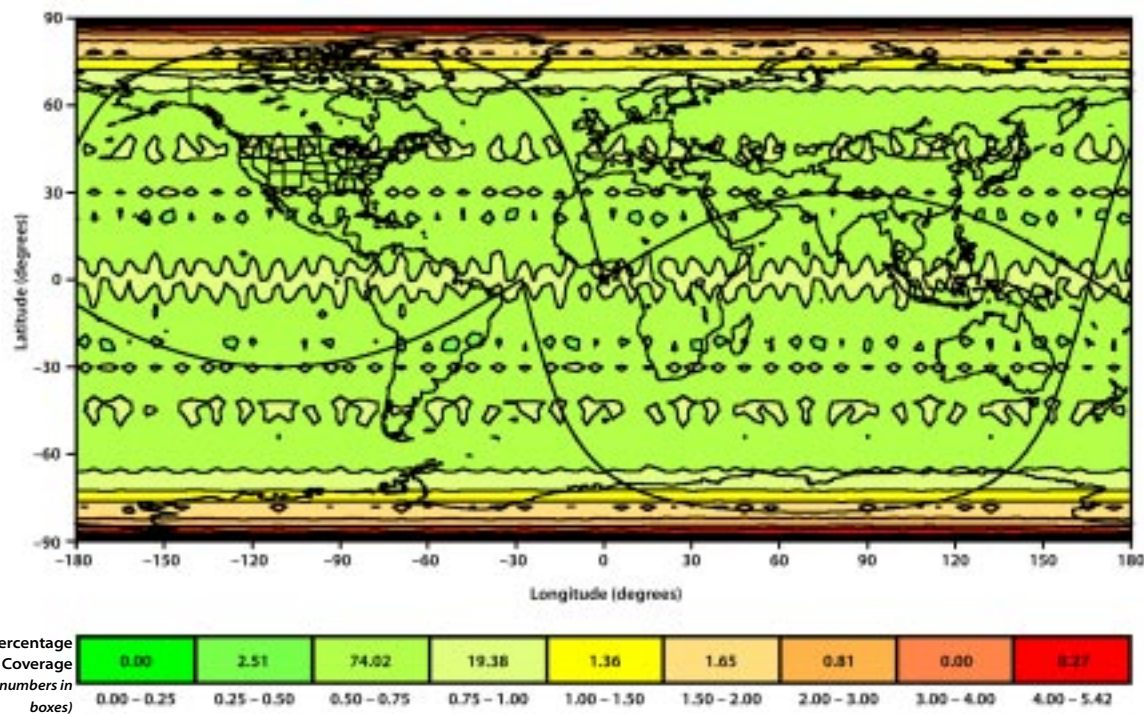


Figure 3.2
A comparison of cumulative land coverage by different LEO and LEO+ constellations. A four-satellite LEO+ constellation covers 90% of the Earth in six hours.

Figure 3.3
Maximum 3-D accuracy from two LEO+ satellites at 101° and 30° inclinations, assuming 1 cm line-of-sight displacement.



though the duty cycle might be significantly higher for some orbits. Each year, the instrument's operational plan would most likely include the collections of different global data sets in various high- and low-resolution modes for archive in an interferometric library (see Table 3.2).

The satellite would also be tasked to collect data as frequently as possible from important seismogenic areas, such as Southern California and other parts of western North America, in addition to other seismogenic zones in South America, Asia, the Mediterranean, and others.

A typical six-month operational plan might consist of 36 days spent acquiring a global, low-resolution, primary-beam, interferometric ScanSAR data set, and 144 days spent acquiring four to six high-resolution maps of western North America and two to three high-resolution maps of other key areas. As

possible, data would also be acquired over other areas to fill in coverage for global high-resolution maps.

The ground resolution depends on which operational mode is in use. The ground resolution for both primary (1-4) and extended beams (5-7) is 30 m in stripmap mode, and 100 m in ScanSAR. The number of looks available also changes for different modes both across and between subswaths. The primary beams have five looks in stripmap mode, and 14 in ScanSAR mode; while the extended beams have five looks in stripmap mode, but 18 looks for ScanSAR. The ground swath for each beam can be calculated from the ground range values in Table 3.1. For stripmap mode, the ground swath in beams 1-7 in kilometers is: 150, 150, 150, 100, 100, 100, 70. In ScanSAR mode, however, the primary-beam ground swath is 535 m, and the extended-beam ground swath is 260 m. Additional

instrument parameters do not vary for subswath or operational mode:

- RF peak power is 10 kW
- Average orbit duty cycle is 10%
- Peak DC power is 3816 W

An illustration of the operational modes and beams is shown in Figure 3.4.

Performance

While the studied system parameters do not represent a final, fully optimized design, they maintain a signal-to-noise ratio of at least 10 dB over the entire visible area, assuming a model scattering profile for a soil surface and incidence angles determined by a nominal spherical Earth. The preliminary design yields a range ambiguity level below -30 dB in the primary subswaths and -20 dB in the extended subswaths, and an azimuth ambiguity below -20 dB in any subswath. Note also that the overall performance is generally better in the middle of a subswath than at its edges, and that the subswath widths can be increased slightly if reduced performance is acceptable in the extended areas. For the stripmap modes, the nominal along-track (azimuth) resolution would be 6 m, and the nominal cross-track (range) resolution projected

onto the ground would be 30 m or better. Performance parameters are summarized in Table 3.1, referenced previously in the System Parameters section.

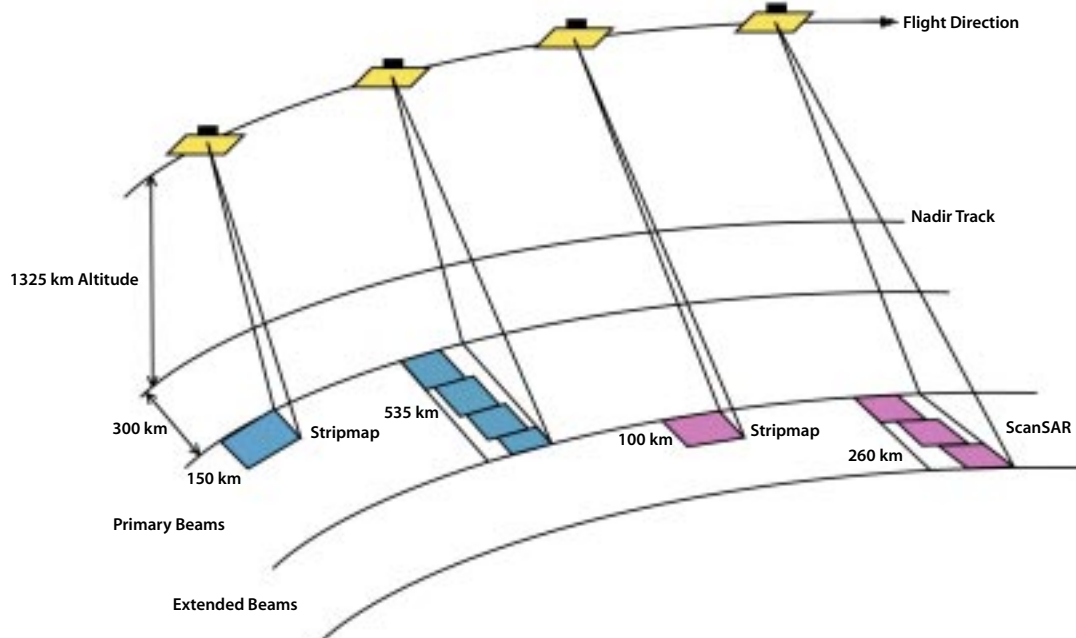
The interferometric displacement accuracy of the system would be highly dependent upon the properties of the surface and the atmosphere at the time data is acquired. Under ideal conditions, line-of-sight displacement accuracies of a few millimeters might be possible from a single interferogram at 30 m resolution, but the performance would degrade considerably in the presence of temporal decorrelation or atmospheric variability. Temporal decorrelation comes about when, rather than bulk displacement, the surface exhibits random change that makes the interferometric phase noisier.

Decorrelation-induced phase noise tends to become more severe as the temporal baseline is increased, but it can also be reduced through averaging, either spatially or over multiple interferometric pairs. Atmospheric artifacts result from the spatial and temporal variations in the effective radar signal path length related to changes in the propagation properties of the troposphere and ionosphere. These artifacts are more difficult to remove,

Global Primary-Beam ScanSAR	(6 days) * (2 sides) / (0.333 over-land duty cycle)	36 days
Global Extended-Beam ScanSAR	(6 days) * (2 sides) / (0.333 over-land duty cycle)	36 days
Priority-Area Primary-Beam Stripmap	(6 days) * (2 sides) * (4 beams)	48 days
Priority-Area Extended-Beam Stripmap	(6 days) * (2 sides) * (3 beams)	36 days
Global Fill-In Primary-Beam Stripmap	(6 days) * (2 sides) * (4 beams) (Targeted Area Time) (0.333 over-land duty cycle)	96 days
Global Fill-In Extended-Beam Stripmap	(6 days) * (2 sides) * (3 beams) (Targeted Area Time) (0.333 over-land duty cycle)	72 days

Table 3.2
LEO+ operational modes.

Figure 3.4
LEO+ operational modes.



but some mitigation strategies are possible (see the Atmospheric Mitigation section in Chapter 5). We expect that average-case accuracies of a few centimeters or better would be possible from a single interferogram, and that these accuracies might be reduced to the subcentimeter level with the proper combination of multiple data sets. (This underscores the need for an InSAR mission that can acquire large amounts of data over short time periods for targeted areas.) We also expect subcentimeter 3-D displacement accuracies for regions between $\pm 30\text{--}70^\circ$ latitude, though as described previously, one of the 3-D displacement components may be indeterminable for other latitudes if data are acquired only from satellites at the same near-polar orbital inclination.

Data Rates and Volumes

The average instantaneous data rate of the satellite would be approximately 105 Mb/s, so assuming a 10% instrument duty cycle, the

data volume collected each day would be about 950 Gb, or 119 GB. Over five years, the satellite would collect more than 200 TB of data that would need to be archived. For downlink and instrument-storage sizing, the maximum instantaneous data rate of 320 Mb/s and a 25% instrument duty cycle would yield 250 Gb of data per orbit. See the Ground Data System section in this chapter for more detail.

Payload Description

The LEO+ mission described here consists of an L-band SAR instrument on a dedicated spacecraft. The radar antenna, consisting of ten lightweight rigid panels and antenna deployment structure, comprises the majority of the radar instrument's 640 kg mass (including 30% contingency). The radar sensor electronics subsystem, which generates the transmit waveform and receives the return echoes, include the RF electronics, data handling electronics, and timing and control electronics.

Radar Sensor Electronics

The Radio Frequency (RF) electronics perform the transmit chirp generation, upconversion, filtering, and amplification during signal transmission (Figure 3.5). They also provide amplification, downconversion, and filtering of the received echo. The instrument uses the full 80 MHz frequency allocation by transmitting and receiving a single linear polarization (HH) chirp in two frequency subbands (split-spectrum) with 70 MHz separation to permit ionospheric corrections similar to the L1/L2 GPS approach. The aggregate bandwidth of both subbands is up to 20 MHz.

Subharmonic sampling will be used to combine the two subbands into a minimum-rate data stream using the least amount of hardware. An NCO-based direct digital synthesizer (DDS) generates multiple chirp waveforms in a small and power-efficient package. Solid-state power amplifiers (SSPAs) are used as the radar transmitter. SSPA technology is very mature at L-band, and several hundred watts to several kilowatts of RF power (over relatively narrow bandwidths) can be readily achieved. For an active phased-array architecture, the transmit power is generated using transmit/receive (T/R) modules distributed on the antenna. In this configura-

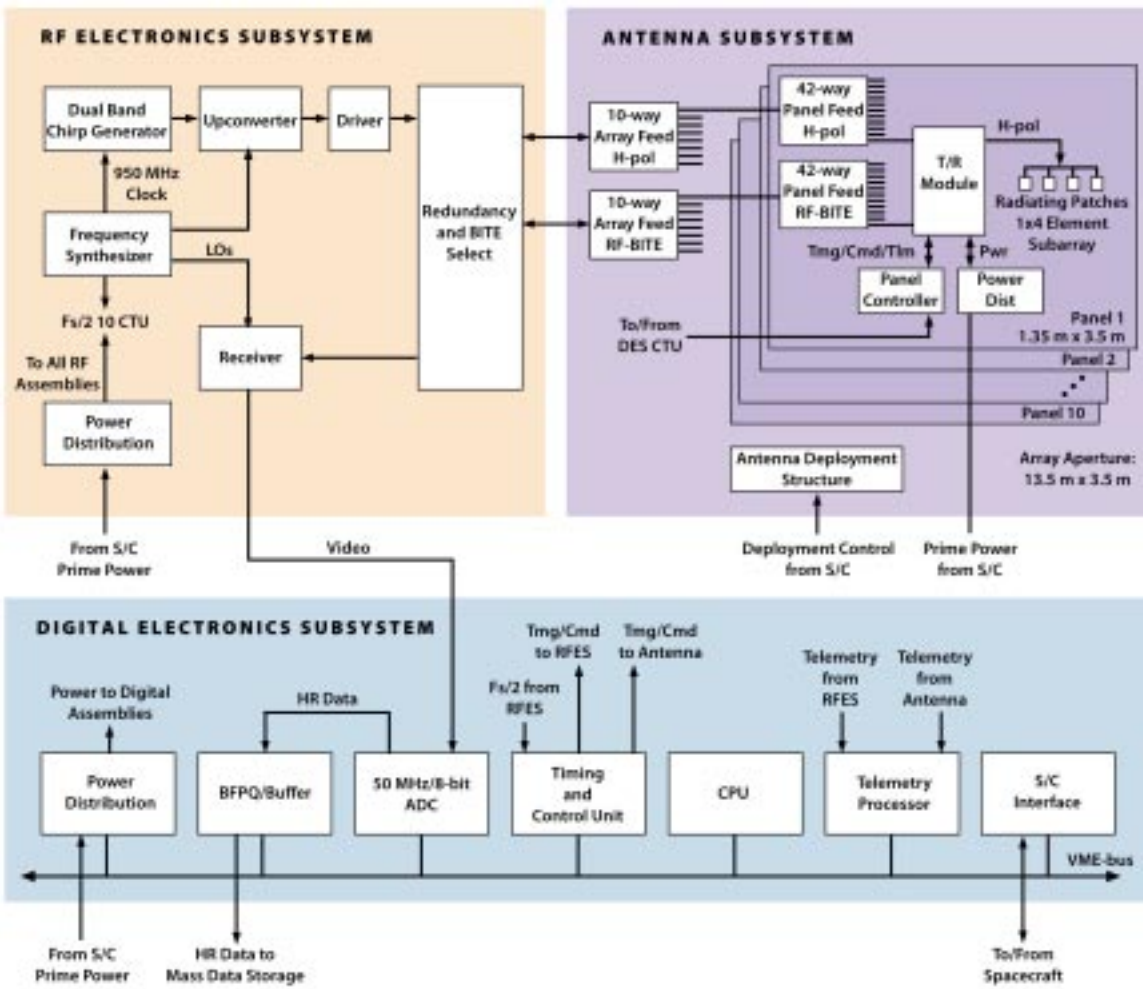


Figure 3.5
Radar electronics
for the LEO+ SAR
payload.

tion, we assume roughly 25 W per module, where 420 modules are distributed along the array to achieve the 10 kW minimum transmit power. The front-end electronics control the signal routing of the primary, redundant, and test/calibration signals. The receiver downconverts the echo received from the antenna and frequency translates the two split-spectrum subbands using a subharmonic sampling technique to produce two concatenated frequency bands at range-offset video. Gain control provides high dynamic range. These signals are then routed to the data handling system for digitization and storage.

The data handling hardware consists of the high-speed analog-to-digital converter (ADC), data buffer and block floating-point quantizer (BFPQ). For the subharmonic sampling receiver, the ADC sample clock is only required to be 50 MHz, with an analog bandwidth of 80 MHz, sampling at 8 bits per sample. The BFPQ converts the 8-bit data to 4-bit data and the buffer reduces the peak data rate to interface with the solid-state recorder (SSR). Formatting includes embedding a sync word, frame count, and spacecraft data (GPS, time) into the data stream. Only one high-rate data channel is required.

The radar control, timing, and telemetry hardware includes a central processor unit (CPU), telemetry processor, spacecraft interface module, radar control and timing unit (CTU), and power module. A dedicated CPU is implemented to control and manage the instrument functions and data flow. This approach ensures a simple interface to the spacecraft and aides in ground testing of the instrument. While the CTU generates deterministic subsecond timing parameters, the CPU controls operations for time scales greater than one second (ScanSAR control

parameters, radar mode, data flow). The dedicated CPU will be able to easily handle the control algorithm to calculate and store in a look-up table the beam position for ScanSAR operation. Based upon the command word generated by the CPU, the CTU generates the timing signals necessary to control the radar, including pulse repetition frequency (PRF), receiver protection and gain control, antenna phase shifter settings, and data window position.

The radar electronics will be housed in two separate chassis, one for the RF electronics and one for the digital electronics. Each subsystem has its own dedicated power distribution unit to convert the raw spacecraft voltages to the required DC voltages and to condition and distribute them to the subsystems. Full block redundancy of the radar electronics is implemented to achieve the five-year mission lifetime. The RF electronics consist of primary and redundant subassemblies and the Redundancy/Built-In-Test select switch matrix, each packaged in a separate shielded enclosure. Surface-mount RFIC/MMIC technology in microstrip circuits ensures cost-effective, low-mass packaging. The digital electronics will reside in a standard VME chassis. Standard VME architecture enables the use of several existing commercial-off-the-shelf (COTS) hardware assemblies to reduce cost and risk. These include the CPU board, the Telemetry Processor Board, the spacecraft I/O interface board, and the power distribution and conditioning board. The custom digital hardware uses FPGA technology to reduce size and power while increasing flexibility of the design.

Radar Antenna

The antenna performs the beam steering and transmission function as well as high-power amplification on transmit and low-noise

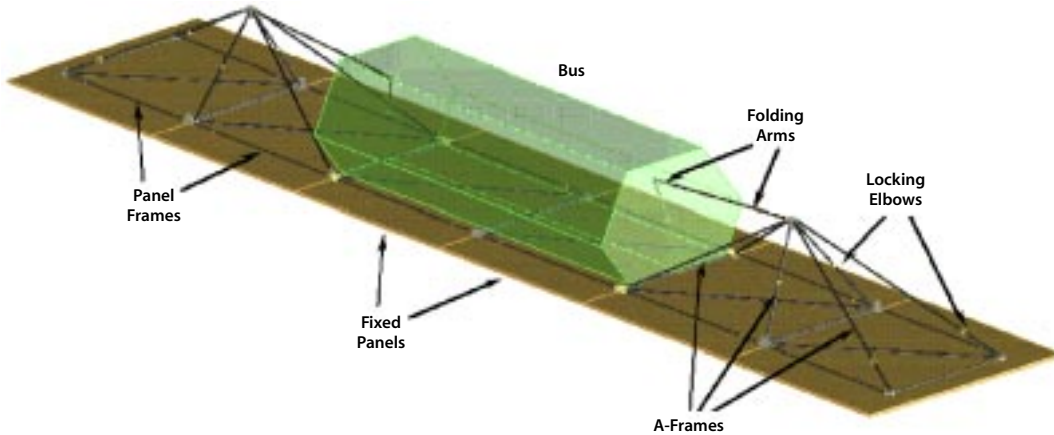


Figure 3.6
LEO+ deployed
antenna using a
RADARSAT-2
modified truss
structure.

amplification on receive. The antenna is a corporate-fed planar phased array with deployable antenna structure (Figure 3.6). The use of many distributed T/R modules on the antenna provides inherent redundancy since random failures of the T/R modules result in a graceful degradation of radar performance. The Antenna Subsystem consists of the RF aperture (antenna panels) and the deployment structure. When stowed, the antenna is folded into ten panels, each measuring $1.35\text{ m} \times 3.5\text{ m}$. The antenna width (3.5 m) was selected such that it could be accommodated in several existing launch vehicles. The radiating elements consist of half-wavelength microstrip patch radiators. To minimize grating lobes, an element spacing of 0.7λ is selected so there are 21 (elevation) $\times 80$ (azimuth) radiating elements in the full array. The radiating elements are single polarization (HH) and combined into 1 (elevation) $\times 4$ (azimuth) element subarrays that are each driven by a single transmit/receive (T/R) module. The T/R modules, with integrated 4-bit phase-shifters, are distributed over each antenna panel to achieve elevation steering as well as to minimize losses. The 420 T/R modules are organized in panels,

which contain 21 (elevation) $\times 2$ (azimuth) T/R modules (42 modules). This configuration enables one phase shifter per elevation element. Although there is no azimuth steering requirement, the antenna does have the capability of limited azimuth scanning. To facilitate ground testing and in-flight performance monitoring, an RF Built-In Test Equipment (BITE) capability is included in the T/R module. A small portion of the transmit signal is coupled to a BITE port and routed to the receiver to monitor the transmitter performance of the antenna. Alternatively, an in-band caltone signal can be routed through the BITE feed and coupled into the T/R module's LNA to test the receive portion of the system. This calibration feature can be implemented as either a special test sequence during a non-data-taking mode or else incorporated directly into the data-taking mode. A broadband corporate feed network distributes the RF signals to and from the antenna elements. The coaxial array feed distributes the RF signals to each panel. Within each panel is a microstrip panel feed to distribute the RF signals to each subarray. Conventional multiwire harness cabling distributes the DC power and control signals to each panel.

Table 3.3
Instrument mass
and power for GESS
LEO+ mission.

	QUANTITY	MASS (KG)	PEAK DC POWER (W)	STANDBY POWER (W)	ORBIT POWER AVG (W)
Antenna Subsystem		433.0	2783.3	13.3	278.3
T/R Modules	420	43.0	2066.7	0.0	
Panels (Aperture, Panel RF Feed, Frame, Hinges)	10	298.0	0.0	0.0	
Antenna Panel Electronics	10	10.0	160.0	10.7	
Antenna DC-DC Converters	67	10.0	556.73	2.7	
Antenna Array RF Feed	—	10.0	0.0	0.0	
Antenna Power and Control Cabling	—	15.0	0.0	0.0	
Deployment Structure	1	47.0	0.0	0.0	
Interface Structure and Launch Support	s/c	0.0	0.0	0.0	
Actuators and Release Mechanisms	s/c	0.0	0.0	0.0	
Thermal Blankets (MLI)	s/c	0.0	0.0	0.0	
Radio Frequency Electronics Subsystem		29.0	91.1	11.1	9.1
Chirp Generator	2	2.0	12.0	0.0	
Frequency Synthesizer	2	3.0	20.0	10.0	
Upconverter	2	2.0	7.0	0.0	
Driver	2	4.0	28.0	0.0	
Receiver	2	2.0	3.0	0.0	
Red and BITE Select	1	1.0	12.0	0.0	
Power Distribution	2	3.0	9.1	1.1	
Housing, Cabling, and Misc.	1	12.0	0.0	0.0	
Digital Electronics Subsystem		31.0	61.3	41.3	6.1
Timing and Control Unit	2	2.0	7.0	7.0	
ADC/Buffer	2	3.0	10.0	0.0	
BFPQ	2	2.0	6.0	0.0	
CPU	2	2.0	10.0	10.0	
Telemetry	2	2.0	10.0	10.0	
S/C I/F and Data Formatter	2	2.0	6.0	6.0	
Power	2	3.0	12.3	8.3	
Housing, Cabling, and Misc.	1	15.0	0.0	0.0	
Radar Total		493.0	2935.7	65.7	293.5
30% Margin		147.9	880.7	19.7	88.1
GESS Radar Total w/ Margin		640.9	3816.4	85.4	381.6

The antenna structure is a deployable truss structure, which provides both support and strength to the panels and maintains flatness of the full array. The structure and deployment mechanisms must be reliable and lightweight and must deploy such that the antenna is flat, structurally stiff, and thermally stable. The flatness requirement of the antenna is one-sixteenth of a wavelength (1.4 cm) to minimize antenna pattern distortion. Two competing truss structures are suitable for this application. A modified deep-truss structure (as used in Seasat and RADARSAT-2) has extensive heritage and is considered relatively low risk. The edge-truss structure offers a very compact stowed envelope although it is less mature technologically. Both are very lightweight and can meet all GESS structural requirements. The spacecraft provides the interface, launch support structure, and thermal blankets. The instrument mass and power are shown in Table 3.3.

Heritage

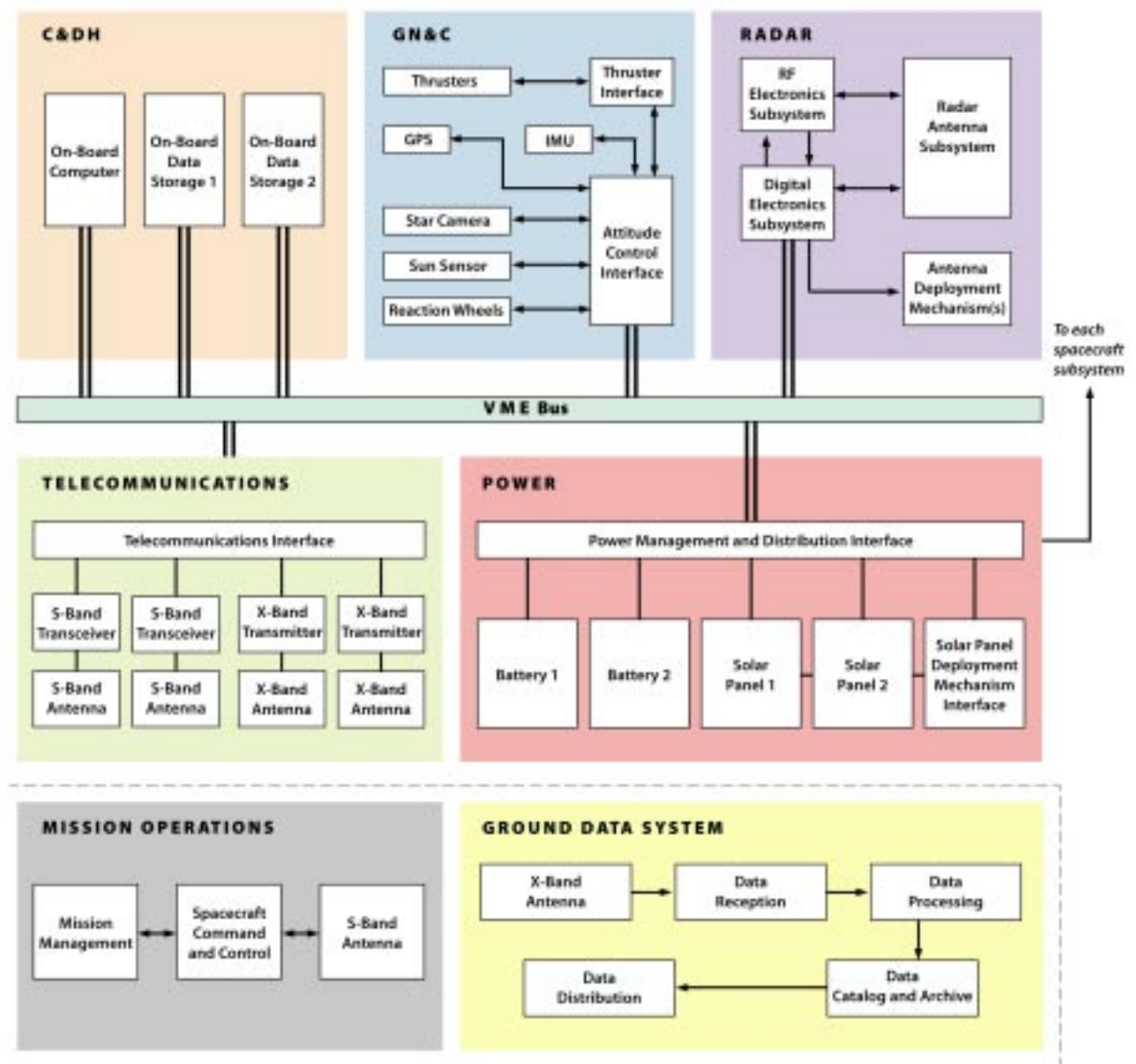
While the instrument is based on existing technology, it represents a major leap forward in measurement capability. The GESS L-band SAR instrument derives much design and hardware heritage from its SIR-C predecessor. SIR-C experimentally validated several new SAR techniques including ScanSAR, spotlight SAR, and repeat-pass interferometry. Technology development activities following the success of SIR-C have focused on reducing the mass, power, and cost of similar instruments to enable a future free-flyer. The Advanced Radar Technology Program (ARTP) in collaboration with LightSAR demonstrated numerous L-band SAR component technologies with significant reductions in mass and power. Many of these technologies can be imple-

mented in the GESS LEO+ mission for cost and risk reduction. For instance, based on LightSAR prototyping activities related to the antenna panel, T/R module, and structure, the total antenna mass density is projected to be roughly 10.2 kg/m^2 , which is a significant improvement over the SIR-C L-band panels (23 kg/m^2) and the SRTM C-band outboard antenna (20 kg/m^2).

Mission Design

The design of the LEO+ mission is summarized below. Overall objectives and subsystem requirements were defined, and traded against, to achieve this baseline design. The LEO+ spacecraft block diagram showing the subsystems is illustrated in Figure 3.7. The five-year mission duration requires the use of functional redundancy in design. In order to mitigate overall risk, the spacecraft design uses full redundancy. The original LEO+ study used a launch date of July 2006, which corresponds to a technology cutoff date of 2003. This means that all technology items must be at a TRL of 6 by the beginning of Phase C/D. Another constraint is that the spacecraft must survive through the short eclipse seasons that occur each year. The power systems were designed to meet that requirement. Additionally, the LEO+ orbit radiation environment is somewhat more harsh than LEO. For study purposes, we assumed a radiation value of 24 krad behind 100 mils per year, with a radiation design margin of two. The current mission was designed for the use of a Delta II launch vehicle. The spacecraft would need either a two-axis gimbal High-Gain Antenna (HGA) or two antennas. These gimbals are required to permit continuous data taking without much performance degradation.

Figure 3.7
LEO+ spacecraft
block diagram
showing the
subsystems.



Spacecraft Description

The LEO+ system concept has been formulated to keep overall costs low by using existing commercial designs (hardware and software) to the maximum extent possible. Applying this approach to the entire end-to-end system design has kept the spacecraft requirements in a range that can be satisfied by any one of several readily available satellite busses that can be obtained from industry. To minimize cost and development schedule, the approach is to use existing designs with

limited modifications to support the mission characteristics. The system design requires the bus to provide the following functions:

- Radar instrument commanding
- Antenna deployment initiation command
- Onboard storage of radar data
- Data handling capacity to accommodate instrument peak data rates
- Data downlink for instrument telemetry
- Global Positioning System data
- Radar instrument power
- Attitude and articulation control
- Capability to handle large instrument

MISSION OBJECTIVE

- mm-level surface change detection accuracy per year (cm-level for any given interferometric pair).
- Six day repeat coverage.
- Global accessibility.
- Five-year mission duration.

MISSION AND INSTRUMENT CHARACTERISTICS

- L-band frequency.
- Single polarization.
- 200-m orbit tube radius.
- Left/right-looking, sun synchronous.
- Up to 20 MHz combined bandwidth split in the 80 MHz available L-band bandwidth to mitigate ionospheric delay problems.
- Incidence angle range 15.4–47.2°.

ORBIT DESIGN

- Baseline six-day repeat orbit of 1325 km.
- 6 am/6 pm orbit baseline.

ATTITUDE CONTROL SUBSYSTEM (ACS)

- Pitch and yaw pointing control to within $\pm 0.05^\circ$ (180 arcsec), 3 sigma. Roll pointing control to within $\pm 0.1^\circ$ (360 arcsec), 3 sigma.
- Pitch and yaw pointing knowledge to within $\pm 0.025^\circ$ (90 arcsec), 3 sigma. Roll pointing knowledge to within $\pm 0.05^\circ$ (180 arcsec), 3 sigma. These are half of the pointing control requirement.
- Pointing stability to within ± 10 arcsec/sec, 3 sigma per axis. This supports the pointing control requirements.
- Repeat orbit position to within 200 m, 3 sigma.
- Real-time orbit position knowledge to within 20 m, 3 sigma, which supports the repeat orbit position requirement.
- Slew about the roll axis through 64° within 5 or 10 minutes.

COMMAND AND DATA SUBSYSTEM (CDS)

- 100 Gbits / orbit average.
- Two orbits storage.
- 150 Mbps data rate.

INSTRUMENT POWER

- 10 kW peak RF output.
- 2936 W DC input in science mode, 66 W in standby mode (3816 W with 30% uncertainty, 85 W with 30% uncertainty).

STRUCTURES

- SAR antenna consists of rigid honeycomb panels with back-up truss, 13.5 × 3.5 m deployed, stowed in 1.35 × 3.5 × 1.5 m assuming 10 panels.
- 433 kg mass estimate (current best estimate with no contingency) for SAR antenna panel.
- Total instrument mass estimated to be 493 kg, including the RF antenna and data electronics boxes (641 kg with 30% contingency).

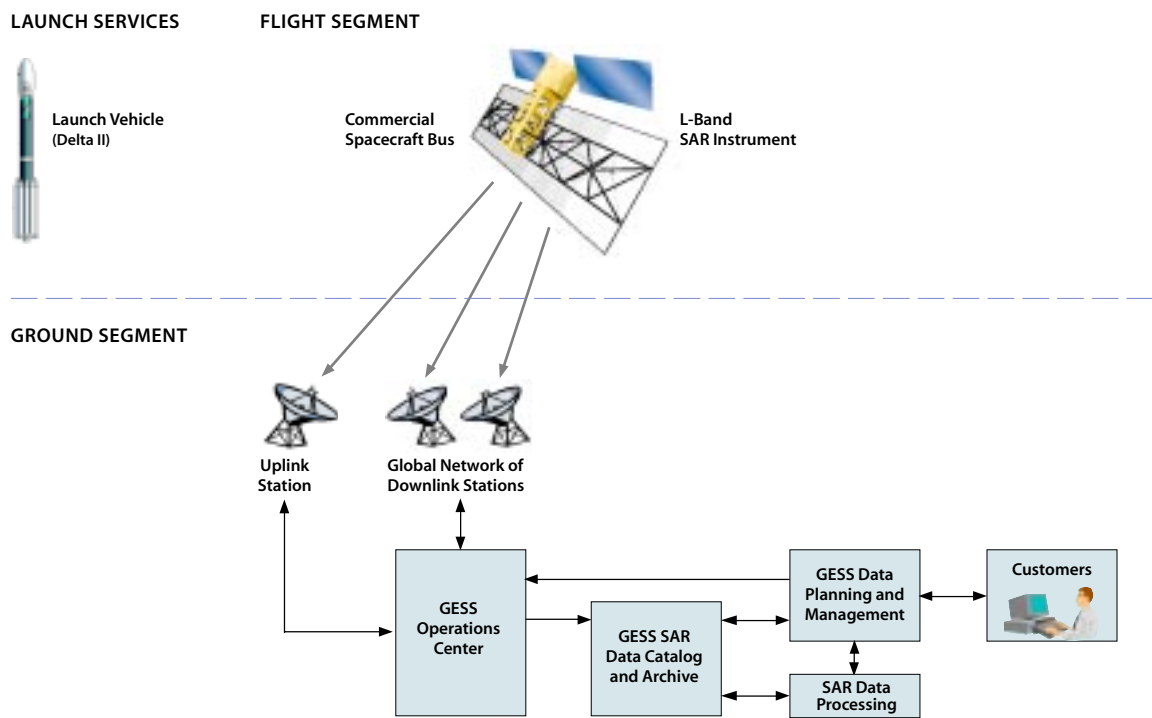
TELECOM

- Support a minimum data rate of 105 Mbps (preferably 320 Mbps using two channels at 160 Mbps), into 11.3 m ground stations in South Dakota (EROS Data Center), Alaska (Alaska SAR Facility), with Svalbard, Norway as backup.
- Provide a low-rate S-Band TTC link.

PROPELLUTION

- Provide 143 m/s of velocity for a 1500-kg spacecraft (based upon assumed bus mass and Team X estimates).
- Provide 20 kg for miscellaneous attitude control functions.
- Unload reaction wheels if necessary. Normal unloading is by torquer bars.
- Provide initial tipoff rate reduction during launch.
- Provide many very small orbit correction maneuvers similar to TOPEX.
- Functional redundancy.

Figure 3.8
System elements
for launch, flight,
and ground
operations.



A survey has been completed that indicates several manufacturers can supply satellite busses that meet or exceed the LEO+ requirements with little or no modifications to existing designs. All of the busses surveyed have substantial flight heritage and utilize space qualified components and technologies. Some of the available busses are production-oriented designs that will provide substantial cost and schedule efficiencies. The cost-saving approach for selecting a bus for nominal design requires that the bus requires little modification, has substantial space flight heritage, is compatible with multiple launch vehicles, has redundancy and sufficient margins to accommodate unexpected changes in the designs, uses radiation-hard standard or commercial parts when possible, and has well-defined interfaces to allow parallel development and testing of the instrument.

Launch Vehicle

The LEO+ launch vehicle will be obtained by the NASA Expendable Launch Vehicle Office and provided to the project using NASA ELV Office procurement and quality assurance processes. The NLS-Medium launch vehicle (Delta II) was assumed, as it can place the spacecraft into the desired orbit (Figure 3.9). A Delta IV would provide ample mass and volume margin.

Assembly, Test, and Launch Operations (AT&LO)

Once the LEO+ system design is complete and has passed the critical design review (CDR), production of the major elements will proceed concurrently. The spacecraft bus, radar instrument, and ground segment systems and their components will complete a rigorous test program during development and build-up for flight. All subsystems will

be thoroughly tested prior to delivery to AT&LO (Figure 3.10). The objectives are to verify system level requirements, functional interfaces, and nominal performance of the integrated flight segment configuration in flight-like conditions.

The main objectives for AT&LO are:

- Provide an integrated, test validated, flight-ready space segment consisting of the spacecraft bus, radar instrument, and launch vehicle, which is capable of being launched on the scheduled launch date.
- Plan and implement traceable, repeatable, and comprehensible test activities.
- Demonstrate an ability to support the spacecraft and the mission objectives with functionally validated ground operations and data processing systems.

The AT&LO program shall test or demonstrate the following:

- Compliance of the integrated flight segment with system-level design and functional requirements.
- Nominal flight segment performance in ambient and expected environmental conditions (of launch and flight), with baseline representative operational sequences; and, predictable performance in selected contingency conditions.
- Compatibility with the launch vehicle and launch systems interface requirements.
- Compatibility with the ground segment and operations systems.
- Verified spacecraft capability to receive and process commands, and to clock out execution time for commands or command sequences that cannot be fully tested in ambient/ground environments.

In addition to traditional integration and test support, the AT&LO organization will also support a postlaunch on-orbit commis-

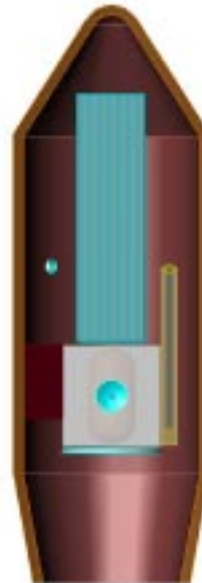


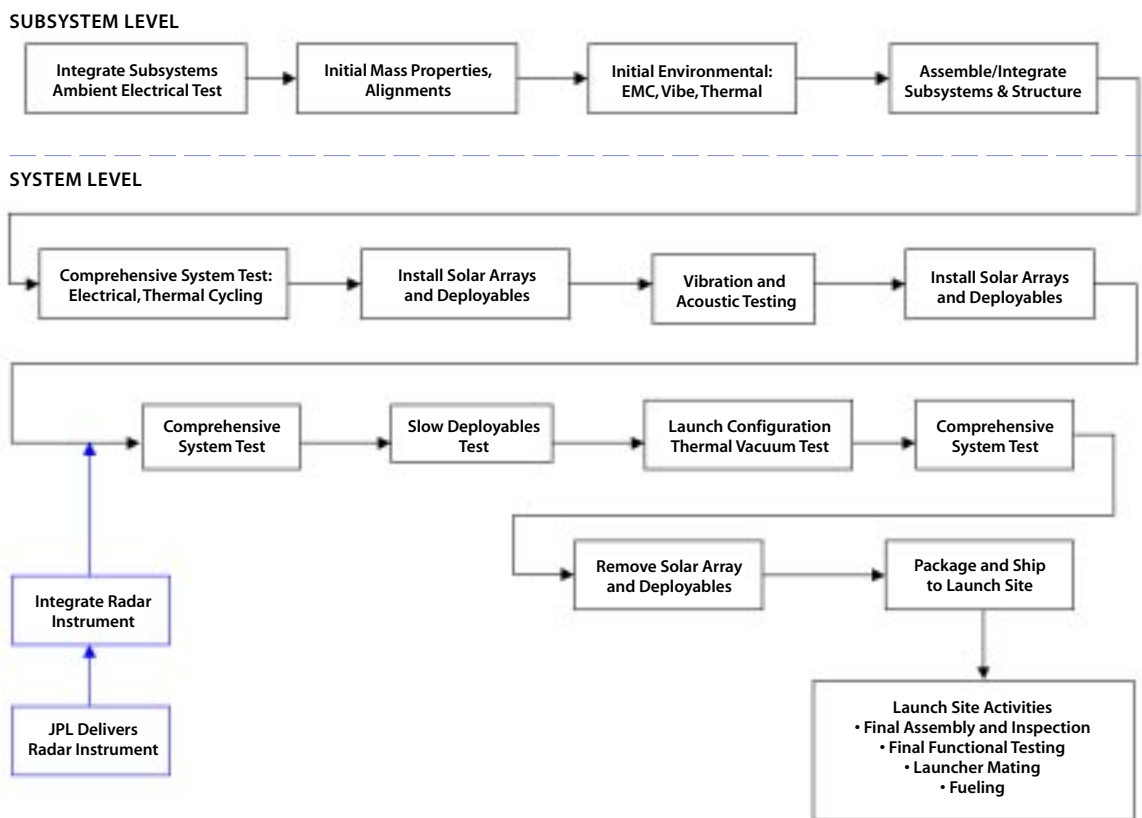
Figure 3.9
The LEO+ payload in stowed configuration in a Delta II launch vehicle fairing.

sioning phase to checkout and calibrate the end-to-end flight and ground system. The AT&LO activity will conclude upon completion of the operational acceptance review, which occurs at the end of the commissioning phase.

AT&LO Approach

The AT&LO approach targets several areas, including the early use of a system testbed to evaluate and confirm avionics architecture and end-to-end Information System design in order to avoid surprises and risks later in integration and testing (I&T). The spacecraft bus manufacturer will be responsible for the spacecraft bus I&T, and will deliver a fully integrated and tested bus. The radar system I&T would follow the incremental build and test approach. Final flight element I&T would be conducted at the spacecraft bus contractor facility. No thermal/vacuum tests at system level, no post-environmental antenna deployment test, and only limited mechanical/integrity verifications

Figure 3.10
Satellite integration and test flow.



are assumed. There will be maximum use of system engineering in other WBS elements. The launch will be from the Western Test Range (Vandenberg Air Force Base).

Ground Data System and Products

The GESS Ground Data System (GDS) is designed to support the disaster management community (Figure 3.8). Specifically, the data latency for disaster response is two hours or less for time-tagged raw data and six hours or less for Level 1 data products, which could be utilized directly by the disaster response teams. Two downlink stations are planned to capture all the raw data being acquired, the EROS Data Center (EDC) in South Dakota and the Alaska SAR Facility (ASF). The Svalbard Ground Station in Norway will serve as a backup downlink station. EDC

would be the central data archiving and processing center, whereas another center, such as JPL, would serve as the GDS development site and backup data archiving and processing facility. JPL would have the capability to handle both the standard data product delivery as well as special event product generation. Level 0 product generation may be done at the downlink station and transmitted directly to the users when needed to reduce the data transmission overhead via EDC.

In the following section, we will summarize the ground data system requirements and corresponding design impact on the GDS for the LEO+ mission. We will describe the output products based on inputs from the seismology community. Next, we describe the external interfaces to the GDS and the distributed software architecture. The distributed nature and

scalability of the GDS architecture designed for the LEO+ mission can be easily expanded to support a geosynchronous mission. We describe the hardware architecture of the GDS, which is composed entirely of commercial off-the-shelf (COTS) products.

Ground Data System Requirements

Based on the functional requirements for the LEO+ mission, the ground data system requirements and design impacts are summarized in Table 3.4.

Data Product Definitions

Two primary user communities with different requirements will be supported: those with radar processing capabilities, and researchers relying on geophysical Level 2 products. The former group of users would request the raw radar data to process themselves. In addition, they will need ancillary data for the purpose of calibration such as the removal of atmospheric effects. The second group of researchers who have no interest or capability to process their own radar data prefer to work directly with the geo-coded differential interferograms to extract the deformation measurements. Therefore, as shown in Table 3.5, the data products are defined to serve both of these user communities.

All level data products have accompanying metadata, which includes the ancillary data and quality, calibration, and processing parameters. Quick-look data (without corrections) will also be available. Ancillary data needed for processing includes:

- Satellite orbit information derived from onboard GPS
- Ground reference GPS (from mission operations)

- Atmospheric path delay model (from meteorological services)
- Ground truth data (from external sources) necessary for calibration

Browse products will be generated for all Level 1a, 1b, and 2 products. Ancillary data may be bundled with any level data product delivery.

Ground Data System Interfaces

The GESS GDS is an integrated SAR processing, product delivery, and archiving system. The GDS interfaces with the following components:

- Spacecraft operations
- Science users
- Program management
- Algorithm developers and calibration engineers
- Ancillary data sources

The high-level GDS boundaries and external interfaces are shown in Figure 3.11.

Spacecraft operations provide satellite-tasking information (instrument on/off times and modes) to the GDS. This information is catalogued, used for internal processing and made available via a Web-based GIS interface (interactive map) and subscription. It also provides ground station tasking and downlinked data. Science users access the GDS through a Web portal. This portal provides product and processing request capability, as well as other features such as data mining and education and outreach. Program management accesses the GDS through a Web portal to view metrics and provide processing priorities etc. Algorithm developers submit basic algorithms and refinements through a Web-enabled configuration management interface. The GDS actively acquires and ingests ancillary files required for product processing.

Table 3.4
Ground data system requirements.
Based on the functional requirements for the LEO+ mission, the ground data system requirements and design impacts are summarized here.

REQUIREMENTS	DESIGN IMPACT
At least two downlink stations	Distributed system architecture Secure and reliable network connections Process raw data at more than one location
Duty cycle up to 20–25%	200–250 Gbits of data per orbit Parallel processing environment Distributed high-speed storage devices
13 orbits per day and six days in a repeat cycle	Online real-time data storage over 30 TB of data Six days' worth of data available on line
Fast downlink (320 Mbps) required	Network upgrades at ASF and Svalbard Identify other possible stations
Single Data Archiving Center with a backup site	Develop operational concepts with EDC Design near online storage devices Use of DVD and high density magnetic media with jukeboxes
System interfaces to those with radar processing capability and individual researchers without the capability	Develop capability to interface with various data access methods Fault tolerance with real-time data delivery Support special orders of various level products
Access to ancillary data	Negotiate interfaces with ancillary data providers Develop redundant interfaces during emergency
Level 0 in compliance with EOS-HDF	Develop metadata standards Participate in HDF version 5 development
Latency for time-tagged raw data is 24 hours	320 Mbps downlink reception capability
Latency for calibrated data products is six days	Parallel/Beowulf/clustered processors Smart online data management system Reliable interfaces to ancillary data repositories
In emergency, two hours for raw and six hours for Level 1	Capability to handle special processing
Easy to use user interface	Data mining Web interfaces to access data Single interface to access all data levels Data and metadata standards
Five-year mission lifetime	Reliable system maintenance and upgrades Develop cost-effective operational concept

LEVEL	DEFINITION
0	Reformatted raw signal data with associated radar headers.
1a	Processed single-look complex (SLC) data, browse imagery from multi-look SLC data, browse interferogram generated with most recent data-take from archive, and associated radar headers.
1b	Interferogram and correlation map with associated radar headers.
2	Calibrated three-dimensional displacement map in standard map projections.
Ancillary data	Satellite orbit information derived from onboard GPS data and ground reference GPS stations (from mission operations), atmospheric path delay model (from meteorological services), and any ground truth information (from external source) necessary for calibration. May be bundled with any level data product delivery.

Table 3.5
Data products
definitions.

Software Architecture

The software architecture supports a distributed implementation allowing for any number of receiving stations to be integrated into the system. In addition, this architecture is scalable in order to meet the performance requirements of a LEO+ mission or a geosynchronous mission. Additional designs may also be studied. Alternate architectures such as a direct broadcast approach may be viable, if data quality and calibration can be ensured.

The current design will allow for one or more ground data systems to be deployed. All ground systems will contain the same software, and will be configured to archive products long term at the EDC, the central data archiving center. The EDC will contain that master catalog of data products acquired throughout the mission and will include both online and offline storage of the data products and metadata. Ground receiving stations will be capable of receiving the products, performing basic data processing, and archiving the products at the EDC.

The product catalogs will be designed to reside on one or more hosts allowing scala-

bility in the catalog. A typical scenario would be to build three product catalogs representing L0, L1, and L1+ data products. The data products will be stored on a network attached storage (NAS) file system so that the data products always appear local to the system creating an online archive.

Two key user interfaces will be created. The science user interface will allow scientists to enter product requests. Requests for previously captured data takes will be processed and products staged for download by the data distribution function. Requests for products that have not been acquired will be recorded by the system and scheduled for notification and distribution to the user once acquired. In addition, an operational user interface will also be created which will allow system operators to manage the data system.

In addition to the principal site of EDC, the software will also support the creation of a replicated site in the event that the EDC is unavailable. The replicated site will allow for products to be archived and queried at that site should the EDC be unavailable. The replicated site will contain a short-term “online”

archive. Should the archive be unavailable, products will be captured by the replicated site, and then moved to the EDC once available. The site will also contain a master copy of the catalog indicating what products are available in the system.

Hardware Architecture

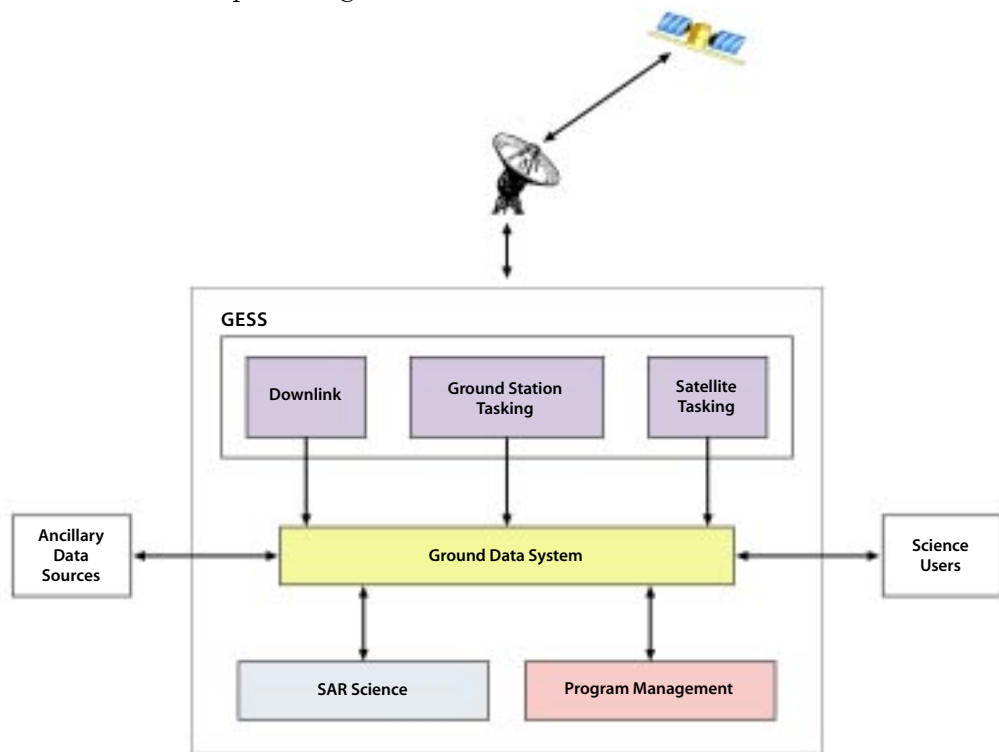
The GDS hardware system is composed of COTS products utilizing COTS operating systems. The hardware architecture is scalable in order to meet the performance requirements of a LEO+ mission or a geosynchronous mission. The physical interface between co-located machines is a high-speed switched network, now specified as Gigabit Ethernet but soon to be 10x Gigabit Ethernet. The design is also adaptable to the new InfiniBand architecture, a high-speed I/O protocol that is five times or more faster than the 10x Gigabit Ethernet, when it becomes widely available. Ground stations and the processing centers

communicate through the Internet at the highest available bandwidth connections provided by the NASA Integrated Services Network (NISN) or commercial providers. The hardware system supports fully distributed processing, access, and control. The database is fully mirrored at an off-site location and is continuously updated. The main repository and archive for the database, online processed products, and long-term archived L0 product will be centralized at EDC. Mirror sites and Web caching at multiple locations will facilitate periods of high demand access to processed products.

Operational Scenario

The GESS GDS is fully responsive to the published operational scenarios. The GDS will be operated and serviced by EDC once the GDS system is delivered. The operational

Figure 3.11
Ground data
system boundaries
and interfaces.



and service concepts will follow the current model of EDC.

Through the GDS Science and Management interfaces, processing priorities will be set (as in the case of the response to a targeted seismic event) and the processed products from the various mapping campaigns will be segregated into virtual collections for distribution and browsing (Table 3.6).

Geosynchronous GDS

To scale the GDS to support a geosynchronous mission essentially increases the duty cycle from 25% to 100% radar on-time. This increases the procurements and downlink costs significantly and would more than double the cost of the LEO+ system described here.

Mission Cost

The total mission cost for the LEO+ system is in the range of \$400–500 million. The JPL Project Design Center (PDC), also known as Team X, which is a concurrent engineering process for proposal development and mission definition, developed the spacecraft and mission costs. The Team X subsystem engineers used grass-roots estimates and parametric models to estimate the costs. The basis of the L-band SAR instrument is a grass-roots estimate developed by experts from the JPL Radar Science and Engineering Section. The following assumptions apply to the costs:

- All costs are in FY02 \$M.
- The mission starts in September 2003.
- The mission launches in August 2006.
- Phase A is nine months, Phase B is 12 months, Phase C/D is 25 months, and Phase E is 60 months.
- This is a Class-B mission using commercial and military 883B parts.

FIRST 6 MONTHS	
14 days	Checkout
36 days	ScanSAR Global
36 days	ScanSAR Extended Beams Global
48 days	High-resolution (Strip) Targeted areas
48 days	High-resolution (Strip) Extended Beam Targeted Areas
<i>Total 182 days</i>	
RECURRING 6 MONTH SCENARIO	
36 days	ScanSAR Global
144 days	High-resolution (Strip) Target Areas

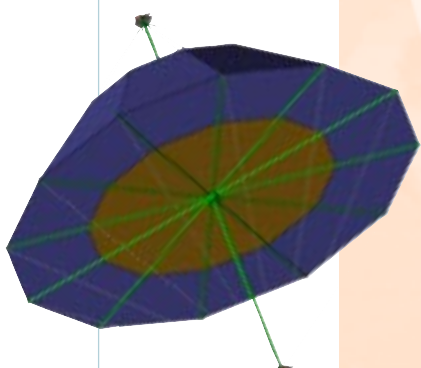
Table 3.6
Ground data
system operational
scenarios.

- It will have full redundancy for a five-year mission duration.
- The spacecraft will be supplied by industry and built as a protoflight. The instrument will be built by JPL.
- Phase A, B, C, D, E will have 30% reserves. There is no reserve on the launch vehicle cost.

These cost study results should be considered a departure point for more in-depth study. By iterating the science requirements with the user community, and the mission design with mission architects, significant cost reductions may be available. Identifying descope options is an important first step in this process. Additional cost savings, as well as additional mission value, should be explored through partnerships with other government agencies (such as NPOESS, DoD) and international programs, including ground stations and flight elements.

Geosynchronous Architecture

CHAPTER FOUR



The most ambitious concept of the GESS study entails the operation of a geosynchronous SAR constellation. While the deployment of such a constellation would be a massive undertaking and require that major technological challenges be overcome, a constellation of high-altitude SAR satellites would offer advantages over lower-altitude sensors in the contexts of system operational flexibility and instantaneous accessibility of target areas on the ground (Figure 4.1). A system with such capabilities might be considered as a mission for the next decade.

Geosynchronous orbits are unique because their orbital periods are equal to one Earth day. A geostationary orbit is a special kind of geosynchronous orbit in which the orbital inclination is zero; viewed from the rotating Earth, a satellite in a geostationary orbit appears to remain fixed in the same position in the sky at all times. This property makes geostationary orbits ideal for such applications as communications and meteorology, but it in fact makes them unusable for SAR missions. This is because the principle of aperture synthesis — the very principle for which SAR is named — requires relative motion between the sensor and the scene under observation. When such motion exists, as it does for an inclined geosynchronous orbit, however, fine resolution can be obtained even from very great distances. Although a geosynchronous satellite follows an elliptical trajectory as dictated by Kepler's laws of motion, due to the relative motion of the Earth and the satellite, the nadir point traces out a "figure-8" pattern on the ground once per day (see Figure 4.2). Since radar instruments can also acquire images both during the day and at night, and unaffected by cloud cover, a high-altitude SAR constellation may be well suited to the task of 24-hour global hazard monitoring. Most of the Earth's surface could be kept in view nearly continuously by a constellation of geosynchronous satellites.

System Parameters

A geosynchronous SAR at an altitude of about 35,800 km would be more than an order of magnitude farther from the Earth than any SAR mission to date. While this high-altitude vantage point would allow a geosynchronous SAR to view a large ground area, it would also require a large physical antenna and a great deal of transmitted power. The antenna size requirements are driven by the need to resolve the range-Doppler ambiguities that are inherent in a pulsed radar system; the power requirements are driven by signal-to-noise ratio (SNR) considerations.

We envision a system with a 30-m-diameter L-band aperture antenna that transmits 60 kW of peak power over relatively long 1-ms pulses. The boresight of this antenna would be kept pointed in the nadir direction and the beam steered electronically to look either left or right. Any part of the sensor footprint could be illuminated with no more than $\pm 8^\circ$ of electronic steering — from this altitude, the limb of the Earth is only 9° from nadir. Data could therefore be acquired for

areas between 1000 and 6500 km ground range from nadir on either side of the platform ground track, corresponding to ground-incidence angles of $10.6\text{--}66.4^\circ$. The antenna could also be steered to areas with ground squint angles up to $\pm 60^\circ$ on either side of the ground track with less than $\pm 8^\circ$ of electronic steering in the azimuth direction.

With such a wide swath, some of the system parameters would have to change a great deal between the near range and the far range. The bandwidth of the system might vary between 80 MHz at the steepest incidence angles to 10 MHz further out. A split-spectrum approach might be employed as in the LEO+ case in order to characterize the effects of the ionosphere. The signal polarization might also change over the sensor footprint. We envision that the spacecraft would be yaw steered to keep the antenna in a nominal HH polarization state for broadside acquisition geometries, implying that the polarization state would be mixed in squinted geometries.

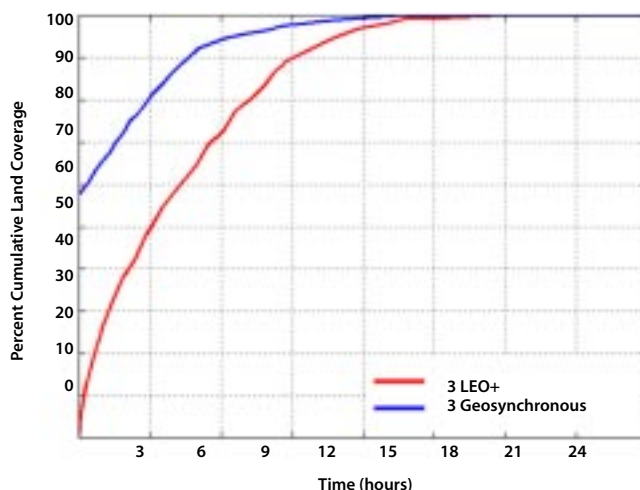


Figure 4.1
Cumulative land coverage from both LEO+ and GEO constellations of three satellites. The GEO constellation achieves over 90% land coverage in approximately half the time of the LEO+ constellation.

Figure 4.2

Trace of a geosynchronous satellite at a 60° orbit inclination (shown as figure-8). Instantaneous field of view for a 5500-km SAR swath is also shown.



Other system parameters would change over the platform orbit as the velocity of the platform relative to an observer on the Earth varies. For an orbital inclination of 60°, the relative velocity of the satellite would vary by a factor of two between about 1500 m/s when the satellite is at high latitudes and 3000 m/s when it is over the equator. The pulse repetition frequency (PRF) of the system would therefore vary between about 125 Hz and 250 Hz. Relevant system parameters are summarized in Table 4.1. Note that these relative velocities and PRFs are significantly lower than those of LEO systems.

Orbit, Coverage, Constellation

Although a geosynchronous SAR would have a very large footprint, its “figure-8”

ground track would always remain in a fixed set of longitudes. A single geosynchronous sensor would consequently be unable to provide global coverage on its own. While the longitude-locked behavior of a geosynchronous SAR might prove advantageous if the mission objective were to provide coverage only of the Western hemisphere, the aim of this study has been the development of system whose scope is global. Consequently, we concentrate here on the use of multiple geosynchronous sensors.

One architecture would be a constellation of ten satellites divided into five groups of two (Figure 4.3). The two satellites in each group would follow the same ground track and would be phased 180° apart, resulting in an interferometric repeat time of 12 hours. In

ORBIT	
Altitude	35788 km
Inclination	60°
Interferometric Repeat Period	1 day
VISIBLE SWATH	
Look Angle	± 1.6–8.0°
Ground Incidence Angle	±10.6–66.4°
Ground Range From Nadir	±1000–6500 km
Slant Range	35892–39224 km
Ground Squint Angle	±60°
Footprint Area	79,000,000 km ²
Subswath Width	400 km nominal
INSTRUMENT	
Antenna Diameter	30 m
Electronic Steering	±8° in azimuth and elevation
Wavelength	24 cm (L-band)
Polarization	varies with squint angle
Peak Transmit Power	60 kW
Pulse Duration	1 ms
Bandwidth	10–80 MHz
Pulse Repetition Frequency	125–250 Hz
PERFORMANCE	
Ground Range Resolution	20 m nominal
Stripmap Azimuth Resolution	varies over orbit (2–20 m nominal)
Nominal SNR	10 dB
Nominal Range Ambiguity Level	-30 dB
Nominal Azimuth Ambiguity Level	-20 dB

Table 4.1
Geosynchronous parameters.

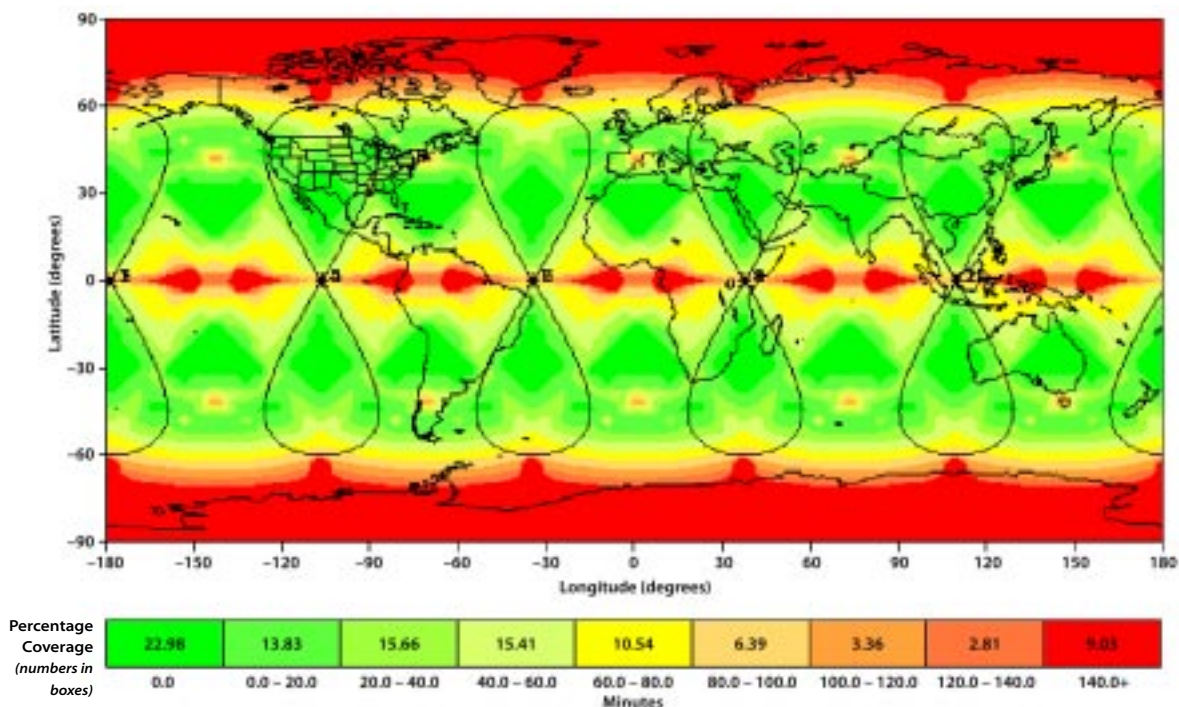
our initial analyses, we assume that the five groups would be equally spaced in longitude, though in an optimized constellation design, the groups might be unevenly spaced for better performance over high-priority areas. Each satellite would be in a nearly circular geosynchronous orbit with a 60° inclination.

At any given time, this ten-satellite constellation would have about 80% or more of the Earth's surface in view. Approximately 20% of the surface would be in view of one or more satellites continuously, and approximately 80% of the surface would be in view nearly continuously (about 90% of the time). Gaps in coverage would be less than one hour for about 70% of the surface to less than five hours for 100% of the surface. The areas associated with longest gaps in coverage would be located mainly near the poles

and at certain longitudes near the equator. For a great majority of the Earth, a 20-m resolution image could be acquired on average within 10 minutes of an emergency event.

The 3-D displacement accuracy of the system would be excellent (Figure 4.4). Because the antenna beam could be squinted both forward and backward via electronic steering, data could be acquired from a great diversity of viewing angles. Moreover, because a target area could be viewed for long periods of time, a great deal of data could be acquired of this area, albeit at the expense of acquiring data of other areas. Typically, hundreds of images of a target area could be acquired during each interferometric repeat cycle. These data could be combined in a least-squares estimation procedure in order to reduce noise induced by

Figure 4.3
The maximum
revisit time for a
constellation of ten
GEO satellites, five
ground tracks,
12-hour phasing, at
an inclination of 60°.



temporal decorrelation and tropospheric and ionospheric effects. We expect that 3-D displacement accuracies of a few millimeters could be achieved in 24–36 hours.

Instrument Modes

Most of the time, full-resolution capability would not be required. Rather, the instrument might instead be operated in various interferometric ScanSAR modes that could yield data over swaths thousands of kilometers wide (each subswath would be up to 400 km wide). Because the antenna beam would be electronically steered exclusively, data could even be acquired from nonadjacent subswaths—perhaps on opposite sides of the ground track—or from beams squinted

both forward and backward. The large antenna footprint would make ScanSAR ground patches hundreds of kilometers wide in the along-track dimension. Moreover, with ScanSAR bursts up to several minutes long, the instrument operation could easily be timed well enough for repeat-pass ScanSAR interferometry. Alternately, the instrument could operate in a standard stripmap mode, or the antenna beam could be steered to dwell on particular areas of interest in a spotlight mode so that large amounts of high-resolution data from various viewing angles could be collected over key seismogenic areas. Between these different modes, the instrument would allow great flexibility in operation.

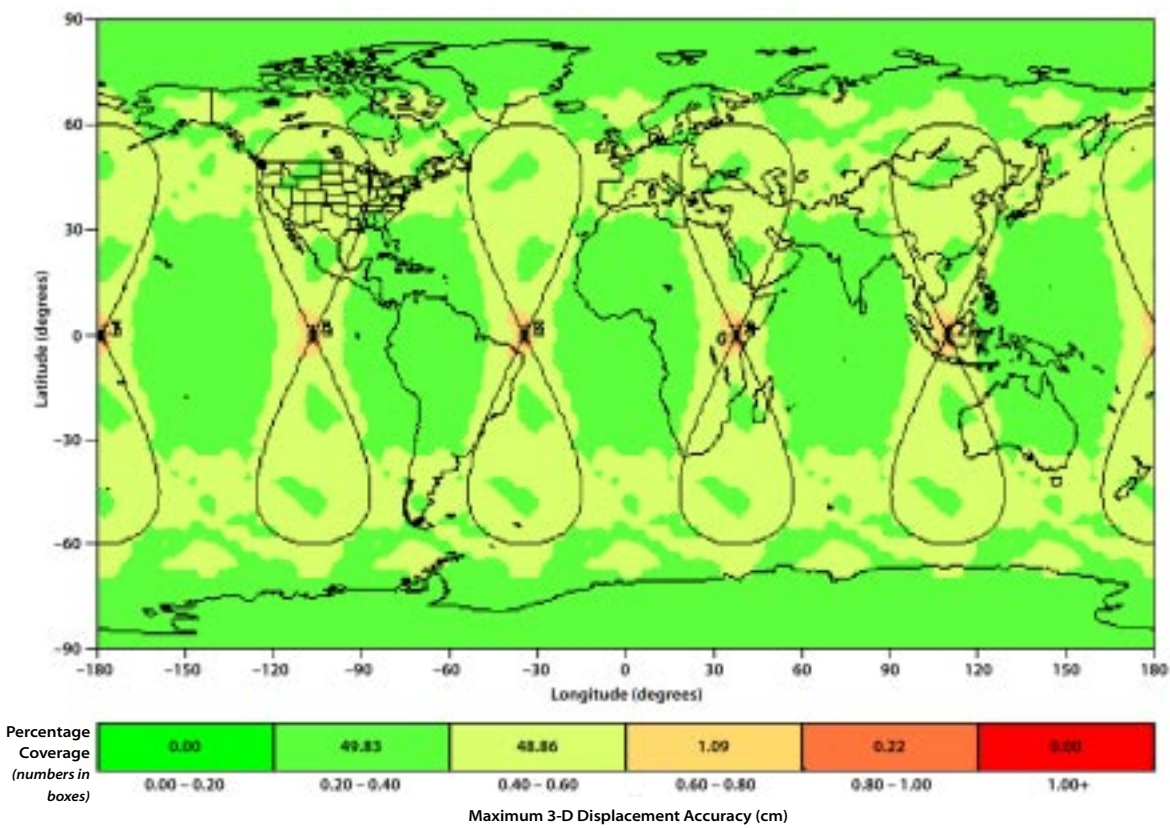


Figure 4.4
Worst-case component of the 3-D vector displacement accuracy for a constellation of ten geosynchronous SAR satellites. The units are relative to the single-image line-of-sight displacement accuracy. For each satellite pass, an image is assumed to have been acquired of the visible ground points every 30° in ground-point azimuth.

The system might have numerous modes that are tailored to different situations and changing priorities. A typical operational plan might involve the daily or twice-daily creation of multiple maps of certain high-priority seismogenic areas (as described in the LEO+ scenario) as well as low-resolution global maps every few days, or high-resolution global maps every few weeks. The operational plan could also be modified as needed in response to global hazard events and current conditions.

Performance

Because the curvature of the relative platform motion changes a great deal over the orbit, the stripmap-mode azimuth resolution depends on the satellite latitude and location of the target in the sensor footprint. When the instrument is looking towards the outside of each loop in the figure-8 pattern, the stripmap-mode azimuth resolution can be as coarse as 20 m, yet it can be finer than 2 m when the instrument is looking towards the inside. That is, in some cases, the orbit curvature would effectively cause the antenna beam to dwell on a particular ground area in a manner similar to that of a spotlight-mode SAR acquisition, even when the antenna beam is kept pointing toward broadside. Azimuth resolutions of around 2 m or better might also be obtained anywhere in the swath or along the orbit when the instrument is operating explicitly in spotlight mode.

The processing involved for attaining 2-m resolution would not be trivial, however. The required synthetic aperture length for such a resolution would be more than 200 km, over which the curvature of the platform motion would change significantly.

In fact, a different azimuth-compression reference function would be required for each along-track sample position. Moreover, the slant-range depth of focus might be even smaller than the nominal slant-range resolution of around 10–20 m if 2-m resolution is desired. Another difficulty of high-resolution processing would be posed by the variability of the ground scene and of the atmosphere over the time required by the satellite to traverse the long synthetic aperture distances; up to 25 min may be required in some situations. In practice, 2-m resolution may be very difficult to achieve, though 5–10-m azimuth resolutions should be readily attainable. Note that while fine spatial resolution is not always required for geophysical applications, high-resolution data can be averaged spatially in order to mitigate the effects of temporal decorrelation in interferometric data.

Indeed, as in the LEO+ case, we expect that the interferometric displacement accuracy will be limited more by temporal decorrelation as well as by tropospheric or ionospheric effects than by the instrument performance. Given the large amount of data that a geosynchronous system can acquire of a targeted area over a short period of time, though, it is not unreasonable to expect that with sufficient averaging, the displacement accuracy can be reduced to the level of a few millimeters for specific target sites. Over larger areas, we expect that subcentimeter displacement accuracies would be typical.

The instrument would also allow for excellent 3-D displacement accuracy over much of the Earth since most points on the ground could be imaged from diverse sets of

viewing angles. This diversity of viewing angles comes from both the lateral curvature of the ground track as well as the variation in ground squint angles that are possible through electronic beam steering from high altitudes.

Data Rates and Volume

Although the footprint of a geosynchronous SAR's accessible area would be much larger than that of a sensor in a lower orbit, the instantaneous data rates of the two would be comparable (on the order of 100–200 Mbs). This is because neither sensor would be able to acquire full-resolution data over its entire footprint simultaneously; data would need to be collected over smaller subswaths. While the subswaths of a geosynchronous SAR would be considerably wider than those of a LEO SAR, the Earth-relative velocity is slower. Despite comparable data rates, because the geosynchronous sensor is almost always in sight of land, even when the sensor itself is over water, the instrument could acquire data nearly continuously. The total data volume could therefore be on the order of 1–2 TB per satellite per day, or around 5–10 PB per satellite over the satellite's relatively long 15-year life. These values would increase by a factor of two or four if multiple radar polarizations were used.

Such data rates and volumes would require specialized downlink and data-handling facilities. Since geosynchronous satellites would be in view continuously from low-latitude ground stations for long periods of time, however, one or two dedicated ground stations could be used to downlink the data from each satellite or each pair of satellites in the same ground track. Furthermore, with appropriate intersatellite communication, one or two

ground stations might be able to handle all of the data from an entire constellation.

Geosynchronous SAR Payload Description

The geosynchronous SAR instrument is dominated by the very large deployable antenna. Because of the large antenna area, our mission concept integrates the SAR antenna with the spacecraft structure and subsystems as illustrated in Figure 4.5. The 30-m-diameter antenna aperture is deployed with horizontal booms and then tensioned to maintain flatness with two asymmetric axially deployed masts and tensioning cables. The antenna aperture is constructed from flexible membrane material that is integrated with the active electronics for proper beam formation and transmit/receive signal amplification. The antenna flatness must be maintained to within 1/20 of a wavelength, or roughly 1 cm across the entire aperture. This type of flatness requirement can be achieved using the axial booms and membrane tensioning cables.

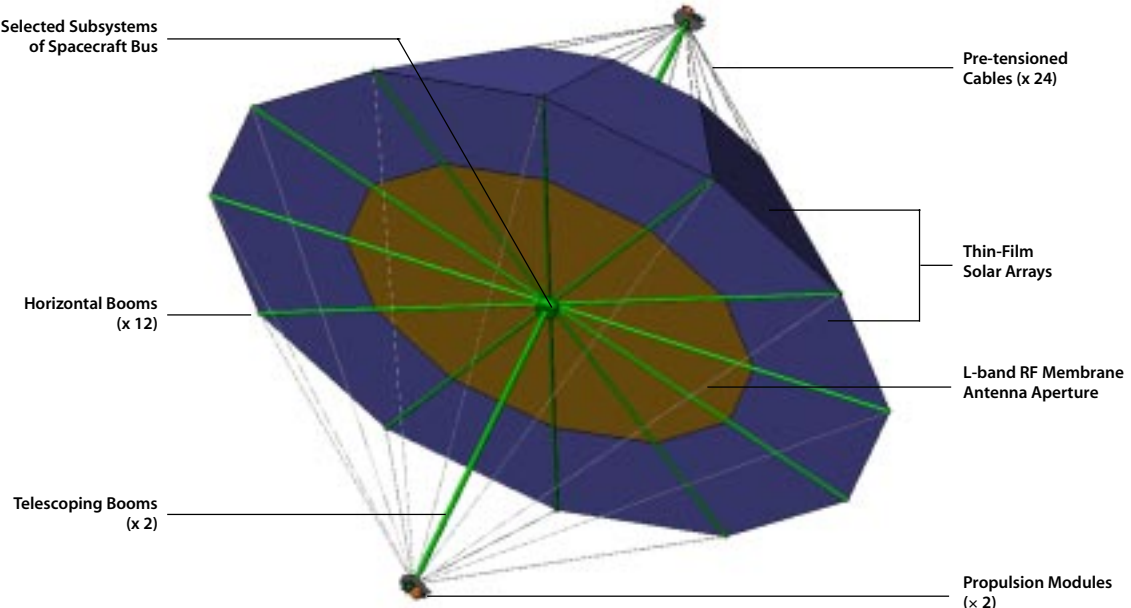
Due to the challenge of such a flatness requirement, the proper calibration of the full array is essential for successful beam-forming. The principal array error sources include feed errors caused by variations in electronic components, and element displacement caused by mechanical deformation of the array surface. The removal of displacement errors is somewhat problematic. Only an external calibration system can address the problem of element displacement. There is a trade-off between mechanical rigidity (and thus, surface accuracy) and mass. In order to minimize the launch mass, it is desirable to tolerate greater

surface errors. The added complexity of an external calibration system must be weighed against the benefit of lighter structural elements. There are several approaches to external calibration. An onboard metrology system (either optical or RF) can be used. Feed errors include all (manufacturing, thermal or aging related) amplitude and phase errors in feed networks, interconnects and T/R modules. There are several proven approaches to compensating for feed errors using loop-back calibration loops. If the feedback paths are properly designed to eliminate leakage from adjacent elements, this calibration can be performed continuously during normal radar operation.

Thin-film solar arrays provide power to the antenna and spacecraft. These arrays are an integral part of the system configuration and share the same structural elements. One solar array is an annular ring formed around

the perimeter of the radar antenna aperture. Solar arrays also partially cover the rear or zenith-pointed side of the spacecraft, stretching up the tensioning cables as shown in Figure 4.5. The solar array “tent configuration” provides a large surface area for solar power collection from any sun orientation but will also result in high solar pressure on the solar arrays making station keeping more challenging and costly. To minimize the effect, we have lengthened the axial boom for steeper angles of the rear-facing solar array. We have also reduced the size of the solar arrays as much as possible. The top of the solar array “tent” is open because the thermal subsystem requires a window to space for radiating excess thermal energy. The power system also includes sufficient batteries to operate for short periods in eclipse. On the tips of each mast are propulsion modules for orbit maintenance. The antenna is mounted

Figure 4.5
Geosynchronous
SAR large deployable
antenna concept.



to a centralized spacecraft bus that also houses the radar central processor/controller.

The high-radiation environment of the geosynchronous orbit poses a substantial risk to the SAR electronics, and degrades the performance and reliability of the solar arrays. Long-term exposure can cause device threshold shifts, increased power consumption, and device damage. Radiation-hardened devices and shielding can mitigate total dose effects. The expected total dose for a 15-year mission behind 30 mils of aluminum is 15 Mrad for a geosynchronous orbit inclined to 60°. Clearly, this presents a major technical challenge. The total dose decreases exponentially with shielding, and therefore the expected total dose behind 100 mils of aluminum is reduced to 600 krad. This becomes a more manageable problem. However, only limited shielding can be employed for the electronics on the antenna. Greater levels of shielding will be very massive and bulky, and perhaps not compatible with membrane antenna technology. Therefore, we consider the radiation environment to be one of the biggest challenges to realizing this system.

A more detailed description of the radar system architecture and antenna design will be presented in Chapter 6. The spacecraft bus contains the subsystems required to perform all spacecraft housekeeping functions and radar control and data handling functions. The bus also supports the deployable booms, masts, antenna aperture, and solar arrays. Twelve horizontal booms deploy, support, and tension the antenna aperture and solar array. These booms each have a fully deployed length of 19 m and are supported by, as well as stowed for launch in,

the spacecraft bus. Self-rigidizable spring-tape-reinforced (STR) inflatable booms of 10 inches (0.25 m) in diameter were selected as the baseline booms. Two high-stiffness, telescoping Able Deployable Articulated Masts (ADAM) developed by AEC-Able provide axial support for the large antenna and solar arrays. The masts will be deployed axially from the top and the bottom of the spacecraft bus. The masts are asymmetric; the nadir-pointing mast has a fully deployed length of 19 m and the upper mast used to support the solar arrays has a length of 38 m. This configuration was chosen to maximize solar array efficiency and to reduce mass and solar pressure effects. Each ADAM mast has a linear mass density of 1.3 kg/m and is stowed in a dedicated canister for launch. The canister for stowing the upper ADAM mast also acts as the central mandrel for packing the antenna aperture. This means that the membrane aperture will be wrapped around the upper canister for launch. The antenna aperture is formed by three layers of thin-film membranes. The 30-m-diameter membrane antenna aperture is integrated with all of the distributed transmit, receive, and control electronics including T/R modules, true-time-delay (TTD) digital transceivers, power converters, and signal-distribution and interconnect technologies. Twenty-four pre-tensioned cables are used to stiffen the horizontal booms. The upper ADAM mast supports 12 of these cables, and the lower ADAM mast supports the other 12 cables. The solar arrays that provide all power for the instrument and spacecraft housekeeping functions are made with flexible, amorphous thin-film technology that is 13% efficient. The areal mass density of these solar arrays

is assumed to be about 0.63 kg/m^2 . The front annular-ring-shaped solar array will be packaged for launch and deployed in space together with the membrane antenna aperture. The rear arrays will be deployed and supported by the 12 upper cables. Two propulsion modules are located at the tips of the ADAM masts. Each propulsion platform consists of hydrazine thrusters, solar-electric ion propulsion engines, and supporting elements of the propulsion subsystem.

The total dry mass of the integrated geo-synchronous SAR flight system is roughly 4500 kg (with contingency). A breakdown of mass and power is provided in Table 4.2.

The geosynchronous SAR integrated flight system will be packaged for launch as shown in Figure 4.6. The total launch stack height is 8 m, which will fit in a Delta IV fairing. The large antenna must be stowable with high packaging-efficiency in order to physically fit into the spacecraft launch vehicle. Since low mass and low stow-volume are driving requirements, a flexible mem-

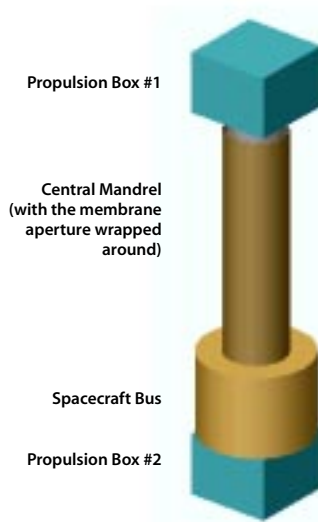
brane antenna architecture was selected. Rigid honeycomb panels, such as that used for SIR-C and SRTM antennas, were not considered due to their larger mass and stowage volume.

Mission Design

Because of the large area of the antenna, our concept of the mission involves the integration of the antenna and the spacecraft structure as just described, with rigidizable booms, deployed radially as illustrated in Figure 4.7. An alternative, more-traditional design involving a separate articulated solar array was examined but not selected because of the mechanical problems involved. The solar arrays of the current working design are sized such that sufficient power would be available regardless of the satellite orientation with respect to the Sun. The spacecraft would also carry enough battery capacity for three minutes of instrument operation during eclipse. This would allow images with azimuth resolutions of 10 m or better to be obtained in emergency situations if necessary. Eclipses would occur once per day during each of two month-long seasons per year, with eclipses of up to 70 minutes duration. The large central opening in the solar arrays over the back of the radar antenna aperture is required for the radiators that would provide thermal control.

Gimbaled propulsion units with both chemical and ion thrusters as well as their propellant tanks would be located on azimuthally rotating platforms at the ends of the main masts. These thrusters would be used for orbit maintenance and for dumping the built-up momentum of the reaction wheels used to provide attitude control and yaw steering. The reaction wheels themselves

Figure 4.6
Major components
of a GEO SAR
flight system.



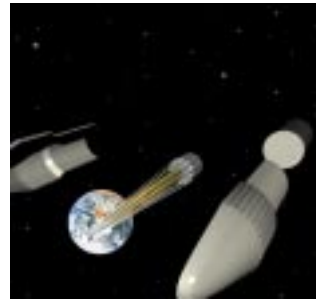
SYSTEM/SUBSYSTEM	NO. OF UNITS	UNIT POWER (W)	TOTAL POWER (W)	UNIT MASS (kg)	TOTAL MASS (kg)
Spacecraft			8226		2810
Spacecraft Bus	1	1091	1091	1166	1166
Flex Solar Array	12	158	1894	76	909
Batteries	2	0	0	214	428
Propulsion Modules	2	2621	5241	154	307
Radar Antenna Structure			0		387
Antenna Membrane Aperture	36	0	0	4.242	152.7
ADAM Mast (nadir)	1	0	0	24.7	24.7
ADAM Mast (zenith)	1	0	0	49.4	49.4
Able Mast Canisters	2	0	0	20	40
Horizontal Boom	12	0	0	9.5	114
End Cap	24	0	0	0.25	6
Radar Electronics			28050		286
Central Processor (CPU)	1	1000	1000	25	25
Digital Receivers	61	50	3050	0.1	6
T/R Modules	15616	2	24000	0.006	94
Feed Probes/Interconnects	15616		0	0.001	16
Optical Fiber Distribution	1		0	30	30
Power Distribution Cabling	1		0	90	90
Power Converters	244		0	0.1	25
Spacecraft Total (Dry)			36276		3482
Contingency (30%)			10883		1045
Spacecraft Total (Dry) with Contingency			47159		4527
Propellant					752
Star 48 V engine for orbit circularization					2455
Launch Mass					7734
Launch Vehicle Capability (Delta IV 4050 Heavy) to GTO					11000
Launch Mass Margin (30%)					3266

Table 4.2
Geosynchronous
SAR mass and
power estimate.

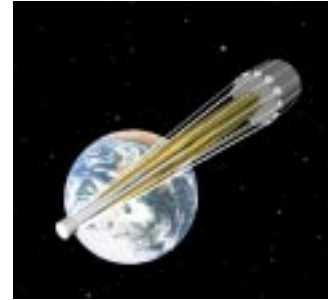
Figure 4.7

The geosynchronous SAR flight system will undergo a four-step deployment sequence:

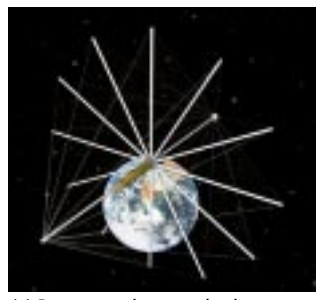
1. The system is separated from the fairing of the launch vehicle. See Figure 4.7(a) and (b).
2. The 12 horizontal booms and the two ADAM masts deploy. See Figure 4.7(c). The 24 tensioning cables also deploy simultaneously with the ADAM masts. These cables will be tensioned to a pre-determined level when the masts are fully extended.
3. The membrane antenna aperture, together with the annular front solar array, start to deploy by the actuation of a set of wire and pulley mechanisms. The various stages of this deployment process are illustrated in Figure 4.7(d) and (e). The fully deployed membrane aperture and ring-shape solar array can be seen in Figure 4.7(f).
4. The rear solar arrays are deployed by a second set of wire-and-pulley mechanisms. Figure 4.7(g) shows the half-deployed cone-shaped solar array and Figure 4.7(h) shows the fully deployed array. It should be noted that in these two figures a full cone is shown for this array; however, the current baseline design uses only a partially filled configuration.



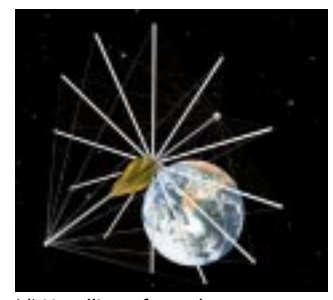
(a) Ejection from the fairing.



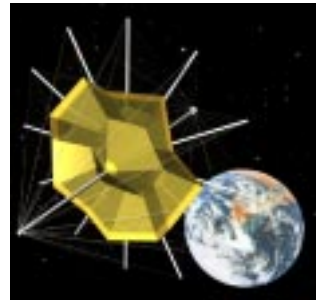
(b) Ready to deploy.



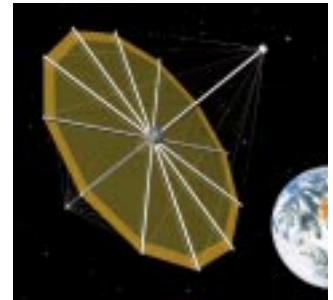
(c) Booms and masts deploy.



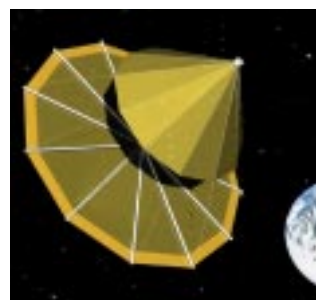
(d) Unrolling of membrane aperture.



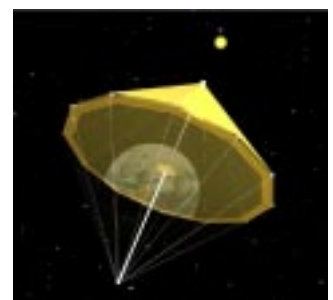
(e) Deploying membrane aperture.



(f) Fully deployed aperture.



(g) Deploying cone-shaped solar array.



(h) Deployed GESS system.

would be located near the spacecraft center of mass. Also located at the end of the nadir mast would be a telecommunications package, including a high-gain antenna, and an Earth sensor for attitude control. The packages located here would be relatively small compared to the size of the radar antenna, so they would not interfere with the operation of the instrument. Precise knowledge of the platform position and attitude would be obtained from the Earth sensor, Sun sensors, star trackers, and a reverse GPS system.

Aside from the technological difficulties posed by the instrument, several key issues need to be addressed in the overall mission design. Because of the great distance of the radar from the Earth and the consequent need for large amounts of power (up to 37 kW DC total for the spacecraft, including 28 kW for the instrument, in addition to power for telecom, solar-electric ion propulsion, but not including contingency), a large area would be required for the solar arrays. Not only would the solar arrays constitute a large fraction of the total spacecraft mass, they would present a large surface area over which solar pressure would exert forces that perturb the spacecraft trajectory and attitude. Several thruster fires per day would be needed to maintain orbit control tightly enough for high-precision repeat-pass interferometry. It is not clear how thruster firings, whether chemical or electric, would affect the flatness of the radar antenna and the subsequent system performance.

The spacecraft mass, including contingency, would be around 4500 kg. In order to maintain an adequate launch vehicle margin of 30%, we require a launch vehicle such as a Delta IV 4050 Heavy, as well as a Star

48 V upper stage (2455 kg). The launch vehicle puts the spacecraft into geosynchronous transfer orbit (GTO), and the Star 48 V provides the apogee burn to produce a final geosynchronous orbit. We further note that more-optimal designs of several subsystems could potentially result in mass savings of at least several hundred kilograms.

Cost

A rough-order cost estimate for the GESS geosynchronous SAR mission concept was derived from Team X cost models and technology projections. With a technology cut-off year of 2010, a 5-year development, and 15-year mission operations, the total cost for the first satellite is in the range of \$1–2 billion. A ten-satellite constellation will cost roughly \$8–10 billion.

Future Opportunities

Seismology from Space Using Ka-Band GEO Satellite

Broadband digital seismometers — the current state of the art in seismology — offer continuous three-component surface displacements with sensitivities in the micron range. Although much of the world is covered with varying densities of broadband seismometers, they remain isolated to discrete point locations.

A satellite-based, continuous measurement of surface displacements with temporal and spatial sensitivities appropriate for seismic waves (submillimeter displacements, 0.01–1-Hz sampling) would represent an important step forward in understanding earthquake physics and solid Earth structure and dynamics. Current models for 3-D velocity structure of the

Earth are based on propagation of seismic waves as measured at discrete points. Spatially continuous mapping of seismic wave phases from large earthquakes would allow great improvements in crustal and lithospheric heterogeneity models, and would be synergistic with current developments in super computing models of 3-D Earth structure and seismic wave propagation (Figure 4.8). Detailed images of complex wave interference would generate significant improvements in basin seismic resonance and earthquake hazard assessment. By seeing the rupture unfold and observing the amplitudes of the seismic waves generated along the rupture, more-precise models would be determined for the rupture dynamics. This should lead to a fundamental improvement in our knowledge of how earthquakes initiate and why they stop.

The development of a radar mission for monitoring seismic waves involves tremendous technical challenges, but it is not outside the realm of possibility as a long-term goal. For now, we assume that the science requirements for such a mission dictate a horizontal resolution of 10 km, a vertical resolution of 100 μm , and a temporal resolution sufficient for following 5 km/s seismic waves.

While most spaceborne imaging radars employ aperture synthesis techniques for obtaining high horizontal resolution, the high-temporal resolution and wide-area coverage requirement of this application preclude the use of such techniques. That is, temporal sampling must occur on time scales finer than those possible for a high-altitude sensor to traverse a synthetic aperture length. Low-altitude sensors would be unable to provide sufficient coverage. We consequently envision a geostationary, real-aperture Ka-band system. That is, in contrast to the geosynchronous

SAR, this platform must be maintained so that it does not move relative to the Earth surface. A constellation of three to five satellites could provide coverage for all equatorial and moderate-latitude regions of the Earth.

A short wavelength is desired so as to maximize the interferometric sensitivity to small surface displacements and to minimize the required antenna area, but the frequency must not be so great as to cause pulse-to-pulse decorrelation through frequency drift. We select the Ka-band frequency of 35 GHz (8.57-mm wavelength) for this analysis as a compromise. Therefore, in order to obtain 10-km horizontal resolution at a latitude of $\pm 60^\circ$, an antenna with a diameter of approximately 110 m is required.

Assuming nominal system parameters, the high antenna gain implies that the single-pulse SNR will be greater than 40 dB for incidence angles up to 68° with 50 kW of radiated power and a normalized backscatter coefficient σ_0 of -20 dB. For this computation, we assume that a 1- μs gated continuous wave (CW) pulse is transmitted. (Range resolution is not required, as successive pulses are to be interferometrically combined.) Thermally induced phase noise will be much less than the 2.2° (25 dB SNR) threshold required for an interferometric vertical accuracy of 100 μm .

Successive pulses for each 10 km ground cell will need to be spaced by approximately 1 s if the wave speed is 5 km/s. Given the time between pulses, tropospheric artifacts may pose a significant limitation on the achievable vertical accuracy of the system (see Chapter 5, Optimizing the Measurement). Over 1 s, the tropospheric delay can vary by approximately 100 μm or more, depending on local condi-

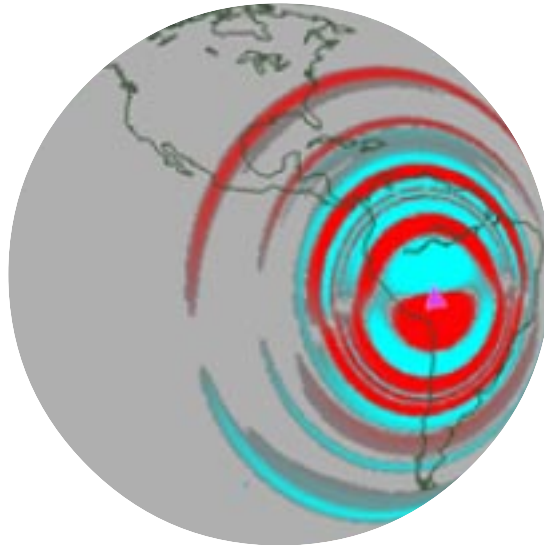


Figure 4.8
Modeled propagation of seismic waves from the deep, magnitude 8.2 Bolivia earthquake of June 9, 1994. The earthquake was so large that it produced a permanent displacement of the surface of the Earth of several millimeters near the epicenter in Bolivia. (Komatitsch and Tromp, 2002)

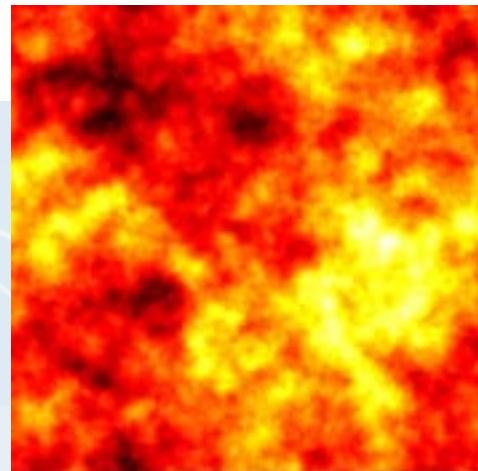
tions. Another factor limiting the system's vertical accuracy may be pulse-to-pulse decorrelation caused by changes of the ground surface between pulses; for example, from disturbances of the local vegetation by the wind. This effect will depend on the scene and its dominant scattering mechanisms at Ka-band. Moreover, it is not clear how the scattering centers of surface features such as vegetation move in response to a seismic wave propagating through the ground.

The total surface area that can be observed by the system during a seismic event is determined by the number of resolution cells that can be scanned within the interferometric repeat time of one second. We assume that the radar antenna is electronically steered to transmit pulses towards different ground cells at a 30-kHz pulse repetition frequency (PRF) during a transmit window equal to the 0.25-s round-trip pulse travel time. The radar

then receives each of the transmitted pulses in turn. The total area covered in 1 second is approximately 10^{12} m^2 , equivalent to a 1200-km-diameter circle.

The most important technological hurdle for such a system will likely be the design, construction, and deployment of a large, high-frequency antenna capable of fast, accurate electronic steering. Advanced onboard processing hardware and algorithms will also be required since the system must detect and respond adaptively to seismic events in real time. Stringent requirements may also be placed on spacecraft control and pointing given the solar pressure exerted on the large antenna.

Note that if the horizontal resolution were relaxed from 10 km to 30 km, the antenna diameter could be reduced by a factor of three, and the area coverage rate would increase by a factor of nine.



Optimizing the Measurement

CHAPTER FIVE

Measuring surface deformation from space at the required accuracy and frequency for earthquake studies constitutes numerous challenges. Methods to improve the measurement capabilities presented in this report include the possibility of using a medium Earth orbit (MEO), and developing ways to reduce the noise from atmospheric effects.

Spectrum of Options: LEO+, MEO, GEO

The mission concepts explored in this study constitute the extremes of a range of options for a global earthquake-monitoring satellite system. The LEO and LEO+ concepts, which have many similarities, are near-term possibilities that entail the use of conventional technology in mission architectures akin to those of existing SAR spacecraft. On the other hand, the geosynchronous concept is an ambitious, far-term possibility that would be dramatically different from any current SAR system in terms of its technology, operation, and performance. A middle ground may be possible, and in fact potentially desirable.

The main differences between the LEO/LEO+ concepts and the geosynchronous concept arise from the disparity in the satellite orbital altitudes — around 1000 km for the LEO/LEO+ cases vs. 35,800 km for the geosynchronous case. Higher-altitude orbits place more demanding requirements on the radar

instrument: Considerably more power is required, as well as a physically larger radar antenna in order to maintain acceptable range-Doppler ambiguity performance. At the same time, higher orbits also provide more comprehensive Earth coverage as well. Although a sensor's area coverage rate for fixed resolution is limited by range-Doppler ambiguities and is consequently independent of altitude, a higher-altitude sensor would generally have land areas of interest in view more often, so the effective or "useful" coverage rate would be greater for higher-altitude sensors. A SAR constellation at MEO (between around the LEO and GEO altitudes) might strike a good balance between instrument complexity and Earth coverage.

Under the assumption that the SAR visible-swath width is limited by the ground-incidence angle, the visible-swath width increases with altitude, as depicted in Figure 5.1. Points are marked on these curves at altitudes

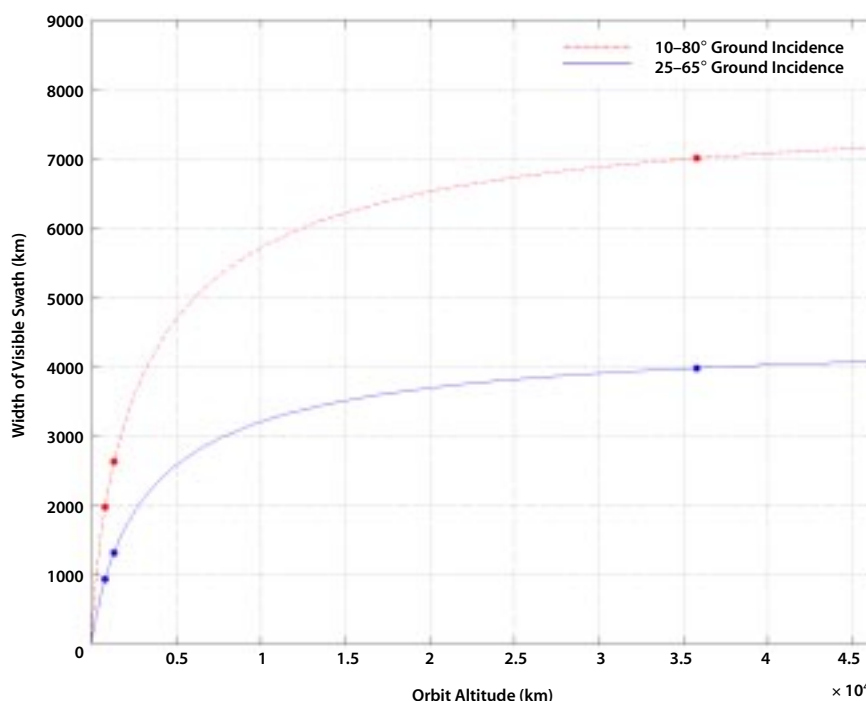


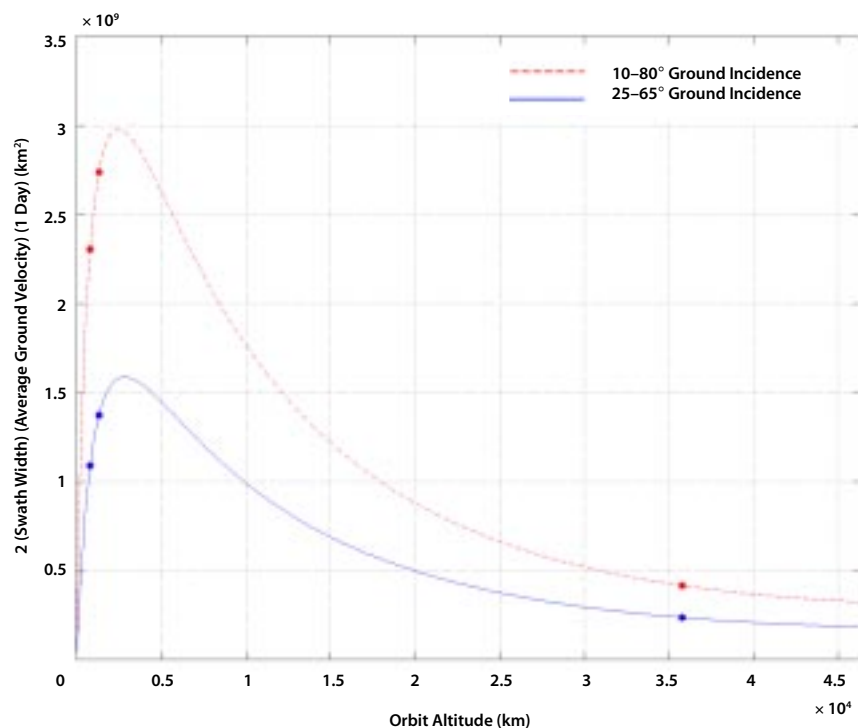
Figure 5.1
Plots of one-sided
SAR swath width for
different ground
incidence angle
limits as a function
of platform altitude.
Markers are for LEO,
LEO+, and GEO
satellites.

corresponding to the LEO (800 km), LEO+ (1325 km), and geosynchronous (35,800 km) concepts. As the altitude increases towards infinity, the visible-swath width approaches an asymptotic limit determined by the curvature of the Earth. An incremental change in orbit altitude thus has a much greater impact on the swath width at lower altitudes than at higher ones.

Considering broadside image acquisitions only, a crude estimate of a SAR platform's two-sided daily coverage area might be computed by multiplying the two-sided visible swath widths of Figure 5.1 by the average nadir velocity of the spacecraft and integrating over one day. Plots of such estimates are shown in Figure 5.2. (Note that ground areas can come into view several times per day, so the coverage area plotted can be larger than the total surface area of the Earth.) Because the nadir velocity decreases with altitude while the swath width increases, these curves

peak at MEO altitudes. Such estimates of the daily coverage area are somewhat oversimplified, however. These estimates do not account for areas accessible through squinted acquisition geometries (see Figure 5.3), and the finite along-track footprint widths of high-altitude sensors can have a dramatic effect on Earth coverage. The estimates also do not account for the ground-track curvature typical of high-altitude orbits, nor do they account for the fact that high-altitude orbits might be more easily designed for better coverage of particular target areas. Furthermore, it may be more difficult to obtain two-sided coverage from lower altitudes since doing so would likely require mechanical rather than electronic antenna beam steering. These factors imply that, in practice, the effective peaks in daily coverage might occur at MEO altitudes somewhat higher than shown in Figure 5.2. More detailed system trade analyses and cost studies

Figure 5.2
Two-sided daily broadside coverage area as a function of platform altitude assuming broadside acquisitions only. The locations of the peaks will be at higher MEO altitudes if other factors are considered. Markers are for LEO, LEO+, and GEO satellites.



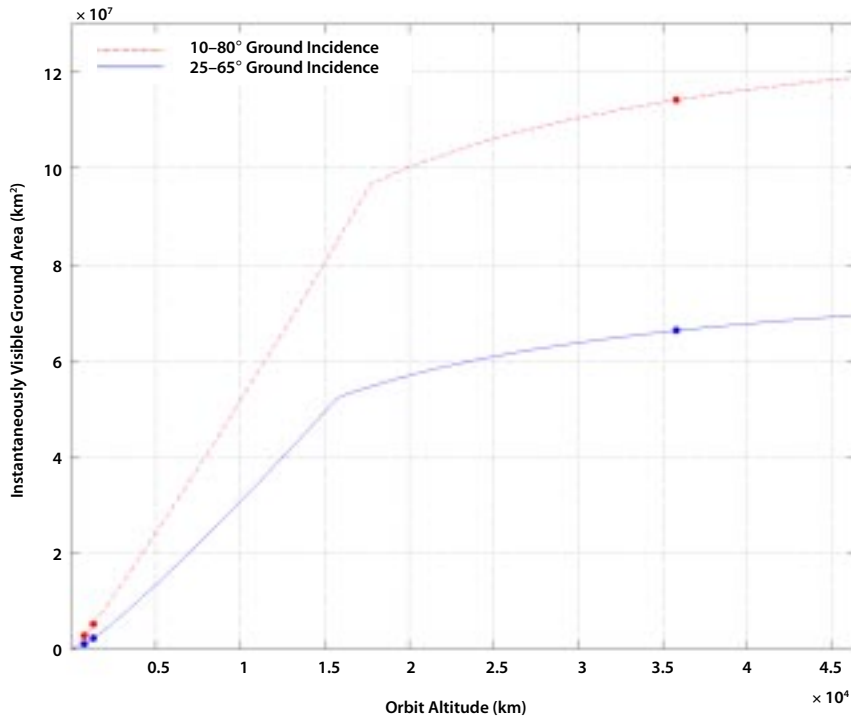


Figure 5.3
Two-sided
instantaneous
accessibility. Area of
the sensor two-sided
visible footprint as a
function of platform
altitude. Markers are
for LEO, LEO+, and
GEO satellites.

would be required to determine the optimal satellite altitude given the factors described above.

Figure 5.3 is perhaps more telling of the Earth-coverage advantages of high-altitude sensors. This plot shows the two-sided instantaneously accessible area, or in other words, the area of the two-sided sensor visible footprint. For low to moderate orbital altitudes (i.e., before the break point at about 18,000 km altitude), the along-track width of the sensor footprint is limited by the maximum azimuth angle to which the radar antenna beam can be steered electronically. At higher altitudes, the along-track footprint width is limited by the squint angle on the ground. The curves shown assume up to $\pm 15^\circ$ of azimuth beam steering and up to $\pm 60^\circ$ of ground squint. For the case of the lower curve, the footprint of the geosynchronous sensor is approximately 30 times larger

than that of the LEO+ sensor. On the other hand, a MEO sensor at half the altitude of the geosynchronous sensor (17,900 km) would have a footprint area 83% of the size of its geosynchronous counterpart.

Clearly, the goal of around-the-clock accessibility for quick-response imaging favors the use of higher-altitude sensors. As the satellite relative velocity decreases with altitude, however, the integration time required to form an image may become significant compared to the event-response time. The average integration time required for 10-m resolution is shown in Figure 5.4. For the geosynchronous case, the integration time could be up to several minutes. This factor would need to be accounted for in more detailed trade studies.

High-altitude SAR systems could provide extensive Earth coverage, but their associated demands on the radar hardware cannot be neglected. Figure 5.5 illustrates the relationship

Figure 5.4
Synthetic aperture integration time required for 10-m resolution as a function of platform altitude.

The required integration time can be several minutes or more at high altitudes.

Markers are for LEO, LEO+, and GEO satellites.

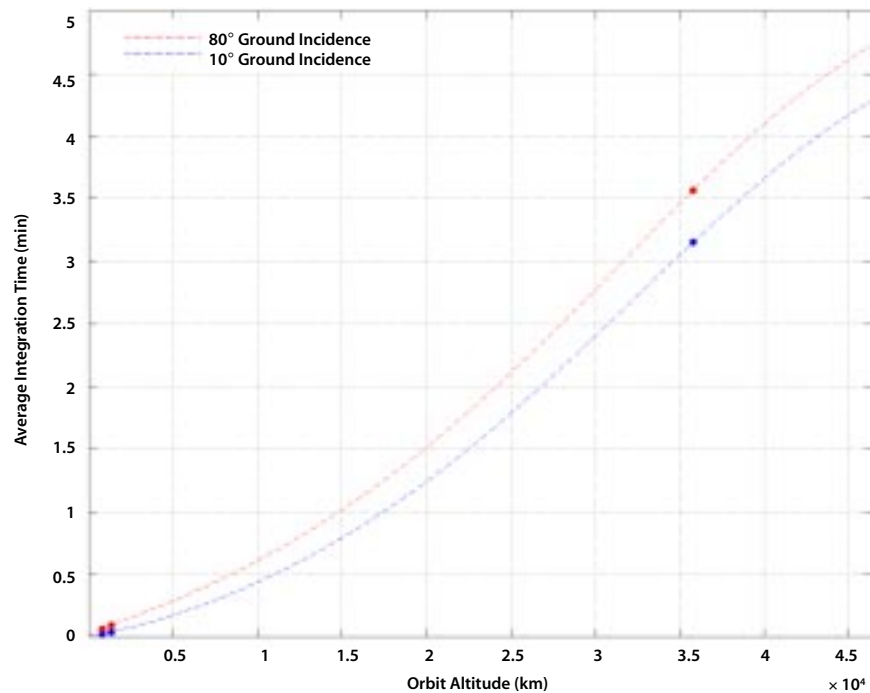
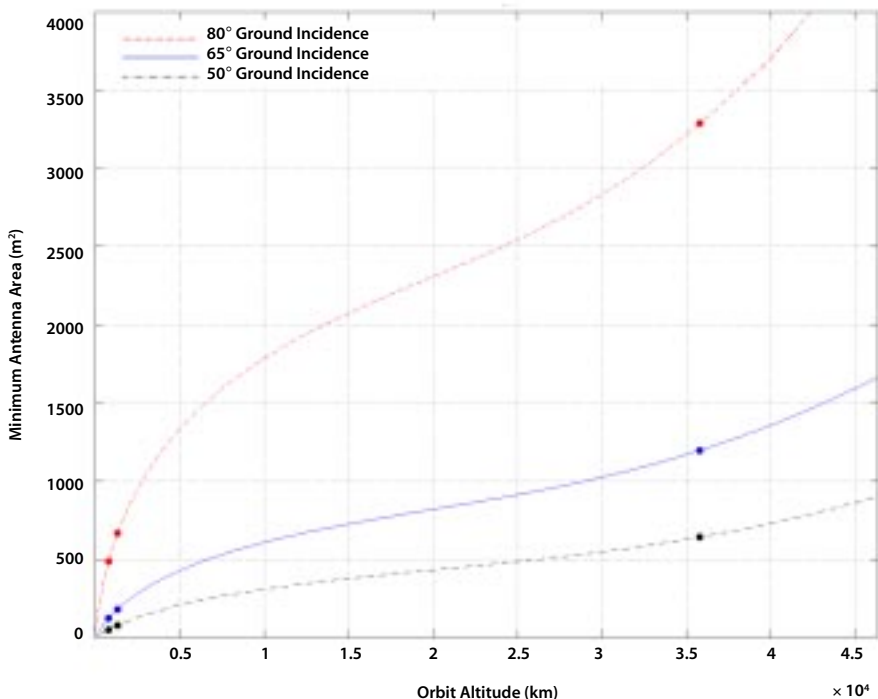


Figure 5.5
Ideal minimum antenna area as a function of platform altitude for various maximum ground incidence angles.

Higher platform altitudes require larger antenna apertures. Markers are for LEO, LEO+, and GEO satellites.



between the orbital altitude and the required ideal antenna area for a number of different ground incidence angles. The required antenna area is driven by the need to avoid range-Doppler ambiguities and increases with both altitude and ground incidence angle. Higher altitudes place less-severe requirements on the electronic-steering capabilities of the radar antenna, however. Figure 5.6 depicts, as functions of altitude, the far-range look angles corresponding to two different far-range ground incidence angles. For nadir-pointed antennas, the far-range look angle is equal to the maximum elevation steering angle. From the curves shown, it is evident that electronic beam steering from side to side would be quite challenging at lower altitudes.

Although the parametric analyses presented in this section are somewhat simplified, they strongly suggest that MEO architectures deserve further consideration. A constellation of SAR sensors in MEO orbits could likely

provide performance similar to that expected from a geosynchronous constellation while doing so with smaller antennas, reduced power, and lower launch costs. Space radiation at MEO altitudes is known to be rather severe, but because the specific characteristics of the radiation environment (e.g., particle energies) must also be considered in the context of the eventual system design, MEO orbits might still be ideal for future SAR missions.

Atmospheric Analysis and Mitigation

Another method for improving measurements from a GESS is to mitigate atmospheric noise effects. Because InSAR observations of surface displacement are obtained through the measurement of signal time delays, variability in the signal propagation properties of the atmosphere can seriously degrade the accuracy of the InSAR technique. If not accounted for, minute changes in the atmosphere's index of refraction can lead to data artifacts that are

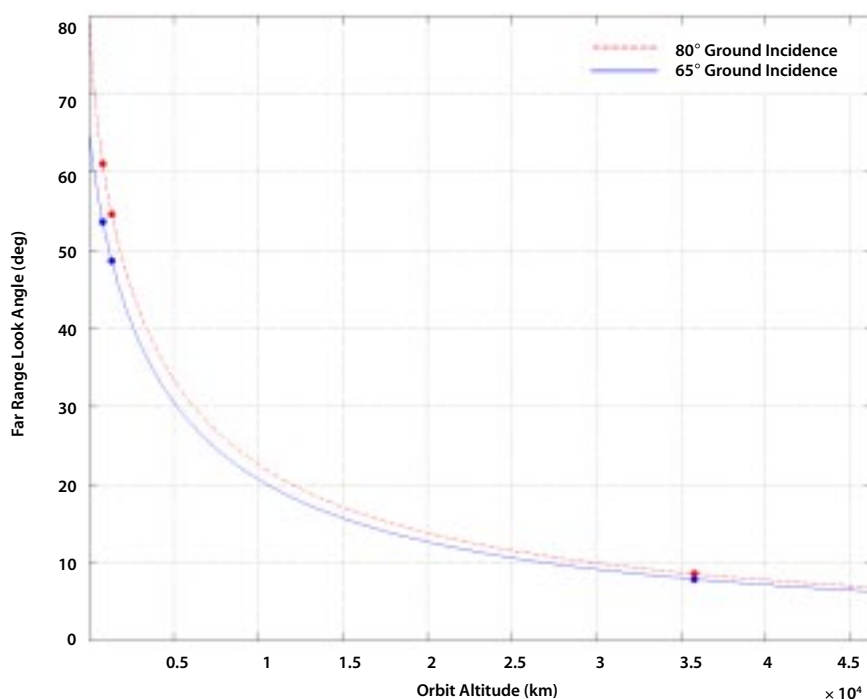


Figure 5.6
Far-range look angle as a function of platform altitude. Because of the greater variation in look angle, side-to-side electronic beam steering is more difficult from lower altitudes. Markers are for LEO, LEO+, and GEO satellites.

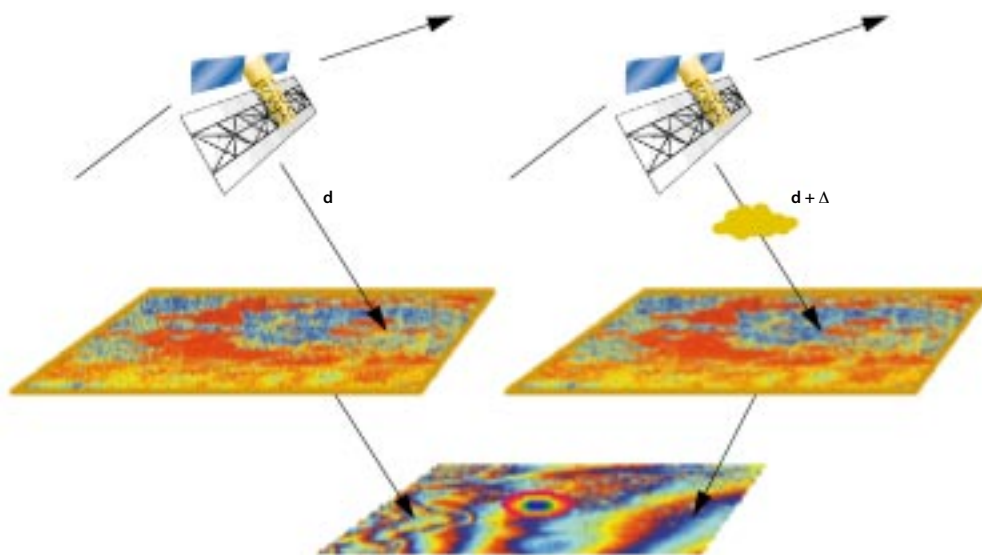
difficult to distinguish from true surface motion; hence, an important aspect of the GESS study has been the characterization of propagation effects introduced by the troposphere and the ionosphere. Effective signal path delays arise in both of these layers, but the mechanisms by which they occur differ. Different mitigation strategies are consequently implied. On the whole, the mitigation strategies for each are common to the LEO, LEO+, and geosynchronous cases, however.

The ionosphere is a dispersive medium and produces several frequency-dependent effects on a radar signal affecting both the resulting single-channel SAR imagery and two-channel interferometric imagery (Figure 5.7). The group delay slows down the radar pulse relative to free space, while the phase delay advances the phase relative to that of free space. The Faraday rotation alters the polarization of the return signal, although this effect is small at the planned GESS frequencies. One may take advantage of the frequency dependence

of the group and phase delays to determine the magnitude of the ionospheric total electron content (TEC) and changes in the TEC over time.

Global and large-scale ionospheric fluctuations are associated with solar UV excitation, and are modulated diurnally and seasonally. These can cause propagation delays at L-band of typically 10 to 40 m, but up to 100 m and more in rare instances. Intermediate-scale disturbances (tens to hundreds of kilometers in extent) include traveling ionospheric disturbances (TIDs) and gravity waves induced by a variety of phenomena. These can alter the propagation delay by up to 5–10%. Small-scale disturbances (ionospheric “blobs” less than approximately 10 km in size) may result in scintillation or SAR defocusing, but tend to be small in magnitude. Larger magnitude small-scale structure does exist near the poles and at times along the equator, however. Total day-to-day variability can exceed a few meters of delay, or up to 25% of the total delay. To

Figure 5.7
Atmospheric signal path delays that change over time create undesired artifacts in differential interferometric imagery.



observe range changes at the centimeter level, the ionospheric effects must be removed almost completely.

We have examined two dual-frequency, or split-spectrum, scenarios. In the first, we assume that GESS transmits a chirp waveform at two L-band (~1250 MHz) frequencies, each 10 MHz wide, separated by 70 MHz. In the second, we envision an additional C-band antenna transmitting a 10 MHz-wide chirp centered at 5350 MHz. We have applied concepts to interferometric SAR similar to those developed for removing ionospheric effects from GPS signals using the GPS dual frequency range and phase observables. Although there are significant differences between GPS and SAR, much work appears applicable. These dual-frequency approaches appear to be capable of removing the ionosphere at the level that GESS requires, at least for intermediate- and larger-scale ionospheric features (10 km and up).

Splitting the spectrum for a single epoch, a single pass of SAR data permits an estimate of the total ionospheric range delay measurement. The apparent range difference of identical features in the split-spectrum images is

$$\Delta r = \alpha T \left[\frac{1}{f_2^2} - \frac{1}{f_1^2} \right]$$

where the range offset is proportional to T , the line-of-site TEC of the ionosphere, and to the difference of the squared inverses of the two frequencies (Figure 5.8). The larger the frequency difference, the larger the effect, although for very different frequencies, the ground imagery changes significantly in other ways. By averaging the observed range offset over areas about 20 km across (depending on terrain and ground features), the total ionospheric delay may be determined to as

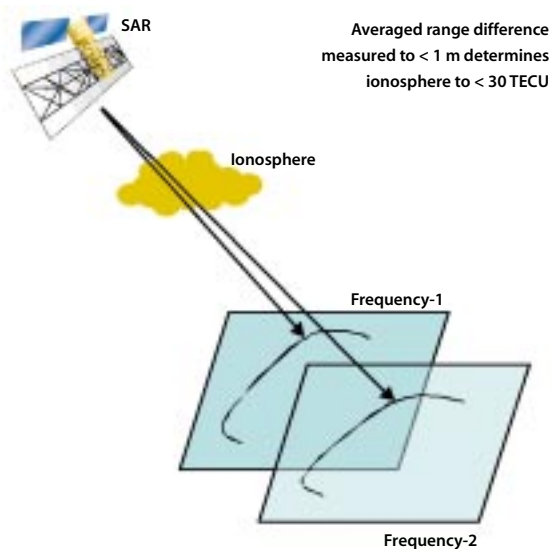


Figure 5.8
Due to the ionosphere, the range of objects in the image changes with frequency.

little as 0.5 TEC units (TECU), equivalent to about 10 cm of ground displacement for differential interferometry.

Splitting the spectrum for two-epoch differential interferometry yields a higher precision estimate of the change in the ionosphere between the two epochs, but no information about the total ionospheric delay. The change in scaled phase due to ionospheric effects is

$$\Delta\phi = \alpha \Delta T \left[\frac{1}{f_2^2} - \frac{1}{f_1^2} \right]$$

where the phase difference is proportional to the change in state of the ionosphere, ΔT . By averaging the interferometric range difference over large enough areas (~10 km on a side), the change in the ionosphere at the required level (0.05 TEC units is approximately 1 cm) may be determined. Thus, intermediate-sized ionospheric perturbations can be estimated and removed from the interferometric data (Figure 5.9). Large-amplitude, smaller-scale perturbations may prove extremely difficult to remove, however.

Unlike the ionosphere, the troposphere is not dispersive, so path delays introduced by the troposphere cannot be removed through split-spectrum techniques. Rather, refractive-index variations in the troposphere stem from inhomogeneities in the air within the lowest several kilometers of the atmosphere. The associated signal-path delays are sometimes associated with meteorological phenomena such as storm systems, but can also sometimes occur in what otherwise appears to be clear air.

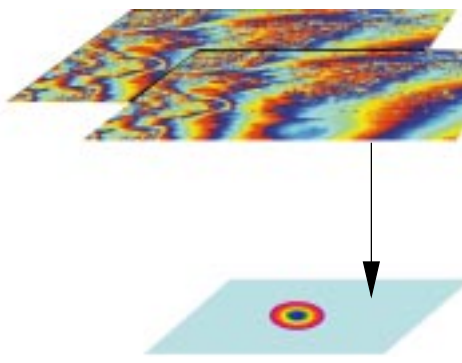
The total signal path delay introduced by the troposphere is often decomposed into dry and wet components, where the former arises from variations in temperature and pressure, and the latter arises from variations in water vapor content. Although most of the total delay is associated with the dry term, spatial variations in the dry delay are relatively slow compared to the size of an interferogram. Artifacts from the dry delay can therefore be removed from an interferogram using only a sparse set of calibration points. Calibration data might come from meteorological data or

from locations where the true surface displacement is known, and such data could provide path-delay accuracies to the level of 1 mm or better.

The wet component of the tropospheric delay poses a much greater problem for InSAR measurements. Because the wet term is rapidly varying spatially, it is much more difficult to remove via external calibration. Spatial variations in tropospheric water vapor content are caused by the turbulent mixing of the air, and because turbulence is a random process, the variability of the wet path delay is usually characterized by statistical models. The Kolmogorov model for such processes suggests that the local spatial variability of the wet delay follows power-law behavior. In other words, the expected rms difference in path delay over two points on the Earth's surface is proportional to the distance between the points, raised to some power. Equivalently, the power spectral density of the wet delay falls off linearly when plotted on a log-log scale. The overall scale factor of the variability changes by orders of magnitude depending on time and global location, however. The wet delay is also highly variable in time, so the wet-delay artifacts between the two SAR acquisitions forming an interferogram are effectively uncorrelated.

Assuming that calibration data are obtained on some regular grid over the surface under observation, the slow spatial variations in the wet delay can be removed from the interferometric data. The wet-delay residual, composed only of the quickly varying components, causes phase artifacts in the interferogram, however. The severity of these artifacts is related to the sample spacing between calibration points through the power-law model of

Figure 5.9
Split-spectrum
interferograms
combined to estimate
ionosphere change.



Averaged interferometric phase
difference measured to < 1 cm
determines ionosphere to < 0.4 TECU

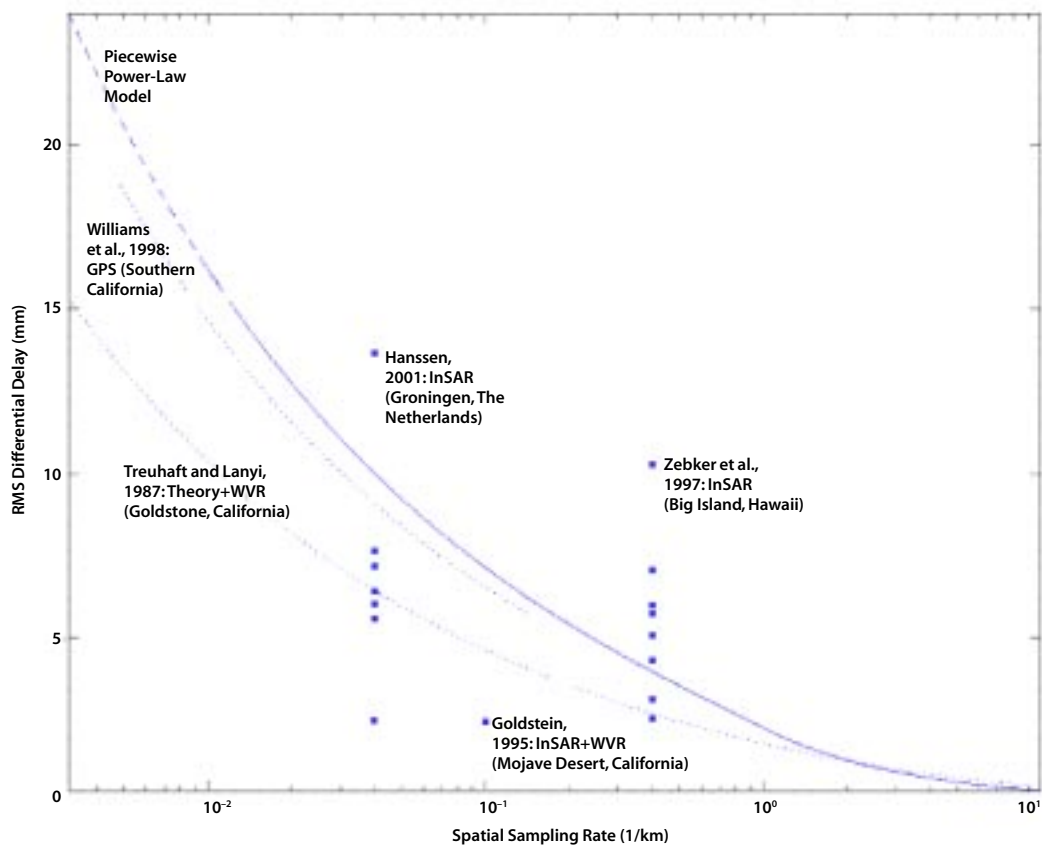


Figure 5.10
Residual one-way differential tropospheric zenith display comparing theoretical models and several data sets as calibration. The modeled residual wet tropospheric delay decreases with increased sampling rate.

the turbulence process, with artifacts becoming less severe as the grid of calibration points is made finer. Calibration data might comprise water-vapor estimates obtained from GPS or water vapor radiometer (WVR) instruments on the ground as well as downward-looking instruments on board the spacecraft. If calibration data are acquired every 10 to 100 km, the residual wet delay can be reduced to the level of 1 cm (see Figure 5.10). Calibration grids much finer than this may be impractical. Mesoscale atmospheric data assimilation models may provide data at fine resolution to correct the delay.

The residual variability in the wet delay can be further reduced through the averaging or “stacking” of multiple interferometric data

sets (Sandwell and Fialko, 2002; Webb et al., 2002). Stacking reduces artifacts and noise from other sources as well, though data limitations and the desire to preserve temporal resolution imply that artifacts cannot be eliminated entirely. Advances in data-processing techniques may also offer ways of removing some tropospheric artifacts. Nevertheless, relative to other sources of error, the wet component of the tropospheric delay may prove to be a limiting factor in the accuracy of the interferometric technique if the goal is to observe millimeter-scale surface displacements. More research on this topic is required to support subcentimeter-scale displacement accuracies.

Technology Studies

C H A P T E R S I X

GESS has studied SAR constellations from low-earth to geosynchronous orbits. These SAR missions place a significant demand on the spacecraft resources (mass, power, data rate). Revolutionary antenna technologies are required to enable the GEO and MEO systems described. High-efficiency integrated (single-chip) T/R modules are necessary to ensure the mass, power, and cost of the modules are not prohibitively high when thousands of modules are required. Adaptive scanning and phase self-compensation techniques will be necessary to alleviate requirements on antenna flatness. Modular or distributed architectures will enable these systems to be very flexible. Radiation-tolerant electronics are also a major challenge, particularly for the antenna electronics, which have only limited shielding.

For the GESS study, three technology studies were completed to address the need for large deployable electronically steered antennas and for a general reduction of radar instrument mass and power. By ultimately reducing the instrument cost, SAR constellations could be enabled. The three tasks were:

- Low-Power Chirp Generator: Demonstrate a miniaturized, low-power, rad-hard chirp generator, which is modular and flexible such that the design is directly applicable to GESS as well as other high-performance radar missions.
- High-Efficiency Transmitter Module: Demonstrate an ultrahigh-efficiency L-band Class-E/F amplifier for use in phased-array transmit/receive modules.
- Geosynchronous SAR Antenna: Conduct design and technology trades to establish the geosynchronous SAR antenna architecture to assess overall mission feasibility and identify the technology roadmap.

Low-Power Chirp Generator

The goal of this activity was to reduce the power consumption of the chirp generator by a factor of five from similar SIR-C/SRTM hardware. In this task, we have demonstrated a low-power, high-bandwidth, reconfigurable digital chirp generator (DCG) for use as a basic building block scalable to a variety of system applications.

Many NASA radar systems operate at L-band or include an L-band intermediate frequency as part of a higher-frequency system. Linear FM chirp waveforms are used for pulse compression. For signal repeatability and flexibility, DCG technology was chosen. The DCG must be frequency agile with the ability to switch between frequencies in a few nanoseconds. The DCG should produce spectrally pure signals (high spurious free dynamic range) and capable of 80-MHz chirp bandwidth.

Minimizing the DC power consumption was a major design goal. When distributed signal generation is required, such as in radar systems implementing an active array antenna requiring hundreds or even thousands of individual DCGs, then power considerations are paramount.

A final major design goal was to ensure that the DCG would endure the space environment. A combination of radiation testing and consultations with radiation testing experts was performed to address this issue.

Technical Challenges

Two candidate technologies were evaluated. The first was based on gallium arsenide (GaAs) technology (STEL-2375A) and the second was based on silicon CMOS technology (AD9854). The differing fabrication process of these two devices leads directly to

almost all of their respective strengths and weaknesses. High-frequency and high-bandwidth digital synthesizers must run at very high frequencies to satisfy the Nyquist limit. High-frequency digital systems invariably require more power than those of lower operating frequencies do. GaAs can run at speeds considerably higher than CMOS, but also consumes more power. Also, the power requirements for GaAs are practically independent of its operating speed. Therefore, one cannot choose to reduce power simply by reducing the speed. In contrast, CMOS requires less power to operate, and its power consumption is directly related to its operating speed, although it cannot run at the maximum speeds of GaAs. If a particular radar system requires less bandwidth, the AD9854 device may be run at slower speeds. In comparison, the STEL-2375A requires 15 W regardless of clocking speed or output frequency.

The AD9854 is hampered by its lower maximum frequency output of 120 MHz. While 120 MHz easily covers the required 80-MHz bandwidth, the signal must be “mixed up” to L-band through heterodyning. A fundamental problem with upconverting low-frequency signals is the close-in image frequency. Unless a multiple-stage upconversion approach is adopted, the image filter is often difficult to realize. The AD9854 is able to overcome this disadvantage by having In-phase and Quadrature (IQ) outputs. These signals can be fed into an IQ mixer to cancel the undesired side band. One technical challenge is created when using IQ modulation. The IQ outputs must be matched to a quadrature mixer that can handle DC-120-MHz input and L-band output. A survey of available components revealed this to be a non-trivial challenge.

A major challenge for the AD9854 is its radiation susceptibility. While the STEL-2375A is inherently rad-hard, the reliable operation of the AD9854 in a high-radiation environment is of concern. This is because it is a silicon (rather than GaAs) device using a commercial (non-rad-hard) fabrication process.

Enabling Technologies

Two semiconductor technologies were evaluated for use as the core-component of a low-power, rad-hard DCG. The first DCG-core is the ITT Microwave (formerly Stanford Telecom) STEL-2375A, which is a hybrid microcircuit composed of a GaAs numerically controlled oscillator (NCO) and

a CMOS DAC. The NCO performs all of the basic functions of the DCG and the DAC converts the digital signal to an analog waveform. The NCO runs up to 1 GHz, which means it can faithfully produce an analog signal up to 400 MHz. The second DCG-core is the Analog Devices AD9854, which is a 0.35- μ m CMOS device. This device runs up to 300 MHz, which means it can faithfully produce an analog signal up to 120 MHz.

The STEL-2375A uses advanced high-speed digital GaAs technology. This technology is newer than silicon technologies, such as CMOS, but mature enough to have an established record. GaAs is well suited for space-based missions as it is naturally radiation tolerant, and its reliability has tested well. Newer materials, such as silicon germanium (SiGe), may become a more practical alternative as speeds increase. However, the radiation susceptibility of SiGe is currently unknown.

The AD9854 device is not new, but its new 0.35- μ m CMOS fabrication process allows for high speeds and unique capabilities. Recent advances in well-balanced, high-frequency SiGe quadrature mixers have enabled us to take advantage of the quadrature outputs of the AD9854.

Figure 6.1
Digital chirp
generators.



(a) STEL-2375A digital chirp generator.



(b) AD9854 digital chirp generator.

Results

The STEL-2375A and the AD9854 were each prototyped using an FPGA as an interface and controller. The DCG based on the STEL-2375A is shown in Figure 6.1(a) and the DCG based on the AD9854 is shown in Figure 6.1(b). Testing of these devices included DC power consumption over all operating modes, spurious free dynamic range, and features testing (i.e., chirp, CW, standby modes). Radiation testing was also performed on the AD9854.

	SRTM DCG	STEL-2375A DCG	AD9854 DC
DC Power (typical)	25 W	15 W	3 W
Reference Clock (max)	180 MHz	1000 MHz	300 MHz
Bandwidth (max)	72 MHz	400 MHz	120 MHz
SFDR (measured worst case)	-36 dBc	-40 dBc	-52 dBc
Fabrication	GaAs	GaAs and CMOS XFCB process	0.35 μ m CMOS TSMC process

As expected, the power requirement for the GaAs STEL-2375A was constant over all modes (CW or chirp), clocking speeds, and RF power out. Also as expected, the power requirement for the CMOS AD9854 was directly proportional to the clocking speed of the device. The AD9854 device also draws considerably less power when certain programmable modes are disabled such as the “inverse sinc” function. This flexibility can be used to optimize the device for low power, based on the specific performance needs of the system.

Performance results for both devices are listed in Table 6.1, and compared to the performance of the SRTM DCG, which is based on an earlier version of the STEL device.

Consultations with radiation testing experts at JPL indicate that the STEL-2375A, which is a GaAs device in a mil-spec package, is very likely to pass radiation tests without problems; therefore, radiation testing of this component was not performed. The AD9854, however, is a commercial CMOS device in a plastic package and there were concerns as to whether it can be space qualified. Therefore, limited radiation testing of the AD9854 was conducted.

Two tests were performed on the AD9854. The first was a total-dose-until-failure or Total Ionizing Dose (TID) test that was used to estimate of the component’s on-orbit lifetime. The device was then subjected to heavy ions during operation. From this test, the rate and effect of single-event upsets (SEUs) on the device was estimated. Also, the device’s susceptibility to latch-up was estimated.

Results indicate this component is a candidate for flight integration at moderate to high risk, which is a lower risk level than that of components currently in some flight programs. The major risk factor for this device is damage to the device due to latch-up events; however, this may be mitigated through the addition of latch-up detection circuitry. The SEU rate is insignificant relative to the refresh rate of the device (>1000 times per second), and poses little risk. The part was tested to a TID of 200 krad without failure, but showed signs of degradation (high current draw) at 50 krad. The results of these tests are summarized in Table 6.2.

Summary and Conclusions

Two candidate technologies were evaluated for use in a general-purpose digital chirp generator. Desired features include low power

Table 6.1
Comparison
of devices.

Table 6.2
Tests performed
on AD9854 DCG.

TEST	METHOD	RESULT
On-orbit lifetime	Total Ionizing Dose (TID)	50 krad
Single-event upset (SEU)	Heavy ions	6 per day (max)
Latch-up	Heavy ions	1 per 5 years (est.)

consumption, high speed, high dynamic range and high radiation tolerance. Flexibility of the waveform characteristics and performance is also very desirable, so that the device can be programmed for optimal performance with minimal power consumption. The AD9854 NCO-based digital chirp generator has all of these features. It significantly reduces power consumption. The SFDR performance is also superior to that of the STEL-2375A. Although the AD9854 is hampered by its lower speed, if the quadrature upconversion scheme can be shown to be reliable, then the AD9854's speed disadvantage can be overcome. The last obstacle for using the AD9854 in flight is its ability to operate reliably in a radiation environment. The limited radiation testing performed has determined that the AD9854 may be a viable option for some space applications.

If necessary, the AD9854 chip can be obtained in die-form and then repackaged for better radiation tolerance. For advanced systems, a custom application-specific integrated circuit (ASIC) device with similar performance could be developed using more advanced materials, such as silicon germanium (SiGe). This would also lead to significant reductions in the size of the device and could enable its use in a distributed antenna architecture, where the signal generators are distributed within the array.

High-Efficiency Transmitter Module

Future SAR missions, such as the concepts currently being studied at LEO, LEO+, and geosynchronous orbits, require very powerful radar systems. This task addressed the need for higher-efficiency transmitters for use in these advanced radar applications. Significant improvements in the transmit/receive (T/R) module efficiency will make very large, high-power, electronically scanned SAR antennas more feasible and affordable.

Existing and recently proposed L-band SAR systems (RADARSAT-2, SIR-C, SRTM, LightSAR, ECHO) all rely on conventional Class-AB or Class-C power amplifier technologies to achieve moderate L-band efficiencies of 30–40%. By using the new Class-E/F power amplifier circuit topology, efficiencies on the order of 70–90% can be achieved. Using current solid-state power amplifier (SSPA) technology, 60 kW of radiated RF power (at 20% duty cycle) will require roughly 30 kW of DC power for the transmitter alone. By improving this efficiency to 80%, the DC power requirement is reduced to 15 kW, thus requiring a much less capable spacecraft and dramatically reducing the mission costs. By miniaturizing the high-efficiency T/R modules, they can be used for both conventional rigid panel phased-array antennas (LEO, LEO+ SAR missions) as well as in super-lightweight, flexible membrane antennas (geosynchronous SAR).

Significant improvements in efficiency will also simplify the thermal design and increase reliability, particularly for membrane antennas, where heat dissipation is far more challenging.

The objective of this study was to demonstrate the feasibility of using a Class-E/F power amplifier at L-band frequencies. The design goals were to achieve 30 watts at L-band (1.25 GHz) with greater than 80 MHz bandwidth and 70% efficiency.

Technical Challenges

We have studied the use of switch-mode amplifier circuits for use as high-efficiency RF power amplifiers. Switching amplifiers, such as Class-E and Class-E/F amplifiers, use the active devices as switches. That is, the active device is ideally fully-on (short-circuit) or fully-off (open-circuit). These circuits are commonly found in switching power supplies, but only recently have they been exploited as RF amplifiers due to the availability of transistors with substantial gain and power at microwave frequencies. The theoretical efficiency for Class-E and Class-E/F amplifiers is 100%; practical efficiencies of 70–90% have been demonstrated at UHF frequencies.

To achieve ultrahigh efficiency, there are four primary loss mechanisms to overcome: conduction loss, input power loss, discharge loss, and passive component loss. The first three loss mechanisms are due to the active devices. Active device losses for switch-mode amplifiers occur mainly during transitions from one switch state to another. By using a high-Q resonant output network, Class-E and Class-E/F amplifiers minimize this switching loss. At L-band, the active devices are typically large in size, have large on-resistance, large output capacitance, and very low

input impedance — all contributing to the loss. The last loss mechanism is due to the passive matching networks. Due to the topology of the push-pull amplifier, a microstrip balun (balanced-to-unbalanced transformer) circuit was needed to convert from a single-ended to double-ended signal at the input and output. This balun must be very low loss and also must be small and planar with a flexible geometry for easy integration into the amplifier circuit. Proper modeling of parasitic capacitance and inductance was another important challenge to ensure the circuit can be properly designed and reproduced to the given requirements.

Enabling Technologies

The California Institute of Technology (Kee et al., 2001) has developed a new class of power amplifier, the Push-Pull Class-E/F power amplifier. The Class-E/F amplifier, which is similar in operation to the more common Class-E amplifier, promises to further increase efficiency and reduce circuit complexity while extending the maximum operating frequency and bandwidth to L-band and beyond.

Push-Pull Class-E/F amplifiers have the following advantages over other switching amplifiers:

- They combine two transistors so higher power levels can be achieved.
- They incorporate the transistor output capacitance into the tuning circuit. Since most high-power devices have high-output capacitance, this feature improves the performance of the tuning circuit.
- They have a lower peak voltage, reducing the transistor breakdown voltage requirement.
- They have lower RMS current, which reduces resistive loss of the circuit.

- They have soft-switching, which keeps the current at a low level while the capacitors discharge, reducing the discharging loss of the amplifier.

The extension of the Class-E/F circuit topology to higher frequencies and high output powers (over 20 W) requires careful selection of the power transistor device. LD-MOS, SiC, and GaN are all viable technologies. For this demonstration, LDMOS (specifically, the Motorola MRF284) has been selected because of its low cost and availability. The advantages of LDMOS include high breakdown voltage and high operation frequency. GaAs is also a mature and widely available device technology. Wide-bandgap materials, such as SiC and GaN, also show promise for high-frequency and high-power applications. However, since these technologies are not as mature as LDMOS and GaAs, the availability of commercial products is a practical problem.

Results

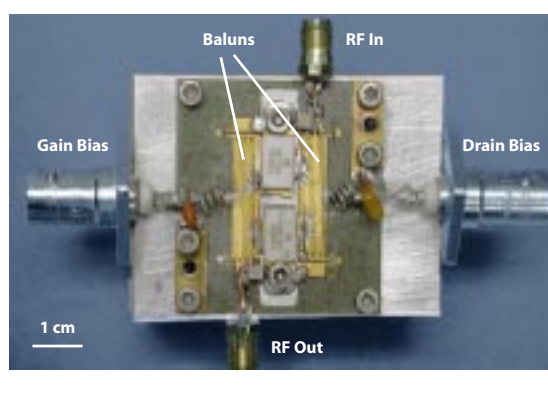
An L-band Class-E/F power amplifier (PA) has been built and measured (Figure 6.2). Preliminary results show an efficiency of 64%

at 800 MHz and an output power of 30 W. The operating frequency is less than the target 1250 MHz, which may be due to parasitic capacitance and inductance in the circuit. Future work includes more thorough testing of the amplifier. In addition, improvements to the circuit models are required to adjust the operating frequency. Since the active devices are the most critical components of the amplifier, evaluation of different device technologies (LD-MOS, GaAs, SiC, GaN) should also be addressed in future studies.

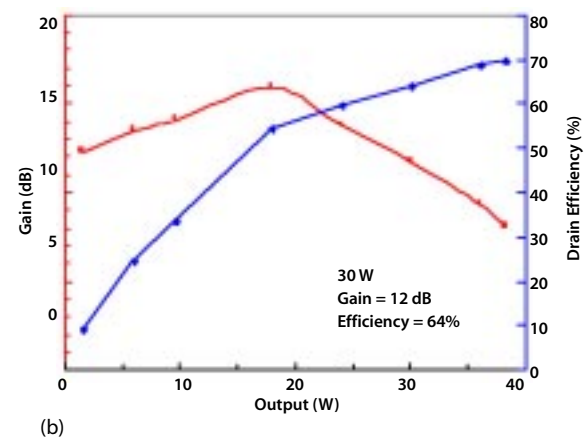
Summary and Conclusions

In this task, JPL teamed with Caltech to explore the use of the new Class-E/F amplifier as an L-band transmit module to achieve high efficiency. Although the performance goals were not entirely achieved, this proof-of-concept breadboard has demonstrated the feasibility of using Class-E/F amplifiers at L-band. This research will continue through an Earth Science Technology Office (ESTO)-sponsored technology research task under the Advanced Component Technology (ACT) program. Future research will include improv-

Figure 6.2
 (a) Photo of the L-band Class-E/F PA.
 (b) Output power, efficiency, and gain of PA at 800 MHz.



(a)



(b)

ing the circuit models to better predict the performance and then demonstrating improved performance at L-band. Ultimately, through the ACT program, the Class-E/F PA will be incorporated into a complete high-efficiency L-band T/R module.

Geosynchronous SAR Antenna Study

Future advanced SAR concepts, such as the one being studied by GESS for a geosynchronous SAR mission, require very large antenna apertures with full 2-D beam-steering capability. This class of antennas requires apertures on the order of several hundreds of square meters transmitting 60 kW of RF power. For this class of mission to be feasible and affordable, the antenna mass and stowed volume must be low enough to fit into an existing launch vehicle. Antenna mass densities must be reduced by an order of magnitude (20 kg/m^2 to less than 2 kg/m^2).

Several notional concepts were developed for a geosynchronous SAR mission and two were studied in some detail. The first concept is to deploy this system using autonomous, reconfigurable panels. Here we envision using an array of hexagonal panels that can be assembled in space to form arrays of differing geometries. Therefore, the same basic antenna element can be manufactured in large volumes on the ground and then assembled in space in the desired configuration. These autonomous antenna panels would be completely self-contained each with its own spacecraft avionics and solar arrays. A detailed study of this concept was conducted for the National Reconnaissance Office (NRO) under the Director's Innovation Initiative (DII) program. The second concept under consideration for the geosynchronous SAR system is a large deployable hexagonal antenna with centralized (rather

than distributed) spacecraft bus components, as described in Chapter 4. The advantage of this concept is that a single launch vehicle can deploy the entire array. The autonomous panel concept would require multiple launches to deploy an antenna of the size required for GESS.

A design study was completed of the geosynchronous SAR antenna based on the large deployable antenna concept to identify key technology drivers for such a system. First, several antenna architectures were evaluated. Once the antenna architecture was selected, a study of the signal generation, distribution, and transmit/receive architecture was conducted to optimize for low mass, low power, and maximum performance. Antenna structures and deployment were also studied. Based on these design and technology trades, the antenna mass, power, and cost were estimated. The design was then used in a Team X exercise to assess overall mission feasibility. This section summarizes the results of the antenna design study.

Antenna Requirements and Performance

The geosynchronous SAR mission design concept was presented in Chapter 4. The driving requirements of the radar antenna are presented in Table 6.3. For a large 30-m aperture antenna and 2-D beam scanning capability, mass, cost, and complexity are major factors to be considered in selecting the antenna architecture. Because the required amount of beam scan is 8° and possibly greater for other future systems, only array concepts are considered for wide-angle beam scanning needs.

Three array concepts were considered for performance trade-off: distributed phased array, reflectarray, and array lens. The distrib-

Table 6.3
Geosynchronous
SAR antenna
requirements.

PARAMETER	REQUIREMENT
Frequency	1.25 GHz
Bandwidth	80 MHz (6.5%)
Aperture Size	30 m × 30 m
RF transmit power	60 kW
Duty cycle (PW*PRF)	20%
Beam scan	±8° or more
Polarization	Single linear vertical
Sidelobe level	-30 dB
Cross-pol level	-25 dB

uted phased array approach has graceful degradation in performance with very little risk of a single-point failure. Also, by using mostly corporate-feed power division, the array is able to achieve adequate RF bandwidth where more than 10% bandwidth can be achieved. The reflectarray and lens arrays do not require complicated beamformers (power dividers) but have limited bandwidth and require a high power TWTA. Using distributed T/R modules would be the more feasible and reliable approach to achieving the very high transmit power. The simplicity of the reflect-array and array lens approaches cannot overcome the bandwidth advantage of the distributed phased array. Because the 6.5% bandwidth is an essential requirement of the radar system, the more complex distributed phased-array approach is selected.

One of the most constrained aspects of the array architecture is the element location. The element locations will determine the overall sidelobe and grating lobes of the antenna. From the standpoint of complexity, it is

desirable to minimize the number of elements. However, insufficient element density causes the appearance of grating lobes and reduced gain when the beam is scanned. In order to minimize the element density while maintaining the required suppression of grating lobes, a triangular grid is used. By arranging the elements on the nodes of a triangular grid, slightly greater (as compared to rectangular grid) element spacing can be used. The maximum spacing that will meet the grating lobe requirements is 0.9λ , which is 21.4 cm at the center frequency. Suppression of grating lobes also requires that each element has its own phase shifter. A 4-bit phase shifter quantization should suffice to achieve the required beam pointing resolution and sidelobe level. To reduce the impact of phase shifter losses on system performance, each element is also fed by its own T/R module, which contains a low-noise amplifier (LNA), a PA, and control circuitry to ensure signal gain on the antenna element side of the phase shifter. An alternative architecture includes a T/R module (PA and LNA) at each subarray and only a phase shifter at every element. This architecture requires low-loss phase shifters. The “fully-populated” architecture delivers better performance but at a higher mass and cost. For this study, we have selected the fully-populated architecture with one T/R module per element.

In order for the 30-m antenna aperture to be stowed and fit into a several-meter launch vehicle fairing, the antenna's membrane aperture must be separated into several sections of rollable and foldable structures. Because of the separation of structures and folding of membranes, gaps where there are no radiating elements (up to 10 cm wide) will be formed between membranes. In addition, because of the particular deployment mechanism

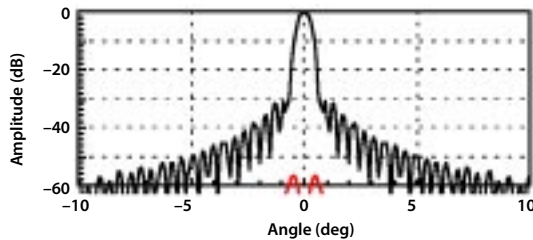
selected, the aperture center will have a 1-m-diameter circular hole where there also are no radiating elements. Far-field radiation patterns and antenna gain losses were calculated to predict the significance of gaps and holes. Figure 6.3(a) gives the 0° scanned pattern from a perfect 30-m aperture without any gap or hole. Figure 6.3(b) shows the pattern effect when gaps and center hole are present. It can be noticed that, besides a 2 dB rise in sidelobe level, there is no significant change in pattern shape. The antenna gain loss is 0.63 dB.

When the main beam is scanned to 8° from the broadside direction, the pattern effects are given in Figure 6.4(a) and (b). Again, no significant change occurred in the pattern. The gain loss is 0.72 dB. One can conclude that the presence of the given membrane gaps and center hole do not produce any detrimental radiation effect.

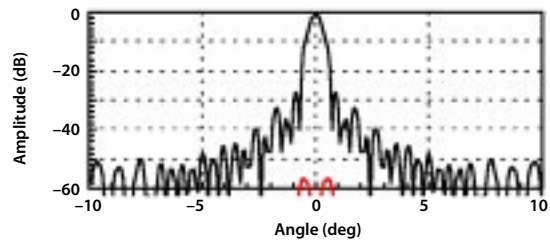
System Architecture

There are many architectural trade-offs, some of which depend upon the future development of technologies. The system architecture presented here incorporates current knowledge and technology predictions in order to satisfy the instrument requirements. However, in cases where the most effective choices are not clear, options are presented along with pros and cons of each approach.

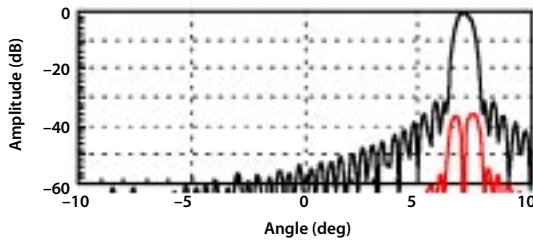
Two key goals of this design are to minimize the overall system mass and to facilitate easy stowage of the antenna. Both of these goals indicate that we should minimize the number of antenna layers. The microstrip patch radiators require two layers (one for the patches and one for the ground plane); thus, the minimum number of layers is two. However, in order to have enough space to implement the required microstrip power dividers,



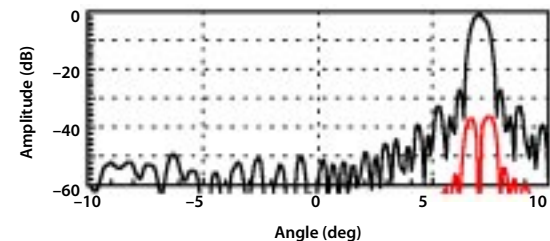
(a) Perfect aperture.



(b) With given gaps and center hole.



(a) Perfect aperture.



(b) With given gaps and center hole.

Figure 6.3
Calculated radiation patterns of a 30-m aperture array with 0° beam scan.

Figure 6.4
Calculated radiation patterns of a 30-m aperture L-band array with 8° beam scan.

a third layer is required. Each layer is constructed of 40- μm -thick polyimide dielectric material, such as Kapton®, with copper metallization. In order to satisfy the skin depth requirements at L-band, the copper must be at least 5 μm thick. However, other requirements such as DC power distribution, heat dissipation, and radiation shielding may require that the metallization be thicker in some places.

There are two reasonable places to put the T/R modules: on the inner ground-plane layer or on the outer layer with the patch radiators. In order to minimize the number of interconnections, it is advantageous to place the T/R modules on the layer with the patches. From a thermal management perspective, it is best to place the T/R modules on the ground plane layer. This allows heat to be spread over the entire ground plane, increasing radiating area. However, each T/R module must then be connected to the patch, which would require over 15,000 interconnections, decreasing reliability and making assembly difficult and costly. A promising approach is to place the T/R module on the inner layer, as above but using a noncontacting method, such as coupled lines or apertures, to feed the T/R modules and the patches. This is superior from a mechanical and reliability perspective but may incur substantial RF losses, thereby degrading power efficiency and system performance. Because of the substantial advantages of this approach, it merits further investigation.

Because of the large size and operating bandwidth of the antenna, true time delays (TTD) are required for proper beam formation. If phase delays alone are used, a reduction in gain and increased grating lobes would

occur. It is impractical to apply a time delay to every element, so instead, the full array is broken up into subarrays of reasonable size and each subarray has a time delay applied to it. Additionally, each element within the subarray contains a controllable phase delay. The full array and subarray design is illustrated in Figure 6.5.

There are a total of 61 TTD subarrays. The size of the time-delayed subarray was chosen to minimize the degradation of antenna gain caused from grating lobes. Separation of the antenna into subarrays also facilitates signal distribution. Each of these TTD subarrays is composed of 36 groups of seven elements (defined as subarrays) arranged in a hexagonal pattern. All 252 elements in the subarray are driven by a single digital transceiver. The digital transceiver receives digital waveform data from a central controller and converts it to an analog waveform with the appropriate time delay and is distributed to the 252 elements with T/R modules and phase shifters. Received power from each element is combined in the microstrip divider/combiner networks so that a single L-band analog received signal reaches the digital transceiver. This signal is then digitized and the resulting data is sent back to a central processor/controller (CPC) for final beamforming. The array system architecture is shown in Figure 6.6, which illustrates the interconnection of the CPC, the TTD subarrays, the T/R modules, and radiating elements.

As previously noted, true time delay is required for proper beam formation. This can be achieved in either analog or digital circuitry. Analog time-delay circuitry consists of switched time delays that are implemented in transmission lines or optical fibers. Because of the line lengths involved, these delays are

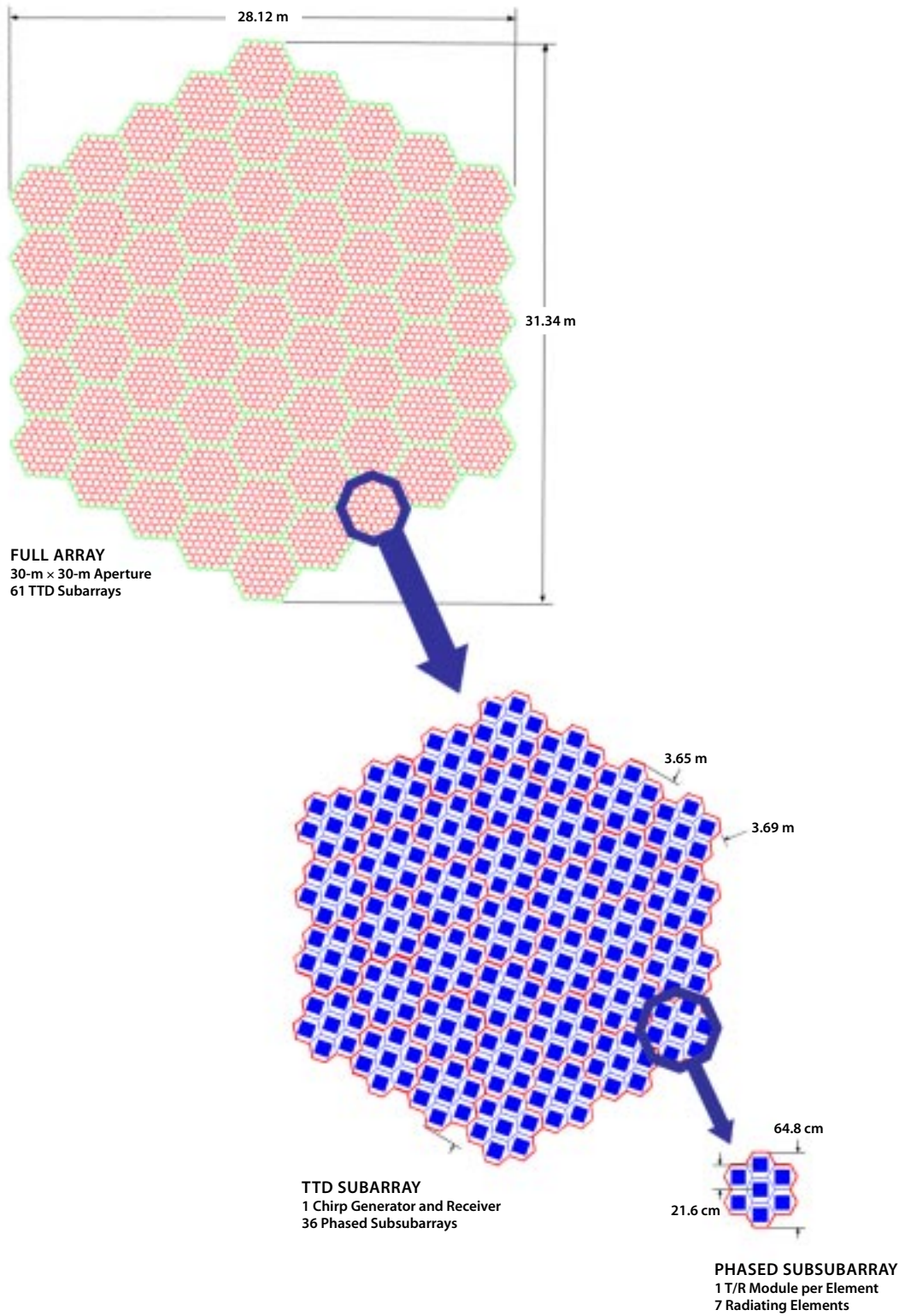
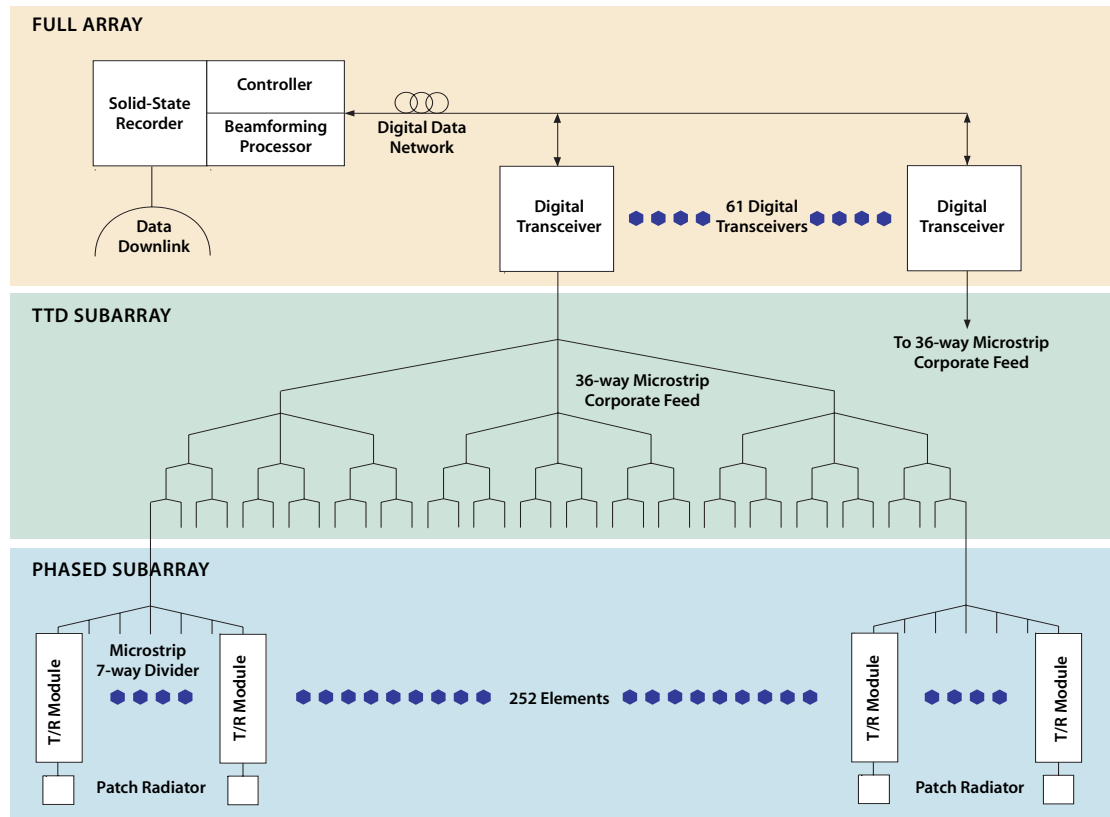


Figure 6.5
Array and subarray
configuration.

Figure 6.6
Array system
architecture.



difficult to miniaturize. Therefore, the approach chosen for this design is to implement the time delays digitally. The major challenge is developing a low cost method of integrating optical fibers with the membrane and reliable connection of fibers to the electronics. Also, because of the high radiation environment, radiation-tolerant fibers must be used.

The architecture of the T/R module is conventional in the sense that it contains a power amplifier, low-noise amplifier, phase shifter, programmable attenuator, and control circuitry. Because of the high average transmit power of the array, it is essential that the power amplifiers be as efficient as possible. Class-E and Class-F amplifiers with over 90% efficiency at 50 MHz have been demonstrated and efficiencies of 70% at L-band are

predicted. This is an area of ongoing research of great interest for both radar and communications applications. A separate activity was undertaken in the GESS study to demonstrate an L-band high-efficiency Class-E/F power amplifier for use in the T/R module, although it wasn't assumed in this system design.

While the architecture of the T/R module is conventional, its packaging is not. In order to successfully mount T/R modules on a thin membrane and maintain the ability to fold and roll it, the modules must have a low mass and a small footprint. Also, reliable and low-cost attachment techniques are required. This requires highly integrated mixed-signal electronics. In order to reduce the mass of the modules, radiation shielding must be minimized. This requires the use of highly radiation-tolerant semiconductor technologies.

Another challenging aspect of such a large and powerful array radar is generating and distributing electrical power. Power is generated by a skirt of flexible solar cells that wrap around the cone and at the edge of the array. Power is then fed inward from the perimeter of the array. In order to minimize ohmic losses in the power distribution systems, 100 V was chosen for the distribution voltage. Voltages greater than 100 V run a substantially increased risk of arcing, while lower voltages will increase ohmic losses. Since the electronics in the T/R module and digital transceivers require lower voltages, voltage conversion is required.

Heavy copper wire attached to the membrane causes unwanted mechanical stresses and additional integration problems. Since achieving low-loss transmission requires a certain conductor cross-sectional area, we can minimize the thickness of conductors by maximizing the surface area that they cover. The ultimate extension of this approach is to feed the power through a thin copper sheet on the interior membrane layer. The sheet can be coated with copper on both sides, with one side being the power plane and the other side the ground plane. One danger of this approach is that a short circuit caused by damage to the membrane may disrupt the power source for the entire array. An approach to mitigate this risk is to divide the power plane into small cells, each connected to its neighbors by fusible links. This concept requires further study.

Structural/Mechanical

A structural system concept for deployment of the large antenna and integrated solar arrays was formulated. This included several trade studies on various deployable and inflat-

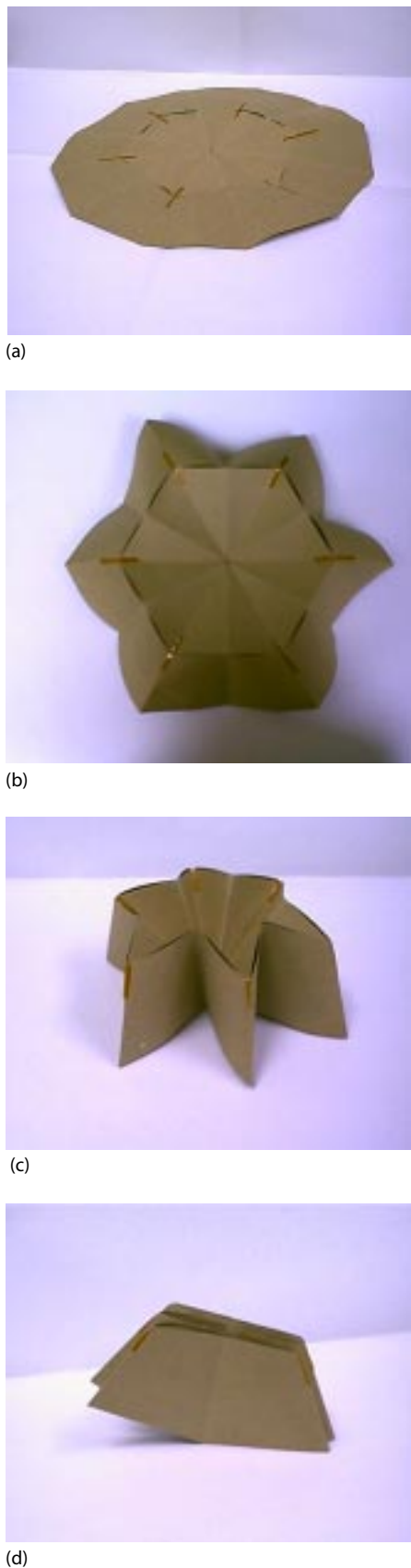
able booms and sizing of the structural members (vertical and horizontal booms). A study of system packaging, membrane management, deployment, and tensioning was conducted. A finite-element model was assembled and used in a preliminary structural analysis. The results of these studies were used to estimate the overall system mass and launch volume. The design was then used in a Team X exercise to assess overall mission feasibility. The results of the overall geosynchronous SAR mission design were presented in Chapter 4.

The horizontal booms deploy, support, and tension the membrane antenna aperture. The self-rigidizable spring-tape-reinforced (STR) inflatable booms of 10-inch diameter were selected for this application for high stiffness and low mass. Other high-stiffness, light-weight booms, including those deployed by mechanical means, are also suitable. The axially deployed booms must be very stiff to maintain aperture flatness. We have baselined the AEC-Able ADAM mast for this application since it has SRTM heritage. Able is currently developing an improved high-stiffness mast that will reduce the linear mass density to 1/8 of the SRTM mast and increase the stowed packaging efficiency by a factor of two while maintaining equivalent strength, stability, and stiffness. This advancement in technology will simplify the packaging of the geosynchronous SAR antenna and increase mass and launch volume margins.

Membrane Aperture Packaging

Membrane management was studied to identify a feasible method of packaging and deploying the antenna. The membrane antenna and the integrated ring-shaped solar array together form a dodecagon. Each of the

Figure 6.7
Antenna folding
procedure.



twelve sides of this dodecagon has a length of 19 meters. To package this dodecagon, it will be first divided by twelve radially extended fold lines and then be packed by a fold-and-roll method. The folding part of this packing method involves the sequential origami folding steps exemplified in Figures 6.7(a) through (d).

The folded stack height can be reduced by increasing the number of rings in the folding pattern while using the same folding approach. A four-ring folding will reduce the stack height to around 5.2 m. Although further reduction of stack height can be achieved by using even more rings, it may present other difficulties in packing the membrane aperture. Also, it is important that the RF design be made compatible with the fold lines as discussed previously. To stow for launch, the folded-up membrane stack will be rolled around the 1-m-diameter central mandrel that is also the canister housing the stowed upper ADAM mast.

Conclusions

While the implementation of a large-aperture, high-power, true time delay (TTD) radar array on flexible membrane presents many architectural challenges, none of the obstacles appear insurmountable. A key focus area for further research is interconnect technology. Lightweight, low-loss, membrane-compatible interconnects for RF, and data and power distribution must be developed. Furthermore, these interconnects must be highly reliable and easily manufactured. Continued research into membrane compatible electronics is also required. The ultimate goal is a low-cost, high-reliability process for producing highly integrated, radiation-hardened, mixed-signal circuits and attaching them reliably to a mem-

brane. This technology is critical for implementation of the GESS radar and would also enable many other large aperture radar concepts. Membrane antenna technology has been demonstrated with several successful ground demonstrations. Future research must address improved element feeding techniques such as slot-coupled to replace bulky feed-probes. This will result in a much less complex and easier to manufacture design that can stow much more compactly. The antenna structures can implement either mature mechanically deployable structures or the emerging technology of inflatable/rigidizable structures. The first few modes of the system are governed mainly by the stiffness of the horizontal booms. Preliminary analysis of the in-space dynamics of the deployed flight system indicates that the fundamental frequency is greater than 0.2 Hz using inflatable boom technology, which is well within the capability of typical spacecraft attitude control systems. The primary challenge is maintaining acceptable antenna flatness, and addressing calibration and metrology techniques to correct for surface deformation in the array.

Technology Roadmap

What are the challenges?

We have described a number of advanced SAR mission concepts. For the near-term missions (LEO and LEO+), there is little technology development required. Evolutionary advances in technology to reduce instrument mass and power will lead to incremental improvements in performance. However, to enable the most ambitious GESS mission concepts, such as the geosynchronous SAR constellation, revolutionary new technologies are essential. The antenna is the dominant component of the radar system and with the

increasing demands for higher resolution, higher sensitivity, targetability, and coverage, the antenna aperture becomes very large, requiring a complicated distributed active array architecture. The array architecture presents many system-level design and integration challenges. Since thousands of T/R modules are required, reducing the mass, power, and cost of these modules will be very beneficial. In addition, signal distribution (RF, control, power) is very complex and low-cost interconnect technologies are required to interface with the modules. Also for the large array, advanced techniques such as digital beamforming and TTD steering may be required. Adaptive methods to compensate for deformation in the array flatness will also need to be addressed. These system issues require a very complicated antenna. For such a large aperture to fit within existing launch vehicles, membrane antenna technology would likely be employed rather than conventional rigid panels. This is a major technical undertaking.

Inflatable membrane antennas have been an area of research over the past several years, with several engineering prototypes developed to demonstrate that inflatable structures can be used to deploy and stretch flat membrane antenna apertures with good RF performance (Huang et al., 1998). Recent focus on inflatable structures has been to develop self-rigidizing technologies and methods to control deployment. Approaches to properly tension the membranes to maintain flatness and precise layer separation is also an area of focus. Although inflatable membrane antennas have been successfully demonstrated, these antennas have not yet addressed the very complicated problem of integrating electronics within the aperture. Nor can the existing

systems be scaled to antennas of the size required for GESS. Mechanically deployed structures are far more mature than inflatables and have the advantage of high stiffness and stability; however, they do not have the high packing efficiency of inflatable structures.

Trade-off studies indicate that as the structure length grows beyond 50 m, inflatable technologies may be advantageous. For GESS, both inflatable and deployable structures are candidates.

Besides the mechanical complications of constructing a large-aperture membrane SAR, the integration of the large number of T/R modules and other electronics within the membrane antenna (reliably and cost effectively) is also a major challenge. Since the ultimate goal is to keep the weight and stowed volume of the antenna small, conventionally packaged T/R electronics are not appropriate. Furthermore, attaching a large packaged component to a thin-film membrane also presents reliability concerns. Therefore, our vision includes embedding or attaching unpackaged chips directly to the membrane structure.

The current state-of-the-art T/R modules typically use three or four chips in a packaged hybrid microcircuit. A fundamental goal is to integrate all the T/R electronics onto a single chip. This will minimize the total part count and will result in overall reductions in module cost, assembly cost, and interconnect costs, while increasing reliability. This is particularly significant when tens of thousands of T/R modules are required.

Since the chip is not packaged (at least not in the same way a conventional T/R module is packaged), the radiation shielding of the chip becomes a serious issue. Because the chip is on a membrane, the heat dissipation from the T/R is also challenging. New membrane materials with better heat conductivity are

needed for passive cooling of the electronics. At high power levels, active cooling methods such as micromachined heat pipes or similar technologies may be required. These difficulties are mitigated when very high-efficiency T/R modules are used.

As advanced (lower TRL) technologies such as thin-film organic electronics mature, the possibility of printing some portions of the T/R electronics (i.e., passive components, phase shifters, sensors, etc.) directly onto the membrane may become possible. This would greatly simplify the complexity and construction of the antenna and may lead to a substantially lower production cost, which is key to a viable SAR constellation mission.

Current Technology Investment

NASA is actively working to develop the technologies required for large membrane antennas. Figure 6.8 and Table 6.4 show the roadmap for this effort. Currently two NASA programs, Code Y's ACT program and Code R's Advanced Measurements and Detection program, are sponsoring this effort. The GESS geosynchronous SAR antenna architecture study has been used to establish the technology requirements and roadmap for the long-term SAR missions. The near-term goal is to demonstrate a fully functional 2×8 element antenna subarray by 2004. The demonstration will combine some of the key technologies that we have been developing to ensure that the system as a whole is functional before more effort is spent on increasing the TRL of the technologies in use. Internal R&D funding is also supporting an independent task to develop a single-chip MMIC T/R module, which will ultimately replace the current five-chip modules.

COMPONENT	TECHNOLOGY	LEO+	MEO	GEO
Lightweight structures	High-stiffness deployment systems with high packing efficiency; inflatable/rigidizable and mechanically deployable structures; membrane tensioning.	CR	E	E
Large membrane antennas	Durable, low-loss, thin-film membrane antenna materials; array feed technique compatible with the membrane electronics and array architecture.	CR	E	E
Integrated, rad-hard, low-power electronics	Single-chip MMIC T/R module; low-power DCG; TTD devices; L-band digital receivers.	CR	E	E
High-power, high-efficiency transmitters	High-efficiency Class-E/F L-band T/R modules; Si, GaAs, SiC, and GaN power amplifiers.	CR	E	E
Low-loss, low-power phase shifters	MEMS or BST; space-qualification and reliability is current obstacle of MEMS phase shifters; phase shifters using ferroelectric materials (BST) are another emerging technology.	CR	CR	CR
Advanced materials	New technologies for devices, structures, thermal, shielding.	CR	CR	CR
Advanced packaging	Die thinning and attachment technologies to enable the reliable, direct attachment of thinned die onto membrane; embedded electronics (vs. attachment alone) to embed the die in the structure for added reliability.	CR	E	E
Signal distribution	Technologies to simplify the interconnection of thousands of unit cells on the array; reliable RF, control, power, and data distribution; lightweight, low-loss, membrane-compatible interconnects for RF, data, and power distribution.	CR	E	E
Shielding for radiation tolerance	Since the conventional bulky package is not envisioned for the T/R module, the radiation protection of the device has to be accomplished through other methods of shielding.	CR	E	E
Passive and active thermal management	Radar-transparent thermal control coatings; variable emissivity surfaces/coatings; micro heat pipes.	CR	E	E
Power generation	Thin-film solar cells; power tiles for integrated and distributed power generation and storage on the membrane.	NR	E	E
Integrated passives	New technologies could replace the bulky energy storage capacitors with capacitor banks integrated directly in the membrane. This has the potential of lowering the complexity, mass, and cost of the antenna.	NR	CR	CR
Organic/printable electronics	Can be easily coated on flexible materials via simple processes such as ink-jet printing. A variety of molecular and polymeric materials may be used to construct thin-film transistors on a wide range of substrates.	NR	CR	CR
Large-scale manufacturing	Low-cost methods of attaching thousands of components on the membrane in such a way that the antenna is manufacturable, testable, and re-workable. Motivation for printing the electronics directly onto the membrane and integrating the remaining high-performance functions onto a single chip. New technologies such as roll-to-roll manufacturing processes are critical.	CR	CR	CR
System	Digital beamforming and digital TTD steering; calibration, metrology, and phase-correction.	CR	E	E

Table 6.4

Some of the key technologies that need to be further developed to enable advanced SAR missions of the next decade.

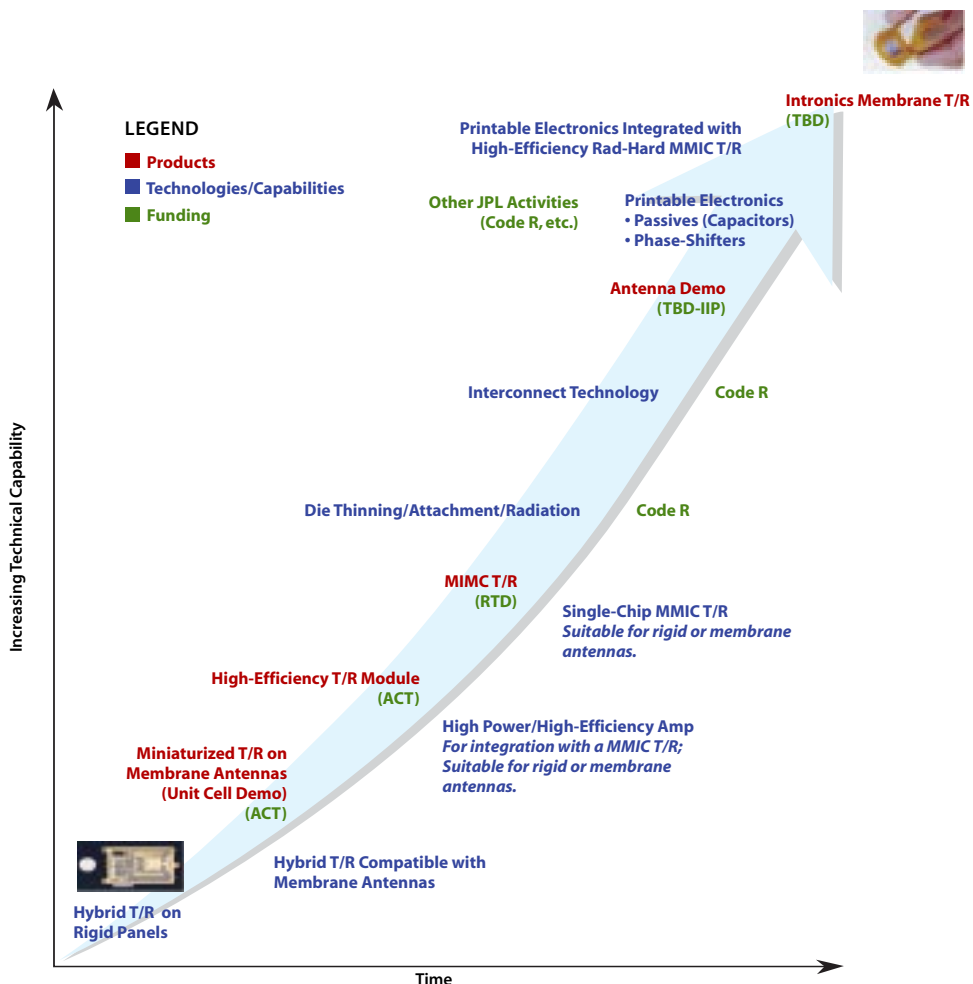
Legend

CR = Cost-reducing technology that will provide increased performance/capability

E = Enabling technology (required for mission feasibility)

NR = Not required for mission

Figure 6.8
Membrane
SAR technology
development plan.
Currently planned/
funded tasks and
relationship with
other programs
are shown in this
roadmap.



The roadmap shows the state of current technology, which is a conventionally packaged T/R module attached on a solid panel for SAR applications. The ultimate goal is to have a single flexible die integrated with the membrane. In this approach, only the parts of the T/R that cannot be printed onto the membrane are integrated onto the single chip.

One of the areas requiring additional investment is the interconnect technology. Lightweight, reliable, low-loss, membrane-compatible interconnects for RF, data, and

power distribution must be developed. Several candidate approaches exist and technology trades are required before selecting the optimal interconnect approach.

Continued research into membrane-compatible electronics is also required. The ultimate goal is a low-cost, reliable process for producing highly integrated, radiation-tolerant, mixed-signal circuits and attaching them reliably onto a membrane. This technology is critical for implementation of the GESS radar and would also enable many other large-aperture radar concepts.

The 20-Year Plan

EARTHQUAKE SCIENCE IS POISED to capitalize on a revolutionary capability for observing global crustal deformation. The concurrent improvements in seismic monitoring networks, high-performance computing, and geodetic measurement of crustal deformation have yielded significant advances in knowledge of fault behavior and crustal stress during the past decades. A major leap forward will be enabled with the ability to monitor crustal deformation with high temporal and spatial resolution. That capability will extend the observational spectrum into the realm of transient and aseismic deformation. These fast but seismically quiet deformation processes, which are at present poorly understood components of the strain budget, are key to developing a complete understanding of earthquake physics. Community models of earthquake physics and seismic hazards, developed in a data-rich environment, will rapidly evolve in response to the data. These new models are expected to yield future earthquake forecasts of useful dimensions that will feed decision-support tools to mitigate losses from future large earthquakes.

The Global Earthquake Satellite System study responds to the clearly articulated need within the solid-Earth science community for dense surface deformation data. It is a detailed implementation plan in alignment with

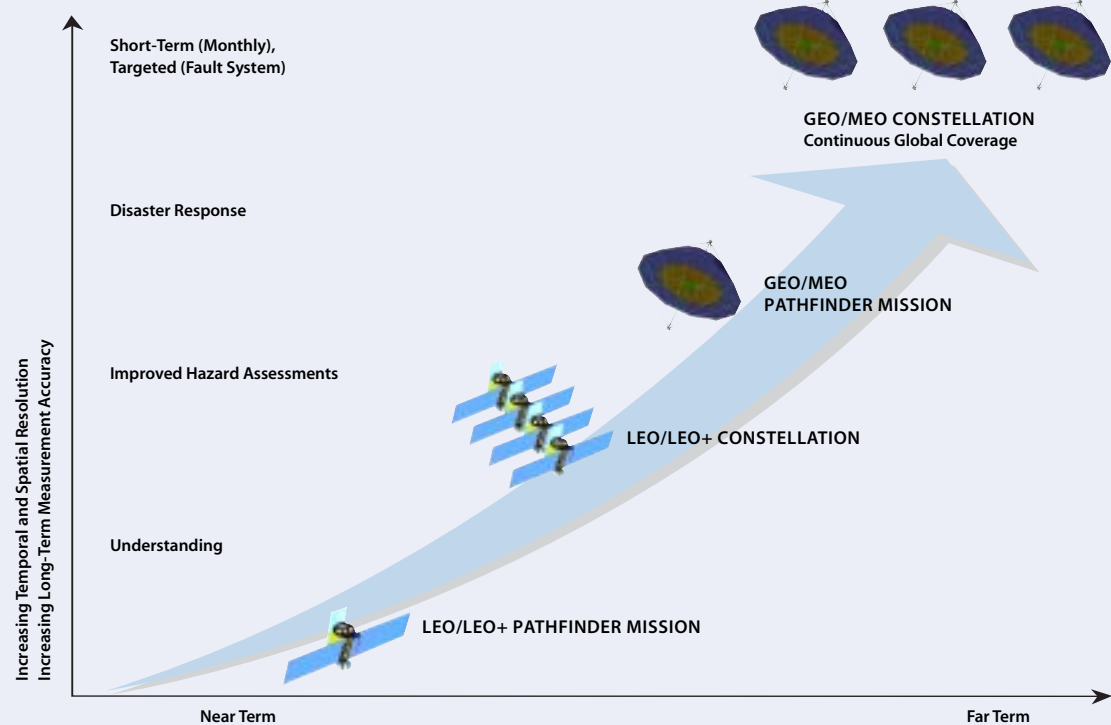
the recommendations of the SESWG, and charts the course for NASA to make major contributions to the interagency EarthScope program, while broadening those goals to a global scope. In the GESS study, we explored the requirements space for various components of an integrated system, but focused our mission architecture studies on systems that deliver high-accuracy, high-resolution surface deformation using InSAR. Detailed science requirements were gathered from the wider community to guide the studies. The major conclusion of the architecture studies is that a constellation of InSAR satellites is needed to address the requirements for monitoring a spectrum of steady and transient deformation processes. To ensure the ability to access any area on the surface of the Earth within 24 hours would require two LEO satellites in orbits above 1000 km. A few MEO or GEO satellites would be equivalent to many spacecraft in LEO and would fully characterize the known transient processes such as postseismic relaxation, slow earthquakes, creep events, and accelerated slip, with full global coverage. It is expected that new discoveries of even faster processes than are recognized today will accrue as crustal deformation measurements extend into the subdaily time scale. The spectrum of transient deformation processes known at present includes

surface deformation due to ground water storage, and hence, the hydrologic cycle. Thus, the opportunity for synergistic interaction of hydrology and tectonics, especially with regard to liquefaction susceptibility, is an exciting area of interdisciplinary research that is an added benefit of the high spatially and temporally resolved deformation measurements.

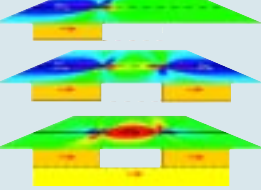
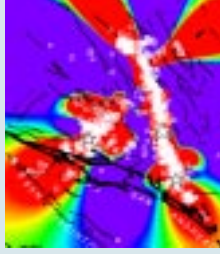
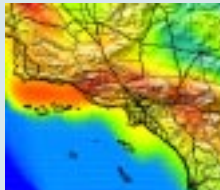
The GESS integrated science and technology plan shown on the opposite page maps the desired scientific knowledge to observational and modeling requirements and to technology investments needed to achieve the vision. Measurements from LEO orbits are

within reach at present. Higher vantage points, such as MEO or geosynchronous, require investments in inflatable, deployable antennas and structures, high-efficiency lightweight electronics, and new processing schemes to account for varying atmospheric and ionospheric conditions during the long integration times required to achieve the synthetic aperture from a slowly moving platform. These investments should be made now to ensure that NASA is ready to respond to the wealth of new discoveries that will be returned by a near-term LEO InSAR constellation.

GESS Roadmap



GESS Integrated Program

CAPABILITY TIMELINE	OBSERVATIONAL SYSTEM NEEDS	MODELING REQUIREMENTS	TECHNOLOGY INVESTMENT NEEDS
2003–08 Understanding earthquake physics	<p>Single LEO InSAR satellite (EarthScope)</p> 	<p>Time-dependent models of interacting fault systems</p>	<p>Deployable antennas and lightweight radar electronics</p>
2008–2013 Mapping crustal stress	<p>Radar-equipped UAVs for disaster response</p> 	<p>Development of distributed community modeling environment</p>	<p>Trade studies of MEO vs. GEO vantage points</p>
2013–2018 Experimental short-term (< 1 yr) earthquake forecasts	<p>2–3 satellite LEO+ InSAR constellation</p> 	<p>High-resolution atmospheric models ingesting radar data to correct atmospheric delay</p> <p>Integrate tectonics, hydrology, and human influence into comprehensive surface deformation model</p>	<p>Large-aperture membrane antennas</p> <p>Large inflatable/deployable structures</p> <p>Radiation-hardened, low-power electronics</p>
>2018 Monthly hazard assessments at scale of fault systems	<p>GEO or MEO InSAR demonstration</p> <p>Continue LEO+ constellation</p> 	<p>Data-mining and pattern-recognition techniques to detect anomalies</p> <p>Rapid verification and assessment of potential earthquake precursors</p>	<p>Integrated thin-film solar arrays</p> <p>Membrane-compatible electronics and signal distribution</p>

Appendix

GESS Investigators

PRINCIPAL AND CO-INVESTIGATORS/ INSTITUTIONS	REPORT
Burgmann, R., Freed, A., and Schmidt, D.—UC Berkeley	InSAR System Requirements for Resolution of Crustal Deformation Parameters Associated with the Earthquake Cycle
Chao, B., Harding, D., Cohen, S., and Luthcke, S.—NASA/GSFC; Hofton, M. and Blair, J. B.—University of Maryland	Global Earthquake Satellite System Requirements Derived from a Suite of Scientific Observational and Modeling Studies: Final Reports
Crippen, R.—JPL	Thermal Imaging of Seismic Events
Donnellan, A. and Hurst, K.—JPL	Inversion of Earthquake Fault Parameters Using Multiple Look Angles
Feigl, K., McClusky, S., Herring, T., and Reilinger, R.—Massachusetts Institute of Technology	Geodetic Improvements for Calculating, Analyzing, and Modeling INSAR Measurements in Synergy with GPS
Fielding, E. J.—JPL; Wright, T. J.—University of Oxford (UK)	Deformation on Complex Fault Zones, Interseismic, Co-seismic and Post-seismic Strain
Melbourne, T. and Baxter, S.—Central Washington University; Webb, F.—JPL	Quantifying Earth's Surface Deformation Budget
Olsen, K. and Peyrat, S.—UC Santa Barbara	Which Rupture Dynamics Parameters Can Be Estimated from SAR and Strong Ground Motion Data?
Price, E., Elitas, S., Freymueller, J., McNutt, S., and Hansen, R.—University of Alaska	Requirements of a SAR Satellite for Monitoring Earthquakes and Crustal Deformation in Alaska
Rundle, J. B. and Kellogg, L. H.—UC Davis	Requirements for Modeling Systems Associated with the NASA Global Earth Satellite System (GESS)
Sammis, C. G.—University of Southern California; Ivins, E.—JPL	Using GESS to Detect Stress Shadows Following Large Earthquakes and to Monitor Their Decay
Sandwell, D. and Fialko, Y.—Scripps/UC San Diego	Requirements for Observing Slow Crustal Deformation Due to Tectonic and Volcanic Processes in the Presence of Tropospheric Noise and Decorrelation
Shinozuka, M. and Bardet, J.-P.—University of Southern California; Eguchi, R.—ImageCat, Inc.	Change Detection Studies for Liquefaction Ground Failure
Simons, M.—Caltech	Constraining Co-seismic Fault Motion and Surface Disruption of Large Earthquakes Using INSAR and Seismology
Taylor, P. and Purucker, M.—NASA/GSFC	Searching for a Magnetic Signature from Earthquakes in the Ionosphere
Webb, F.—JPL; Emardson, R.—JPL (visiting); Simons, M.—Caltech	Neutral Atmospheric Delay in Interferometric Synthetic Aperture Radar Applications: Statistical Description and Mitigation
Zebker, H. and Segall, P.—Stanford	Characterizing Space-Time Patterns of Slip at Depth Along Fault Systems: InSAR Measurement and System Requirements

GESS Science Definition Team

Chair: Carol A. Raymond

*Jet Propulsion Laboratory,
California Institute of Technology*

Douglas Burbank

University of California, Santa Barbara

Benjamin F. Chao

NASA Goddard Space Flight Center

Andrea Donnellan

*Jet Propulsion Laboratory,
California Institute of Technology*

Alan Gillespie

University of Washington

Thomas L. Henyey

University of Southern California

Thomas Herring

Massachusetts Institute of Technology

Thomas Jordan

University of Southern California

Donald L. Turcotte

Cornell University

Mary Lou Zoback

U.S. Geological Survey

**GESS Study Team,
Jet Propulsion Laboratory,
California Institute of Technology**

Carol A. Raymond Jeff Booth

Science Lead Curtis Chen

Soren Madsen Adam Freedman

Radar Lead David Imel

Wendy Edelstein Yunling Lou

Technology Lead Paul Lundgren

References

Bawden, G., W. Thatcher, R. S. Stein, K. W. Hudnut, and G. Peltzer, Tectonic contraction across Los Angeles after removal of groundwater pumping effects, *Nature*, 412, 812–815, 2001.

Burgmann, R., A. M. Freed, and D. Schmidt, InSAR system requirements for resolution of crustal deformation parameters associated with the earthquake cycle, 10 pp., *Final Report, GESS Requirements Definition Study*, JPL Contract 1232377, 2002.

Chao, B. F., S. C. Cohen, D. J. Harding, M. Hofton, J. B. Blair, and S. B. Luthcke, Global Earthquake Satellite System requirements derived from a suite of scientific observational and modeling studies: Final reports, 24 pp., *Final Report, GESS Requirements Definition Study*, 2002.

Crippen, R., Thermal Imaging of Seismic Events, 6 pp., *Final Report, GESS Requirements Definition Study*, 2002.

DeLouis, B., P. Lundgren, J. Salichon, and D. Giardini, Joint inversion of InSAR and teleseismic data for the slip history of the 1999 Izmit (Turkey) earthquake, *Geophys. Res. Lett.*, 27, 3389–3392, 2000.

Feigl, K., S. McClusky, T. Herring, and R. Reilinger, Geodetic improvements for calculating, analyzing and modeling INSAR measurements in synergy with GPS, 9 pp., *Final Report, GESS Requirements Definition Study*, JPL Contract 1233102, 2002.

Fielding, E. J. and T. J. Wright, Deformation on complex fault zones, interseismic, co-seismic and post-seismic strain, *Final Report, GESS Requirements Definition Study*, 2002.

Fenoglio, M. A., M. J. S. Johnston, and J. Byerlee, Magnetic and electric fields associated with changes in high pore pressure in fault zones: application to the Loma Prieta ULF emissions, *J. Geophys. Res.*, 100, 12951–12958, 1995.

Freed, A. M. and J. Lin, Delayed triggering of the 1999 Hector Mine earthquake by viscoelastic stress transfer, *Nature*, 411, 180–183, 2001.

Hamza, V. M., Tectonic leakage of fault bounded aquifers subject to non-isothermal recharge: a mechanism generating thermal precursors to seismic events, *Phys. Earth Plan. Int.*, 126, 163–177, 2001.

Hofton, M. A. and J. B. Blair, Detecting vertical ground surface change using laser pulse correlation, *J. Geodyn.*, 34, 477–489, 2002.

- Huang J., M. Lou, A. Feria, and Y. Kim, An inflatable L-band microstrip SAR array, *IEEE AP-S/URSI Symposium*, Atlanta, Georgia, pp. 2100–2103, June 1998.
- Ivins, E., personal communication to Carol A. Raymond, 2003.
- Johnston, M. J. S., Review of electric and magnetic fields accompanying seismic and volcanic activity, *Surveys in Geophysics*, 18, 441–475, 1997.
- Kee, S.D., I. Aoki, and D.B. Rutledge, 7-MHz, 1.1-kW demonstration of the new E/F_{2,odd} switching amplifier class, 2001 *IEEE MTT-S International Microwave Symposium Digest*, 3, 1505–1508, 2001.
- Komatitsch, D. and J. Tromp, Spectral-element simulations of global seismic wave propagation - I. Validation, *Geophys. Jour. Int.*, 149, 390–412, 2002.
- Lienkaemper, J.J., J.S. Galehouse, and R.W. Simpson, Creep response of the Hayward Fault to stress changes caused by the Loma Prieta earthquake, *Science*, 276, 2014–2016, 1997.
- Lundgren, P.R., InSAR time series resolution of blind thrust and surface fault creep, 3 pp., *Final Report, GESS Requirements Definition Study*, 2002.
- Madsen, S.N., C. Chen, and W. Edelstein, Radar options for global earthquake monitoring, *IGARSS 04_09_14:00*, 2002.
- Melbourne, T., S. Baxter, and F. Webb, Quantifying Earth's surface deformation budget, 9 pp., *Final Report, GESS Requirements Definition Study*, JPL Contract 1232313, 2002.
- Minster, J.B., personal communication to Carol A. Raymond, 2001.
- Olsen, K., and S. Peyrat, Which rupture parameters can be estimated from SAR and strong ground motion data?, 11 pp., *Final Report, GESS Requirements Definition Study*, JPL Contract 1232158, 2002.
- Park, S. K., Precursors to earthquakes: Seismoelectromagnetic signals, *Surv. Geophys.*, 17, 493–516, 1996.
- Pollitz, F.F. and I. S. Sacks, Stress triggering of the 1999 Hector Mine earthquake by transient deformation following the 1992 Landers earthquake, *Bull. Seismo. Soc. Amer.*, 92, 1487–1496, 2002.
- Price, E., S. Elitas, J. Freymueller, S. McNutt, and R. Hansen, Requirements of a SAR satellite for monitoring earthquakes and crustal deformation in Alaska, 10 pp., *Final Report, GESS Requirements Definition Study*, JPL Contract 1232431, 2002.
- Pritchard, M., M. Simons, P. Rosen, S. Hensley, and F. Webb, *Geophys. J. Int.*, 150, 362–376, 2002.
- Rundle, J. B. and L. H. Kellogg, Requirements for modeling systems associated with the NASA Global Earthquake Satellite System (GESS), 25 pp., *Final Report, GESS Requirements Definition Study*, JPL Contracts 1232241/1232379, 2002.
- Rundle, J. B., L. H. Kellogg, K. F. Tiampo, W. Klein, P. B. Rundle, and A. Donnellan, Illuminating the relationship between observable data and unobservable dynamics using numerical simulations of a changing Earth, *PAGEOPH*, submitted, Fall 2002.
- Sandwell, D. and Y. Fialko, Requirements for observing slow crustal deformation due to tectonic and volcanic processes in the presence of tropospheric noise and decorrelation, *CD-ROM Final Report, GESS Requirements Definition Study*, JPL Contract 1232381, 2002.
- Sammis, C. G. and E. Ivins, Using GESS to detect stress shadows following large earthquakes and to monitor their decay, 17 pp., *Final Report, GESS Requirements Definition Study*, JPL Contract 1235152, 2002.
- Shinozuka, M., B. Mansouri, R.T. Eguchi, and C. K. Huyck, Change detection studies for liquefaction ground failure: 16 pp., *Final Report, GESS Requirements Definition Study (Part A)*, JPL Contract 1232166, 2002.
- Taylor, P. and M. Purucker, Searching for a magnetic signature from earthquakes in the ionosphere, 76 pp., *Final Report, GESS Requirements Definition Study*, 2002.
- Tobita, T., J-P Bardet, and M. Shinozuka, Regional detection of soil liquefaction susceptibility using SAR, 58 pp., *Final Report, GESS Requirements Definition Study (Part B)*, JPL Contract 1232166, 2002.
- Toda, S., R. S. Stein, and T. Sagiya, Evidence from the AD 2000 Izu islands earthquake swarm that stressing rate governs seismicity, *Nature*, 419, 58–61, 2002.
- Tomiyasu, K., Conceptual performance of a satellite borne, wide swath synthetic aperture radar, *IEEE Transactions on Geoscience and Remote Sensing*, GE-19(2), 108–116, 1981.
- Zebker, H. and P. Segall, Characterizing space–time patterns of slip at depth along fault systems: InSAR measurement and system requirements, 6pp., *Final Report, GESS Requirements Definition Study*, JPL Contract 1232132, 2002.



National Aeronautics and
Space Administration
Jet Propulsion Laboratory
California Institute of Technology
Pasadena, California

JPL 400-1069 03/03